

Cosmic rays and the magnetic field in the nearby starburst galaxy NGC 253



Dissertation

zur
Erlangung des Grades
„Doktor der Naturwissenschaften“
der Fakultät für Physik und Astronomie
an der Ruhr-Universität Bochum

von
Volker Heesen
aus
Moers

Bochum 2007

1. Gutachter: Prof. Dr. Ralf-Jürgen Dettmar
2. Gutachter: Prof. Dr. Reinhard Schlickeiser

Tag der Disputation: 8. Februar 2008

Für meine Familie

”Und die Flucht der Sternennebel! Was?! Haben Sie nicht davon gehört?! Die Flucht!! Was ist das?! Wer flieht?! Das ist verdächtig – mehr noch – das ist ein Schuldbekenntnis!!”
Stanisław Lem. Memoiren, gefunden in der Badewanne.

Contents

| | | |
|----------|---|-----------|
| 1 | Introduction | 1 |
| 1.1 | Organization of the thesis | 4 |
| 2 | The cosmic ray distribution in NGC 253 | 5 |
| 3 | The magnetic field structure in NGC 253 | 23 |
| 4 | Summary and Outlook | 35 |
| 4.1 | Summary | 35 |
| 4.2 | Extending the investigations to other spiral galaxies | 37 |
| 4.2.1 | Observations and data reduction | 37 |
| 4.2.2 | Morphology of the radio continuum emission | 38 |
| 4.3 | Outlook | 42 |
| A | High dynamic range single-dish imaging | 45 |
| A.1 | Constructing the beam pattern | 45 |
| A.1.1 | Observations and data reduction | 45 |
| A.1.2 | The Effelsberg beam pattern | 47 |
| A.1.3 | Elevation dependent sidelobes | 47 |
| A.2 | The cleaning procedure | 49 |
| A.2.1 | The Högbom cleaning | 49 |
| A.2.2 | The cleaned total power maps | 56 |
| A.3 | Instrumental polarization | 57 |
| A.3.1 | The transformation of Stokes Q and U | 57 |
| A.3.2 | The Effelsberg polarization maps | 61 |
| B | High dynamic range imaging with the Very Large Array (VLA) | 71 |
| B.1 | The VLA mosaic | 71 |
| B.2 | Wide field polarization imaging | 71 |
| B.2.1 | Standard polarization calibration with the VLA | 71 |
| B.2.2 | Improved snapshot technique | 72 |
| B.2.3 | Off-axis polarization calibration | 76 |
| B.2.4 | Comparison with the Effelsberg polarization maps | 81 |
| C | Color figures | 83 |
| | Bibliography | 89 |

| | |
|-------------------------|------------|
| List of Figures | 94 |
| List of Tables | 95 |
| Acknowledgments | 98 |
| Curriculum Vitae | 100 |

Chapter 1

Introduction

The temperature fluctuations in the “3 Kelvin background radiation” measured by the Wilkinson Microwave Anisotropy Probe (WMAP) revealed precisely the matter distribution in the Universe at the time of recombination (Spergel et al. 2003, 2007). These tiny density fluctuations with a relative amplitude of less than 10^{-4} are the seed which forms by gravitational collapse the structures observed today. However, the time since the formation of the Universe of 13.7 Gyr is not long enough to explain the contraction alone due to the gravity of the observed baryonic matter. The so-called cold dark matter (CDM) is thus part of the standard cosmological model to ensure structure formation on adequate time scales by the additional gravity of unseen material. Direct observations of the Universe at early epochs showed that the models successfully describe the evolution of structure on large and intermediate scales (Coles 2005). Still, there are serious contradictions on smaller, galactic scales. Observations of nearby galaxies show that galactic dark matter halos have a density profile with a flat core (de Blok & Bosma 2002). According to numerical simulations by Navarro et al. (1996), the halos should have divergent density (a cusp) at the center. Another discrepancy of the CDM-model is the predicted number of small satellite galaxies of the Milky Way which is about 10 to 100 times higher than observed (Moore et al. 1999). Moreover, the cores of galaxy clusters possess an excess of hot gas to the prediction of adiabatic heating by hierarchical formation (Ponman et al. 1999).

Several solutions to these problems which involve stellar feedback on the interstellar medium (ISM) have been proposed. Recent hydrodynamic computations by Mashchenko et al. (2006) suggest that the cusps of the dark matter density profiles in small primordial galaxies can be removed by random gas bulk motions excited by supernovae explosions. A possible scenario to explain excess of hot gas in the cores of galaxy clusters are supernova powered outflows of hot gas (Borgani et al. 2005). In the early Universe the galaxies were much closer to each other than today and hence their interaction was stronger. Frequent minor mergers can transfer gas effectively into the central regions of the galaxies fueling active star formation (Younger et al. 2007). Spatially concentrated supernovae explosions drive thermal outflows of hot gas creating galactic halos and even enrich the intergalactic medium (IGM), if the gas escapes from the gravitational potential (galactic wind). Hence, galaxies can have a strong influence on the surrounding IGM incorporating mass and momentum losses which leave the gravitational potential. The preheated intracluster medium prevents gas from collapsing into their potential wells leaving the bulk of the baryons in the Universe in a currently undetectable high-entropy sea (Ponman et al. 1999). The small escape velocity of dwarf galaxies make them particularly vulnerable to galactic wind. A possible wind might thus suppress the number of dwarf galaxies in dark matter halos of star-forming galaxies since they lose all gas by a galactic wind (Veilleux & Rupke 2004). Hence, it is likely that in the early Universe, galaxies were surrounded by a magnetized IGM. This affects the dynamics of the galaxy interaction as gravity is not the only contribution to the force equilibrium but magnetohydrodynamical effects have to

be taken into account, too. The properties of galactic winds and their contribution to the enrichment of the IGM with cosmic rays and magnetic fields are thus an important information which is needed to understand the structure formation in the early Universe.

The supernova heated gas itself can drive a galactic wind provided the heating processes are sufficiently strong and the gravitational potential is weak enough. A good example for this situation is the edge-on galaxy M 82 where a huge halo of hot X-ray gas, $H\alpha$, and radio continuum emission is detected. Observations by Hoopes et al. (2003) in $H\alpha$ confirm that the wind material will eventually reach the IGM. However, in many cases the hot gas can not drive a galactic wind alone, because strong radiation cools the gas which eventually falls back onto the disk (Breitschwerdt et al. 1991). This galactic fountain scenario might also explain the high-velocity clouds (HVCs) observed in the Milky Way halo as the cooled outflow debris falling back onto the disk. If we incorporate pressure support by cosmic rays, the galactic wind can be sustained against radiative losses, as have been shown in a pioneering work by Ipavich (1975). The cosmic rays suffer only weakly from radiative losses (mainly by synchrotron losses of the electrons). As the protons carry the large part of the energy this does not influence the cosmic ray energy significantly. Thus, the pressure support from below can drive a galactic wind against the gravity of the underlying galactic disk. Breitschwerdt et al. (1991) assumed the propagation of cosmic rays along “flux tubes” which allow a one-dimensional treatment of the problem. This model has been extended to a full three-dimensional treatment (with rotational symmetry) by Zirakashvili et al. (1996) which allows the treatment of galactic rotation. It was found that cosmic rays can drive a galactic wind under a broad choice of conditions in the disk.

The magnetic field structure is directly connected with the transport of cosmic rays. The diffusion of cosmic rays is hampered by perpendicular magnetic field lines and diffusive transport proceeds mainly along the magnetic field lines. Hence, the alignment of the magnetic field with respect to the galactic disk is important for the cosmic ray transport. Any disk-parallel magnetic field holds the cosmic ray gas in the disk. A process to create “open” field lines are the so-called superbubbles generated by successive SNe. At a certain height above the disk the shells of the superbubbles begin to overlap which results in open field lines in the halo. Another process, which opens the field lines, is the well-known Parker instability. The cosmic ray buoyancy creates a loop of magnetic field lines. The cold gas slides down along the field lines and the force directed upwards is increased (Parker 1966). Thus, a galaxy may possess a poloidal magnetic field in the halo while in the disk the magnetic field is predominantly disk-parallel.

In the local Universe the influence of the possibly magnetized IGM on the galaxy dynamics is small. Nearby objects are a good starting point for the observation of galactic winds, because of the high sensitivity and resolution which are observationally accessible. The properties of galactic winds found by such studies can be used in order to extrapolate the influence of galactic winds on the IGM in the early Universe. The ultimate goal is to establish the connection between the magnetic field formation and structure formation in the early Universe. One of the most favoured objects to study is the archetypical starburst galaxy NGC 253. It hosts one of the brightest radio halos discovered so far and observations with the current generation of radio telescopes allow the study of cosmic rays and magnetic fields far away from the disk. This galaxy is thus a preview of what will be possible with the next generation of radio telescopes like the Expanded Very Large Array (EVLA), the Low Frequency Array (LOFAR), and the Square Kilometre Array (SKA). All of them have a higher sensitivity and the possible observation at lower frequencies will not be so much limited by the aging of cosmic ray electrons due to synchrotron losses. Thus, the expected observable vertical extent of radio halos will be significantly larger. A special technique that circumvents the problem of cosmic ray aging in halos of galaxies is the Faraday mapping of polarized background sources which will be one of the key science projects of the SKA (Gaensler et al. 2004). Currently, with this technique the mapping of galactic halos is hampered by the sparsely

| ISM constituent | T [K] | n [cm ⁻³] |
|--------------------------------------|-----------------------|-------------------------|
| Atomic Hydrogen (HI) | $100 - 5 \times 10^3$ | $1 - 100$ |
| Molecular Hydrogen (H ₂) | $5 - 100$ | $100 - 10^4$ |
| Other Molecules | $5 - 100$ | $100 - 10^6$ |
| Ionized Hydrogen (HII) | 5000 | $10^2 - 10^4$ |
| Coronal Gas | $10^6 - 10^7$ | 10^{-2} |
| Dust Grains | $20 - 100$ | — |
| Magnetic Fields | — | — |
| Cosmic Rays | — | — |

Table 1.1: *Constituents of the ISM.*

populated background sources and hence the direct observation of halos in synchrotron emission is still favourable (Beck & Gaensler 2004).

NGC 253 contains a region of active star formation in the inner part of the disk which is connected with large lobes observed in HI, H α , and soft X-ray emission. The gas can be traced up to 8 kpc away from the disk (Pietsch et al. 2000) and it is likely that the outflow is strong enough to drive a galactic wind which reaches the IGM. The outflow model must explain the properties of the different phases of the interstellar medium (ISM) in the halo of NGC 253 which are traced by various observations. These are the molecular medium, the cold neutral medium, and the warm ionized medium, which is also known as diffuse ionized gas. The description of the ISM would be incomplete if we neglect other ingredients namely cosmic rays, magnetic fields, the interstellar radiation field, and dust. The constituents of the ISM are listed in Table 1.1.

In the halo of NGC 253 various phases of the ISM have been detected so far. Pietsch et al. (2000) detected a huge X-ray halo proving the existence of hot coronal gas with temperatures of 10^6 K. A possible explanation for the hot X-ray emitting gas is a wind, driven by the intense star formation in the inner regions of the disk. The kinetic energy of the wind is thermalized by shockwaves which heat the gas. The X-ray emission is concentrated in lobes enveloping two huge cavities on both sides of the disk which are generally referred to as *superbubbles*. H α -emitting gas with temperatures of 10^4 K was found to be concentrated in lobes which surround the X-ray emitting gas (Hoopes et al. 1996). Moreover, HI observations of Boomsma et al. (2005) show huge lobes of extra-planar cold neutral gas enveloping the superbubbles (see Fig. 1.1 for a cartoon of the distribution of the ISM phases in the halo). This cold gas is an important ingredient to explain the formation of shockwaves by the expanding superbubble, since a population of preexisting clouds in the halo is not consistent with the observed distribution of X-ray and H α -emitting gas (Strickland et al. 2002). The source of the cold neutral gas in the halo, however, remains unclear. A minor merger with a satellite galaxy is unlikely, since the distribution of the cold gas is highly symmetric with respect to the major axis (Boomsma et al. 2005). Moreover, the striking asymmetry of extra-planar HI gas between the northeastern and the southwestern halo requires another explanation. A connection to the disk is likely since radio continuum observations by Carilli et al. (1992) indicate a higher star-formation rate in the northeastern disk. Until now, no such possible transport of cold gas by a galactic wind blowing over the entire extent of the disk into the halo has been discovered.

I will use radio continuum observations presented in this thesis to investigate the connection between the star-forming disk and the halo. As cosmic rays are generated and accelerated in the disk by supernova explosions, the existence of extra-planar diffuse synchrotron emission requires a transport of cosmic rays from the disk into the halo. The lifetime of the cosmic ray electrons imposes a lower limit on the velocity of the transport which hence allows to calculate the cosmic ray bulk speed. The cosmic rays are coupled

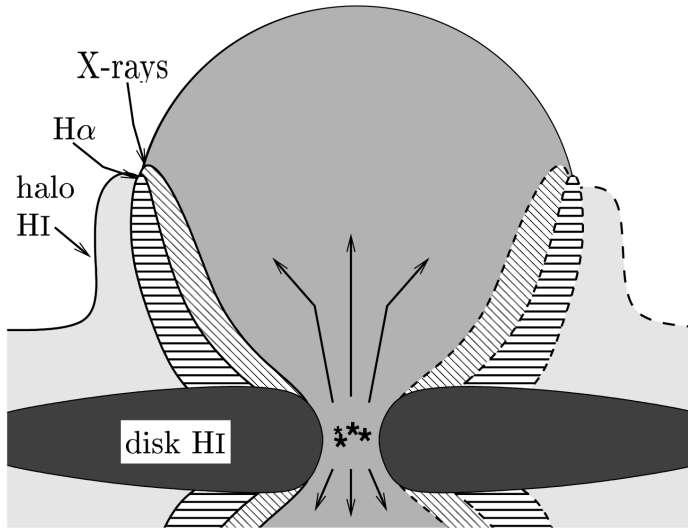


Figure 1.1: *Reproduced Fig. 8 of Boomsma et al. (2005). The dashed lines on the right outline parts that have not been detected.*

effectively via the *streaming instability* to the plasma (Kulsrud & Pearce 1969). Scattering at Alfvén waves and fast magnetosonic waves produce an isotropic pitch angle distribution in the local comoving coordinate system. Thus, cosmic rays cannot stream faster with respect to the background plasma than with the Alfvén speed. Hence, by investigating the cosmic ray transport, we can essentially study the transport of (partially) ionized gas from the disk into the halo. Moreover, I will investigate the three-dimensional magnetic field structure in the halo of NGC 253 and compare it with the features seen in the other ISM phases.

1.1 Organization of the thesis

This thesis is organized as follows: after this introduction the main work is presented in two chapters along with the new radio continuum observations of NGC 253. In Chapter 2, I investigate the cosmic ray distribution from the continuum emission. In Chapter 3, I discuss the three-dimensional structure of the magnetic field using the polarimetry information of the observations. I summarize my results and give an outlook in Chapter 4.

NGC 253 is a challenge for radio continuum observations since it harbors a very bright point source. Hence, I have tailored the data calibration to a high dynamic range. Appendix A contains a description how the single-dish observations with the 100-m Effelsberg telescope were cleaned and a correction of the instrumental effects on the polarization was applied. Obtaining the polarization mosaic from the interferometric VLA observations required a wide-field polarization calibration which is presented in Appendix B.

Cosmic rays and the magnetic field in the nearby starburst galaxy NGC 253 I. The cosmic ray distribution

Volker Heesen¹, Rainer Beck², Marita Krause², and Ralf-Jürgen Dettmar¹

¹ Astronomisches Institut der Ruhr-Universität Bochum, Universitätsstr. 150, 44780 Bochum, Germany

² Max-Planck Institut für Radioastronomie, Auf dem Hügel 69, 53121 Bonn, Germany

Received 2008/ / Accepted 2008/

ABSTRACT

Context. The models of cosmic ray (CR) transport still lack detailed observational constraints. Nearby edge-on galaxies are the best objects to study the vertical CR distribution with high sensitivity and resolution, since the extra-planar distribution of CRs in the Milky Way cannot reliably be determined from within the galaxy.

Aims. The diffusive and convective CR transport from the disk into the halo is discussed with vertical profiles of the CR bulk speed. The connection of the CR transport with the superwind model is investigated.

Methods. From high resolution radio continuum observations of the nearby starburst galaxy NGC 253 we determine the local correlation between the extra-planar CR distribution and the magnetic field structure. With the VLA we have obtained a mosaic consisting of 15 pointings at $\lambda 6.2$ cm. The missing zero-spacing flux of the VLA mosaic has been filled up using observations with the 100-m Effelsberg telescope. We also obtained new $\lambda 3.6$ cm maps with Effelsberg observations and use a three-pointing mosaic at $\lambda 20$ cm from the VLA archive. Moreover, we reproduced a $\lambda 90$ cm map presented by Carilli et al. (1992). The high dynamic range caused by the strong nuclear point source was addressed with a special data calibration scheme for both the single dish and interferometric observations.

Results. We find a thin and a thick radio disk with a scaleheight of 0.3 kpc and 1.7 kpc for $\lambda 6.2$ cm, respectively. The equipartition total magnetic field strength of $15 \mu\text{G}$ in the disk is remarkably high. Spectral index profiles between $\lambda 90$ cm and $\lambda 6.2$ cm show a steepening of the spectral index with increasing distance from the disk. This can be explained by strong radiative losses of the cosmic ray electrons (CREs). We find a local linear correlation between the scaleheight and the CRE synchrotron lifetime which requires a significant vertical CR bulk speed of at least 270 km s^{-1} .

Conclusions. The cosmic ray transport can be best described for the eastern halo by convection and for the western halo by diffusion. A stronger wind in the eastern halo, suggested also by the extra-planar abundance of H I, H α , and soft X-ray emission may explain this dichotomy of the cosmic ray transport.

Key words. keyword 1 - keyword 2 - keyword 3

1. Introduction

NGC 253 is a prototypical starburst galaxy at a distance of 3.94 Mpc (Karachentsev et al. 2003). It is a late-type spiral galaxy with a high inclination angle of 78.5° . This allows for observation of extra-planar components of the interstellar medium (ISM) at different wavelengths: ROSAT Position Sensitive Proportional Counter (PSPC) observations have revealed a very extended halo of soft diffusive X-ray emission extending into the halo to a distance of 8 kpc from the disk. The prominent lobes of soft X-ray emission show a distinct “X”-shaped pattern centered on the nucleus (Pietsch et al. 2000). Moreover, H α observations by Hoopes et al. (1996) show prominent plumes emerging from the disk into the halo which spatially coincide with the lobes of the soft X-ray emission. Observations of Boomsma et al. (2005) in H I show large plumes of extra-planar H I emission enclosing the soft X-ray emission.

Given the different species of the interstellar medium in the halo of NGC 253 the question arises, how the observed halo structure has been formed? The onion shell appearance of the different ISM phases have led to the suggestion that the halo can be considered as one huge bubble which is fueled by an active star forming region around the nucleus of the galaxy. This so-called *superwind* scenario is supported by the finding of a

small plume of hot X-ray gas in CHANDRA maps associated with a conical outflow from the nuclear starburst (Strickland et al. 2000). Spectroscopic measurements of H α -emitting gas in the southern nuclear outflow cone by Schulz & Wegner (1992) give an outflow velocity of 390 km s^{-1} . An attractive aspect of the superwind model is that the observed lobes observed in the different extra-planar ISM species can be explained by *limb brightening*. Numerical simulations of the superwind model by Suchkov et al. (1994) followed the evolution of a multi-phase halo powered by a point source located in the center of the disk. A good resemblance of the “X”-shaped pattern of the soft X-ray emission was indeed found which could be interpreted as the termination shock of the hot gas where the gas can cool effectively. On the other hand, the dilute hot plasma inside the bubble is not visible because of its low density. It should be noted that the AGN activity is at most weak, if there is an AGN at all (Mohan et al. 2002), and thus the nuclear starburst is the only energy source to be considered.

The superwind model can be tested with the distribution of the different ISM phases in the halo and must thereby explain the luminosity of the hot gas. A possible explanation for the amount of X-ray and H α -emitting gas in the halo is the dissipation of kinetic energy via shock heating (Lehnert &

Heckman 1996) if the thermalization fraction is high enough (Strickland et al. 2002). A precondition for this model is the existence of cool gas in the halo which condenses to clouds at which the shock can form. ISOPHOT observations discussed by Radovich et al. (2001) show “X”-shaped FIR emission overlapping with the $H\alpha$ and X-ray emission indicating the existence of such a cool gas. However, the origin of the gas is not clear. It could be a preexisting population of cool gas in the halo, possibly accreted from a merger with a satellite. Another possibility is that the wind carries its own cool gas into the halo as suggested by simulations. These show that the gas of the disk can be transported into the halo along the walls of the cavity, as Kelvin-Helmholtz instabilities rip of clumps off cool gas in the disk (see e.g. Suchkov et al. 1994; Heckman et al. 2000).

Cosmic rays (CRs) and magnetic fields are important for the evolution of the ISM, because they possess an energy density comparable to that of the thermal gas (Beck et al. 1996). They are even more important for the study of galactic winds, because the supernova-heated gas itself can drive a galactic wind only when the heating processes are sufficiently strong and the gravitational potential is comparably weak. A good example for this situation is the edge-on galaxy M 82, which possesses a huge halo of hot X-ray, $H\alpha$, and radio continuum emission. However, the hot gas cools radiatively preventing the escape from the gravitational potential and falls back onto the disk in condensed clouds. This *galactic fountain* scenario proposed by Field et al. (1969) might explain the infall of the so-called High Velocity Clouds (HVC’s) which could be interpreted as cooled remnants of the hot gas.

If we incorporate the CR pressure the galactic wind can be sustained against the radiative losses (Ipavich 1975), because the CRs suffer only little from radiative losses (mainly via synchrotron losses of the electrons). As the protons carry the large part of the energy this does not influence the cosmic ray energy density. Thus the pressure support from below can drive a galactic wind against the gravity of the underlying galactic disk. Breitschwerdt et al. (1991, 1993) started a series of papers treating the cosmic ray transport along “flux tubes” in a one-dimensional model. This model has been extended to a full three-dimensional treatment (with rotational symmetry) by Zirakashvili et al. (1996), including the influence of galactic rotation. It was found that CRs can drive a galactic wind under a broad variety of conditions in the disk and that the loss of mass and momentum over the lifetime of a galaxy is significant (Ptuskin et al. 1997).

The theory of a CR driven galactic wind can be constrained with radio continuum studies. As the relativistic CRs are the most pervasive component of the ISM, they are expected to be associated with the other phases in the halo of NGC 253. Indeed, a radio halo around NGC 253 was detected by Beck et al. (1979) using the 100-m Effelsberg telescope¹ at $\lambda 2.8$ cm. However, no correction for the sidelobes of the strong nuclear point source was applied and thus it was not possible to disentangle the intrinsic halo emission from the contribution by the sidelobes. The study was extended later with VLA² interferometric observations by Carilli et al. (1992), which show an extended halo over the length of the optical disk. The finding of a large radio spur southeast of the nucleus already led to speculations of an

outflow connected with the spur. Extending the observations to other wavelengths and including the polarization, a prediction of the magnetic field structure in the disk was presented by Beck et al. (1994). The sensitivity of the observations was not sufficient to get information for the extra-planar polarized emission.

With the new VLA mosaic at $\lambda 6.2$ cm we are able to increase the sensitivity at this short wavelength, allowing us to study in detail the extra-planar emission at this high frequency. The advantage is that the high synchrotron losses at this short wavelength allow to impose tighter constraints on the CR propagation from the disk into the halo. Moreover, for the first time sensitive polarization measurements have been carried out to study the large-scale magnetic field structure in the halo of NGC 253 which will be addressed in a subsequent paper (thereafter Paper II).

This paper is organized as follows: in Sect. 2 we introduce our observations and present the data calibration. We present our radio continuum maps along with a discussion of the morphology in Sect. 3. An important finding is the steepening of the spectral index with increasing distance from the disk (Sect. 4). The finding of an extended radio halo with a thick radio disk leads to the determination of the vertical CR bulk speed (Sect. 5). Eventually we will discuss the impact of our findings on the feeding of the radio halo with CRs from the star forming disk (Sect. 6). Finally we summarize our results and present our conclusions in Sect. 7.

2. Observations and data reduction

2.1. The Effelsberg observations

The $\lambda 3.6$ cm observations have been obtained between February 2003 and July 2004. The Effelsberg $\lambda 3.6$ cm receiver is equipped with a single horn and mounted in the secondary focus cabin (SFK). The receiver is capable to record the total power and the Stokes channels Q and U simultaneously. We have compiled 26 maps of each Stokes channel respectively with a map-size of $30.5' \times 20.5'$. The maps have been aligned with the major axis of NGC 253, which reduces the time for scanning. Each map has been checked and corrected for pointing errors using Gauss-fits on the nuclear point source. The final map was produced using the PLAIT algorithm, which we used to suppress scanning effects (Emerson & Gräve 1988). The noise level of the final map is $500 \mu\text{Jy}/\text{beam}$ in total power with a resolution of $84''$ Half Power Beam Width (HPBW).

The $\lambda 6.2$ cm observations were carried out with the 100-m Effelsberg telescope during 1997 by R. Beck. The dual-horn receiver effectively reduces scanning-effects via beam-switching. The restoration of the maps was done following the standard calibration process resulting in eleven maps with a map-size of $30' \times 30'$. The maps were checked and corrected for pointing errors using Gaussian fits on the nuclear point source and combined with the PLAIT algorithm. The noise level of the final map is $1 \text{ mJy}/\text{beam}$ in total power with a resolution of $144''$ (HPBW). 3C286 was used as a calibrator for the flux of the Effelsberg observations at $\lambda 3.6$ cm and $\lambda 6.2$ cm, adopting the flux density scale of Baars et al. (1977).

The sidelobes of the Effelsberg beam pattern peak at a level of a few percent which limits the dynamic range to 100 at most. As the nuclear point source has a flux density of 1 Jy we would be limited to a noise-level of $10 \text{ mJy}/\text{beam}$. In order to overcome this limitations we had to remove the sidelobes of the nuclear point source. This was accomplished by applying a procedure similar to the CLEAN algorithm by Högbom (1974). This proce-

¹ The Effelsberg 100-m telescope is operated by the Max-Planck Institut für Radioastronomie (MPIfR).

² The VLA (Very Large Array) is operated by the NRAO (National Radio Astronomy Observatory).

ture has been revised and extended for the application on single-dish observations by Klein and Rottmann (see Rottmann 1996). The required beam patterns have been obtained from deep observations of 3C84 and 0234-23 for $\lambda 3.6$ cm and $\lambda 6.2$ cm, respectively. Each single map was cleaned with a constant parallactic angle. This is sufficient, since the variation of the parallactic angle is less than 5° during the observation of a single map. Thus we were able to obtain essentially noise limited maps with a dynamic range of at least 1000. The cleaning structures (the difference between the uncleaned and the cleaned map) exhibit prominent sidelobes extending far from the disk. This underlines the importance of a careful cleaning procedure. Details of the single dish cleaning can be found in Heesen (2007).

2.2. The VLA observations

With the VLA in D-configuration we observed in July 2004 at $\lambda 6.2$ cm with a total integration time of 40 hours. The size of the primary beams of the VLA antennas at $\lambda 6.2$ cm is $8'$, requiring a mosaic of 15 pointings. They were arranged in three rows parallel to the major axis of the galaxy, including much of the extra-planar field of interest. An illustration of the mosaic setup is shown in Fig. 1 and the coordinates of the individual pointings are listed in Tab. 1. The data have been calibrated using the standard procedures in the Astronomical Image Processing System³ with the flux density scale given in Baars et al. (1977). The performed self calibration allowed us to suppress the sidelobes of the nuclear point source in order to gain a high dynamic range. After inverting the (u,v)-data and the successive cleaning we convolved the maps of each pointing with a Gaussian in order to obtain an identical clean beam. Using LTESS (part of AIPS) the maps were finally combined with a linear superposition and a correction for the VLA primary beam attenuation using information from each pointing out to the 7 percent point of the primary beam (Braun 1988). Our final map has a noise level of $30 \mu\text{Jy}/\text{beam}$ in total power which corresponds to a dynamic range of 40.000 with respect to the nucleus.

Finally, we combined the VLA map with our Effelsberg map using IMERG (part of AIPS) which performs a Fourier combination of the two maps. We found the missing zero-spacing flux to be a fraction of 10 % of the total flux measured with Effelsberg. The importance of the single-dish observations for recovering all extended emission will be briefly discussed in Sect. 3.

The $\lambda 20$ cm data were obtained from the VLA archive (presented by Carilli et al. 1992). At this wavelength the VLA primary beam size of $25'$ allows to cover the disk and halo with three pointings only. We combined the (u,v)-data of three configurations (D, C, and B) and inverted with natural weighting. The three maps were cleaned and restored with a $30''$ Gaussian. Using LTESS we constructed the final map with a noise level of $500 \mu\text{Jy}/\text{beam}$ at a resolution of $30''$ (HPBW).

3. Morphology of the total power emission

We present the total power maps as exponential contour plots with the first contour indicating emission exceeding three times the noise level. The optical background image has been obtained from the DSS (Digital Sky Survey)⁴.

³ The Astronomical Image Processing System (AIPS) is distributed by the National Radio Astronomy Observatory (NRAO) as free software.

⁴ The compressed files of the "Palomar Observatory - Space Telescope Science Institute Digital Sky Survey" of the northern sky,

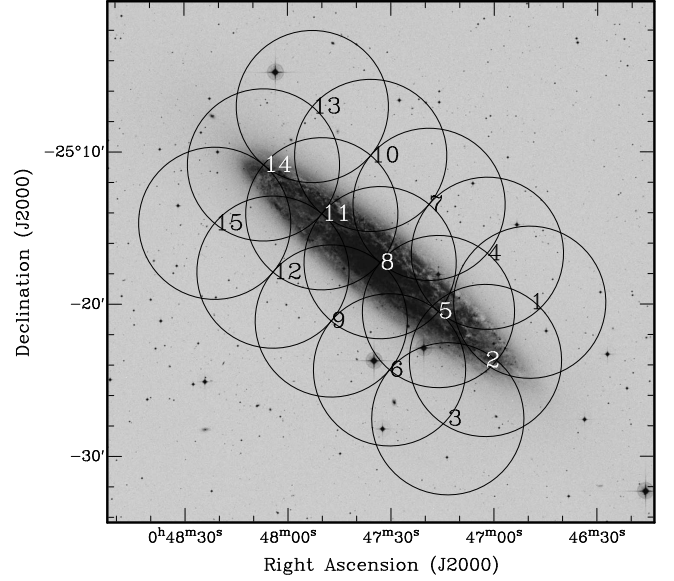


Fig. 1. The VLA mosaic of NGC 253 at $\lambda 6.2$ cm consisting of 15 pointings. The circles indicate the HPBW of the VLA primary beam which is $8'$ at $\lambda 6.2$ cm. The corresponding coordinates of the pointing centers can be found in Tab. 1. The background optical image has been obtained from the DSS.

Table 1. Coordinates of the 15 VLA mosaic pointings at $\lambda 6.2$ cm.

| Pointing | R.A. | Dec. |
|----------|---|--------------|
| 1 | 00 ^h 46 ^m 49 ^s .63 | -25°19'53".7 |
| 2 | 00 ^h 47 ^m 02 ^s .49 | -25°23'43".8 |
| 3 | 00 ^h 47 ^m 13 ^s .44 | -25°27'33".3 |
| 4 | 00 ^h 47 ^m 01 ^s .94 | -25°16'40".8 |
| 5 | 00 ^h 47 ^m 16 ^s .17 | -25°20'30".6 |
| 6 | 00 ^h 47 ^m 30 ^s .40 | -25°24'20".4 |
| 7 | 00 ^h 47 ^m 18 ^s .91 | -25°13'28".0 |
| 8 | 00 ^h 47 ^m 33 ^s .13 | -25°17'17".8 |
| 9 | 00 ^h 47 ^m 47 ^s .35 | -25°21'07".6 |
| 10 | 00 ^h 47 ^m 35 ^s .86 | -25°10'15".2 |
| 11 | 00 ^h 47 ^m 50 ^s .07 | -25°14'05".0 |
| 12 | 00 ^h 48 ^m 04 ^s .28 | -25°17'54".8 |
| 13 | 00 ^h 47 ^m 52 ^s .80 | -25°07'02".3 |
| 14 | 00 ^h 48 ^m 07 ^s .00 | -25°10'52".1 |
| 15 | 00 ^h 48 ^m 21 ^s .20 | -25°14'41".9 |

The morphology of the total power emission depends strongly on the observing wavelength and the resolution of the map. This is most prominent in the $\lambda 20$ cm and $\lambda 6.2$ cm maps presented in Figs. 2 and 3 which have the highest resolution of the presented maps with $30''$ (HPBW). These maps show a slight enhancement along the optical spiral arms, one extending to the northwest and the other to the southeast, of the radio continuum emission. The inner part of the disk shows a plateau of high emission coinciding with the brightest part in the optical image. These general features are also found in the maps with the lower resolution, though not as clearly, because they are smoothed out. The continuum emission does not exceed the optical disk along the major axis but we find a notable excess of emission along the

based on scans of the Second Palomar Sky Survey are ©1993-1995 by the California Institute of Technology and are distributed herein by agreement.

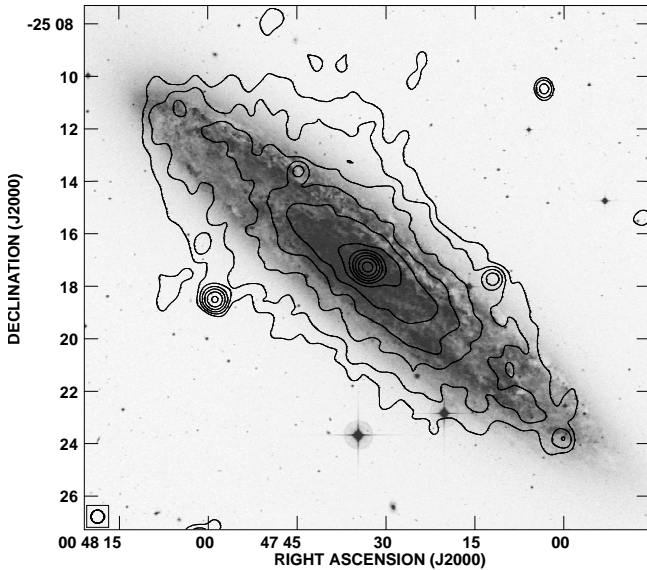


Fig. 2. Total power radio continuum at $\lambda 20$ cm obtained from the VLA observations. Contours are at 3, 6, 12, 24, 48, 96, 192, 384, 768, 1536, 3077, and 6144×0.5 mJy/beam. The background optical image is taken from the DSS, which is used in the figures below, too.

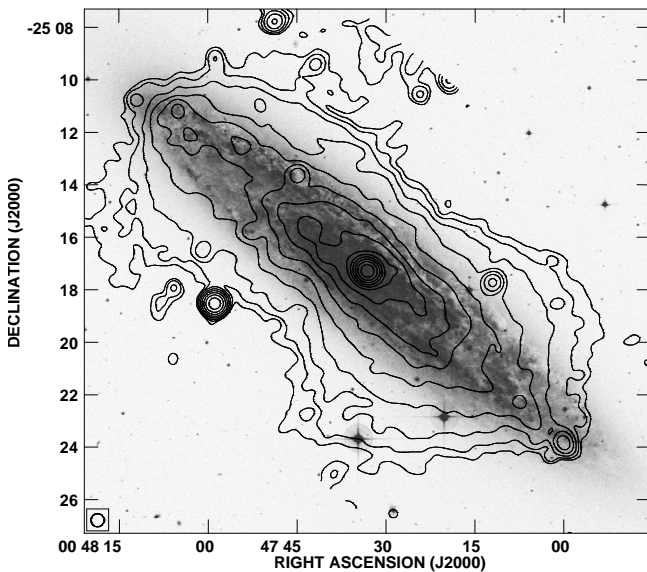


Fig. 3. Total power radio continuum at $\lambda 6.2$ cm obtained from the VLA and Effelsberg observations. Contours are at 3, 6, 12, 24, 48, 96, 192, 384, 768, 1536, 3077, 6144, 12288, and 24576×30 μ Jy/beam.

minor axis in all maps. We will refer this radiation as to *extra-planar emission*, and a detailed analysis and proof that the emission does not belong to the disk will be given later in Sect. 5.1. The abundance of extra-planar emission is strongly dependent on the observing wavelength if we compare our maps: in Fig. 4 we reproduce the $\lambda 90$ cm map with a resolution of $70''$ (HPBW) which was presented by Carilli et al. (1992). At this long wavelength the extra-planar emission is very pronounced while the disk does not show up prominently. The $\lambda 3.6$ cm Effelsberg map presented in Fig. 5 has a moderate resolution of $84''$ (HPBW) and exhibits the least extra-planar emission.

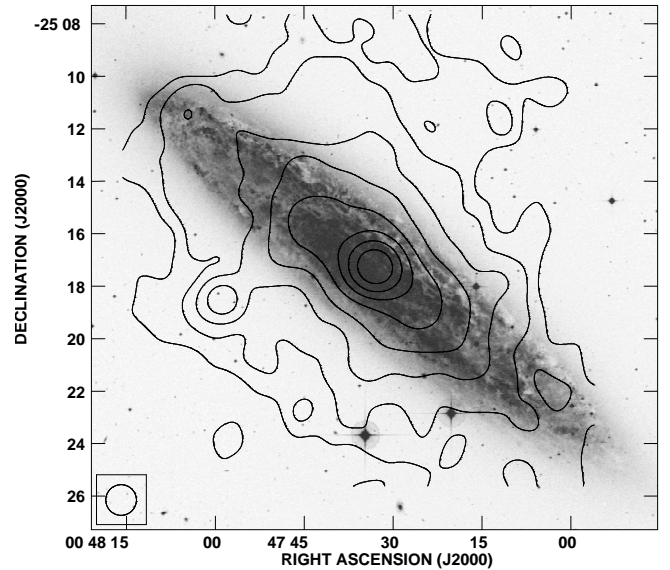


Fig. 4. Total power radio continuum at $\lambda 90$ cm obtained from VLA observations. This map has been presented by Carilli et al. (1992) and is presented in this work for analysis purposes. Contours are at 3, 6, 12, 24, 48, 96, 192, 384, 768, 1536, and 3077×6 mJy/beam.

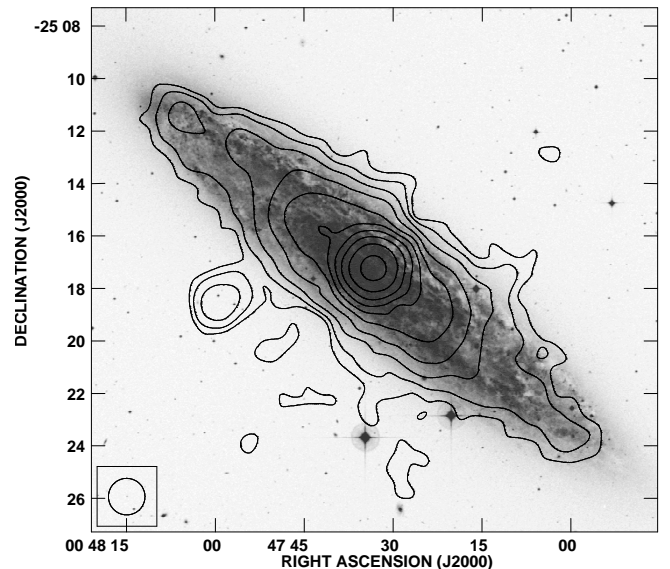


Fig. 5. Total power radio continuum at $\lambda 3.6$ cm obtained from the Effelsberg observation. Contours are at 3, 6, 12, 24, 48, 96, 192, 384, 768, and 1536×500 μ Jy/beam.

The total extension of emission perpendicular to the disk does not only depend on the wavelength but also on the sensitivity of the observations because the radio continuum emission decreases with increasing distance from the disk. We note that the $\lambda 20$ cm map shows less extra-planar emission than the $\lambda 6.2$ cm map since the noise-level of the latter one is more than 10 times smaller. Thus we observe always only the brightest tip of a huge radio halo with a given sensitivity. This is the motivation to use a different measure for the extra-planar emission which does not depend on the sensitivity: the scaleheight h , which prescribes the emission profiles perpendicular to the disk as an exponential function $\exp(-z/h)$ of the distance z from the major axis. However, even from the morphological view we find

the general trend of increasing extra-planar emission with increasing wavelength. This can be attributed to a steep spectral index caused by CR aging and will be discussed in the Sect. 5.5.

The extent of the extra-planar emission depends also on the position along the major axis. The contour lines in all maps show a dumbbell shape which means that the extension of the extra-planar emission has a local minimum in the center of the disk. This trend is visible in all maps. It is clearly most prominent at the shorter wavelengths. Especially the Effelsberg map at $\lambda 3.6$ cm has a prominent neck just at the position of the nucleus where the contour lines have a steep gradient along the minor axis. This points to a rapid vertical decrease of extra-planar emission just outside the optical disk. If the vertical decrease of emission would be equal all along the major axis, the highest extension would be expected there. We will investigate this effect in more detail and give an explanation in Sect. 5.

Moreover, there are some general features found in all maps: one is a prominent extension on the northeastern side on the nucleus. The other notable feature is an extension southeast of the nucleus. It is visible in all maps like a finger emerging from the disk with a point source located at its southern tip. This is a prominent example of a so-called “radio spur”, where the magnetic field has a strong component perpendicular to the disk as will be shown in Paper II.

Finally, we present the Effelsberg map at $\lambda 6.2$ cm in Fig. 6. Despite its low resolution of $144''$ (HPBW) this map is particularly important for our investigation. The comparison with the VLA map shown in Fig. 7 reveals how much extended emission is missing in the interferometer only image. In fact the missing total flux is about 10 % of the total flux measured with Effelsberg. If only the extended flux without the nuclear point source is considered, the fraction of the missing zero-spacing flux increases to 20 %. The correction for the missing zero-spacing flux is especially important for edge-on galaxies, since the bright disk causes deep depressions outside the disk along the minor axis in interferometric observations. Hence, the reconstruction of the extra-planar emission at $\lambda 6.2$ cm crucially depends on the Effelsberg map. We stress that also for mosaics, which cover the entire region of interest, a single-dish map is necessary in order to detect all extended emission. This even applies for the $\lambda 20$ cm VLA map where the primary beam size is comparable with the size of the disk of NGC 253. The analysis of the extra-planar spectral index gives indication that there is still flux missing (see Sect. 4.3).

4. Spectral index distribution

4.1. Point sources

Our continuum maps, in particular those with the highest resolution, which are the $\lambda 20$ cm and the $\lambda 6.2$ cm maps, show several point sources. We obtained peak fluxes and positions in both maps using Gaussians which were fitted to the images. Neglecting any proper motion of the sources within our different observing epochs (our linear resolution in the source is of the order of 1 kpc), we identified point sources if the positions in both maps were in agreement. The list of point sources presented in Tab. 2 includes positions, fluxes, and spectral indices, α , defined by the relation $S \propto \nu^{-\alpha}$, where S is the total power radio continuum flux.

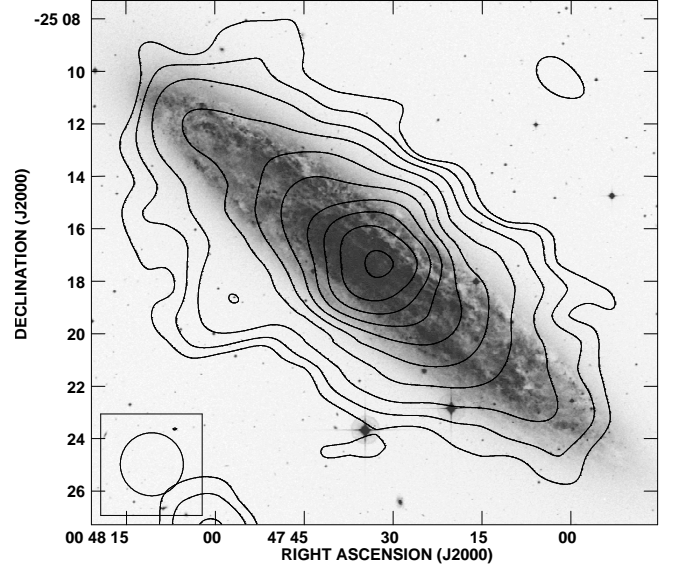


Fig. 6. Total power radio continuum at $\lambda 6.2$ cm obtained from the Effelsberg observation. Contours are at 3, 6, 12, 24, 48, 96, 192, 384, 768, and 1536×1 mJy/beam.

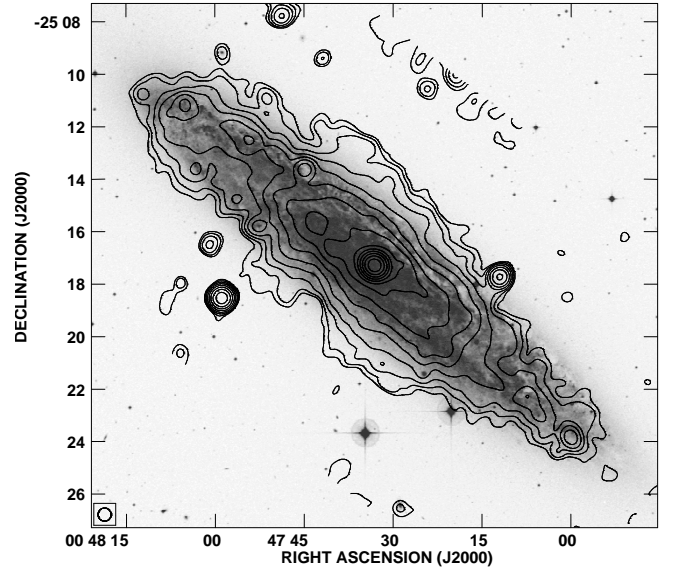


Fig. 7. Total power radio continuum at $\lambda 6.2$ cm obtained from the VLA observations. Otherwise same as Fig. 3.

The strongest two point sources, the nucleus and the point source at the southern tip of the large radio spur southeast of the nucleus, are detected at all four wavelengths. We have corrected their peak flux density obtained from the Gaussian fits by subtracting the underlying background flux density. The spectra are presented in Fig. 8. The slopes of the linear fits in the log-log diagrams are the corresponding spectral indices in the range between $\lambda 90$ cm and $\lambda 3.6$ cm. We find $\alpha_n = 0.44 \pm 0.02$ for the nucleus and $\alpha_{LS} = 0.84 \pm 0.02$ for the point source located at the radio spur. We do not find any indication of free-free absorption in the spectrum of the nucleus while Carilli (1996) reported a free-free absorption towards the nucleus indicated by his $\lambda 90$ cm observations, which show a spectral flattening towards long wavelengths. This finding has been confirmed by Lenc & Tingay (2006) who analyze the spectral behavior of sev-

Table 2. Positions of point sources obtained from Gaussian fits and the flux density for each observed wavelength. The spectral index α is defined by $S \propto \nu^{-\alpha}$, where S is the total power radio continuum flux and ν the observing frequency.

| RA | Dec | $S_{\lambda 90}$ [mJy] | $S_{\lambda 20}$ [mJy] | $S_{\lambda 6.2}$ [mJy] | $S_{\lambda 3.6}$ [mJy] | α |
|---|--------------|------------------------|------------------------|-------------------------|-------------------------|-------------|
| 00 ^h 47 ^m 00 ^s .08 | −25°23′49″.2 | | 4.07 ± 0.19 | 2.21 ± 0.07 | | 0.51 |
| 00 ^h 47 ^m 12 ^s .09 | −25°17′45″.0 | | 15.0 ± 0.7 | 6.63 ± 0.24 | | 0.68 |
| 00 ^h 47 ^m 33 ^s .12 | −25°17′17″.3 | 3960 ± 80 | 2020 ± 30 | 1267 ± 6 | 977 ± 2 | 0.44 ± 0.02 |
| 00 ^h 47 ^m 42 ^s .64 | −25°15′42″.0 | | 38.3 ± 0.2 | 7.0 ± 0.4 | | 1.41 |
| 00 ^h 47 ^m 54 ^s .66 | −25°12′31″.2 | | 6.2 ± 0.1 | 3.23 ± 0.07 | | 0.54 |
| 00 ^h 47 ^m 58 ^s .90 | −25°18′31″.9 | 190 ± 10 | 53.2 ± 0.4 | 19.44 ± 0.03 | 9.5 ± 0.5 | 0.84 ± 0.02 |
| 00 ^h 48 ^m 00 ^s .78 | −25°16′26″.3 | | 5.43 ± 0.07 | 1.10 ± 0.03 | | 1.32 |
| 00 ^h 48 ^m 04 ^s .97 | −25°11′20″.5 | | 5.24 ± 0.13 | 3.05 ± 0.10 | | 0.45 |

eral point sources in the environment of the nucleus. This can be explained with our measurement to be hampered by the large beam size which results in a high contribution of extended emission to the measured peak flux. Thus, we likely overestimate the flux at $\lambda 90$ cm, which explains the disagreement with Carilli’s finding who uses a map with a higher resolution of $33'' \times 21''$ (HPBW).

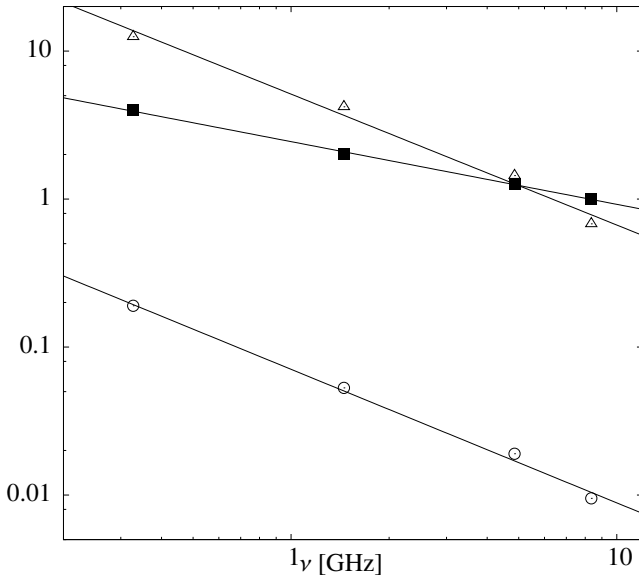


Fig. 8. Total power flux density of the nuclear point source S_n (triangles), of the point source in the left spur S_{LS} (circles), and of the extended emission S_e (boxes) as a function of the observing frequency ν . The slope of the linear fit in this log-log diagram provides the spectral indices $\alpha_n = 0.44 \pm 0.02$, $\alpha_{LS} = 0.84 \pm 0.02$, and $\alpha_e = 0.90 \pm 0.08$, respectively.

4.2. Total flux

The total radio continuum flux has been integrated within ellipses with the major axis aligned to the position angle $PA = 52^\circ$ of NGC 253. The inclination of the ellipses has been chosen in order to cover all extended emission (including the extra-planar emission) and thus it is smaller than the actual inclination of the disk. The parameters of the flux integration are listed in Tab. 3 and the total fluxes obtained with different measurements are found in Tab. 4. The flux of the point sources (see Sect. 4.1) has been subtracted in order to measure only the

flux of the extended emission.

Table 3. Parameters for integration of the total flux in ellipses.

| λ [cm] | a [arcsec] | a [kpc] | b [arcsec] | b [kpc] | i_e |
|----------------|--------------|-----------|--------------|-----------|-------|
| 90 | 620 | 12.1 | 392 | 7.6 | 50.8° |
| 20 | 620 | 12.1 | 392 | 7.6 | 50.8° |
| 6.2 | 680 | 13.3 | 430 | 8.4 | 50.8° |
| 3.6 | 648 | 12.6 | 400 | 7.8 | 52.3° |

The total fluxes were integrated within ellipses chosen to include the extended emission in the disk and the halo of NGC 253. The major axis a , the minor axis b , and the inclination i_e , defined by $b = a \cdot \cos(i_e)$ for each wavelength λ is presented..

Table 4. Integrated total power flux where S_i is the total integrated flux, and S_e is the flux of the extended emission only.

| λ [cm] | Instrument | S_i [Jy] | S_e [Jy] |
|----------------|------------------------|---------------|---------------|
| 90 | VLA | 16.5 ± 0.16 | 12.54 ± 0.18 |
| 20 | VLA | 6.259 ± 0.07 | 4.244 ± 0.08 |
| 6.2 | VLA + Effelsberg | 2.707 ± 0.010 | 1.440 ± 0.012 |
| 6.2 | VLA | 2.426 ± 0.005 | 1.159 ± 0.008 |
| 6.2 | Effelsberg (uncleaned) | 3.071 ± 0.008 | 1.804 ± 0.009 |
| 6.2 | Effelsberg (cleaned) | 2.699 ± 0.008 | 1.432 ± 0.010 |
| 3.6 | Effelsberg (uncleaned) | 1.726 ± 0.005 | 0.749 ± 0.005 |
| 3.6 | Effelsberg (cleaned) | 1.656 ± 0.005 | 0.679 ± 0.005 |

The corresponding spectrum of the extended emission is presented in Fig. 8 where we find a spectral index of $\alpha_e = 0.90 \pm 0.08$ in the range between $\lambda 90$ cm and $\lambda 3.6$ cm. This is a considerably steeper spectrum than that of young cosmic ray electrons (CREs) which are accelerated in supernovae remnants ($\alpha = 0.6$). This indicates some contribution of CR aging by strong synchrotron losses which will be discussed in detail in Sect. 5.5.

4.3. Extended emission

In this section we present the spectral index distribution of the extended emission which we obtained from the total power maps. In all spectral index maps the nuclear point source has not been subtracted and shows up as a circular region of very flat spectral index ($\alpha < 0.5$) in the center. In Fig. 9 we present the $\lambda 90$ cm/ $\lambda 6.2$ cm spectral index map. To combine the two maps we convolved the $\lambda 6.2$ cm map with a Gaussian in order to

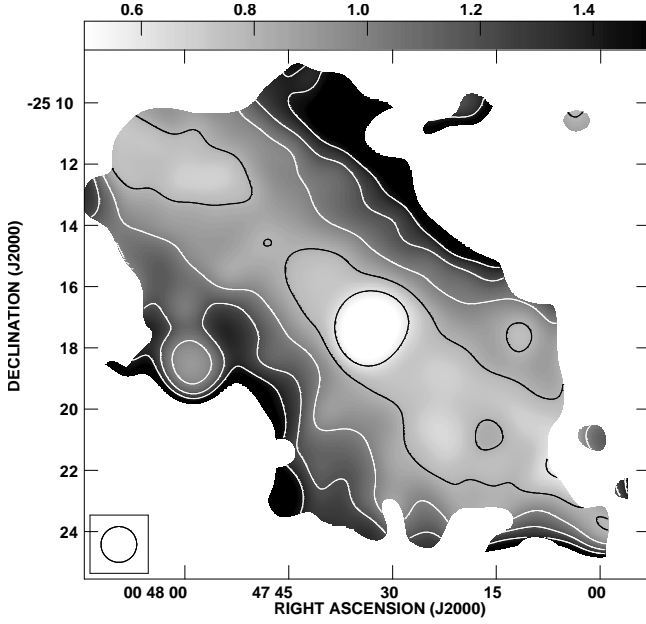


Fig. 9. Spectral index distribution $\lambda 90/6.2$ cm with $70''$ resolution (HPBW). Contours are at 0.6, 0.8, 1.0, 1.2, and 1.4.

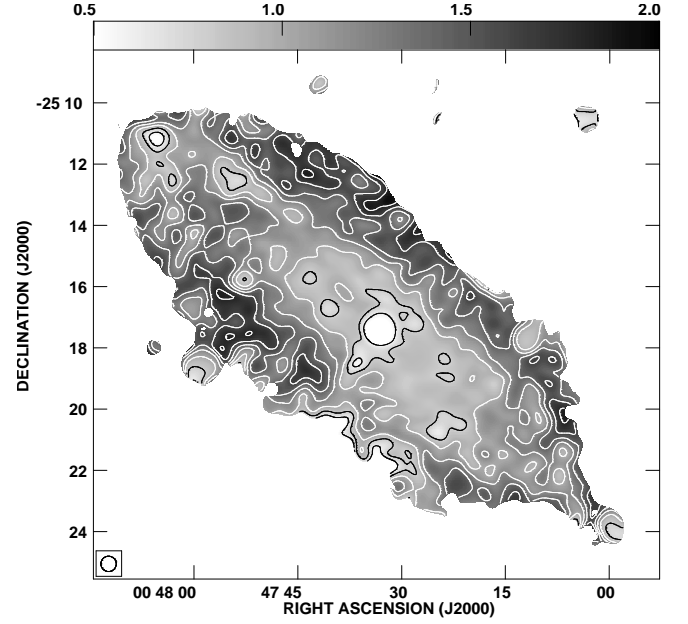


Fig. 10. Spectral index distribution $\lambda 20$ cm/ $\lambda 6.2$ cm with $30''$ resolution (HPBW). Contours are at 0.6, 0.8, 1.0, 1.2, 1.4, 1.6, and 1.8.

match the clean Gaussian beam with $70''$ HPBW of the $\lambda 90$ cm map. At this low resolution the inner disk and the spiral arms are not resolved. We find that the spectral index gradually steepens with increasing distance from the major axis, with the gradient strongest in the inner part of the disk. The spectral index distribution perpendicular to the major axis will be investigated in Sect. 5.5. There is a slight trend which shows the western part to possess a flatter spectral index than the eastern part. At the southern tip of the southeastern spur is a point source which shows up by its flat spectral index of $\alpha_{LS} = 0.84$ compared with the steep spectral in the halo.

The higher resolution $\lambda 20$ cm/ $\lambda 6.2$ cm spectral index map presented in Fig. 10 reveals more detail. The spiral arms are well resolved and show a flatter spectral index than the inter-arm regions. In addition the inner disk has a notable plateau with a flat spectral index of $6'$ extent along the major axis. This spectral index flattening is caused by young cosmic rays accelerated in supernovae remnants of star forming regions. Moreover, we find regions of very steep spectral index ($\alpha > 1$) at the base of the large radio spur southeast of the nucleus and at the northeast extension. That finding agrees well with the $\lambda 90$ cm/ $\lambda 6.2$ cm spectral index map presented above.

The $\lambda 90$ cm/ $\lambda 3.6$ cm spectral index map presented in Fig. 11 has the lowest resolution of our spectral index maps with $84''$ (HPBW). The morphology of this map is similar to the $\lambda 20$ cm/ $\lambda 6.2$ cm map even though smoothed out in comparison. The spectral index is very flat in the inner disk and in the spiral arms with $\alpha < 0.7$. Limited by the sensitivity of the $\lambda 3.6$ cm map we find only four small extensions with extra-planar spectral indices, which are steeper than in the disk. The exception is the extension north-west of the nucleus with a flatter spectral index which can be explained by a point source (RA: $00^h47^m12^s.09$, Dec: $-25^\circ17'45''.0$) with a flat spectral index of $\alpha = 0.68$ embedded in the extended emission (see Tab. 2).

The comparison between the $\lambda 20$ cm/ $\lambda 6.2$ cm and the $\lambda 90$ cm/ $\lambda 3.6$ cm is a good check how reliable the maps are, because both maps have been obtained from independent observations. We find a good correlation of the minimum (i.e. flat

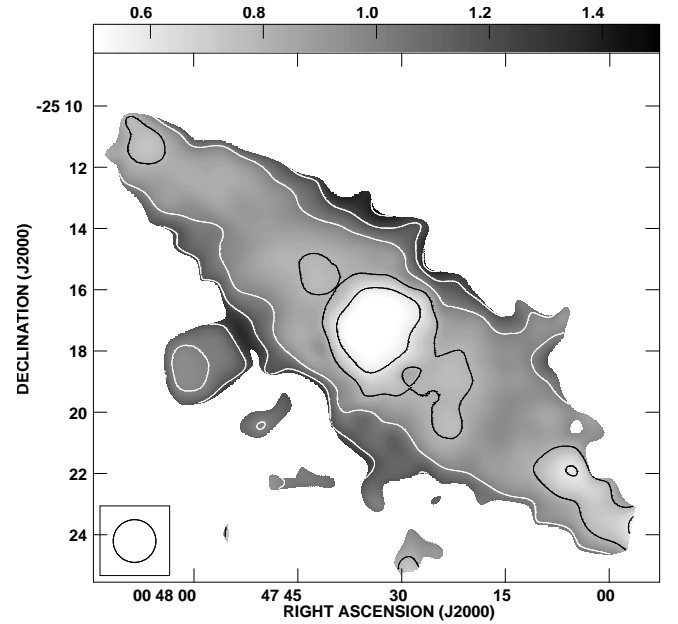


Fig. 11. Spectral index distribution $\lambda 90$ cm/ $\lambda 3.6$ cm with $84''$ resolution (HPBW). Contours are at 0.6, 0.8, 1.0, 1.2, and 1.4

spectral index) at the locations of the inner disk and the spiral arms. However, the steepening of the spectral index with increasing distance from the disk is not found in the $\lambda 20$ cm/ $\lambda 6.2$ cm map. In fact we find in the southwestern part a region where the spectral index ($\alpha \approx 0.5$) is very flat in disagreement with the $\lambda 90$ cm/ $\lambda 3.6$ cm map. Further investigation of the vertical spectral index profiles (see Sect. 5.5) confirms that the spectral index decreases with increasing distance to the disk. This observation contradicts the theory of strong synchrotron losses of the CREs transported away from the disk into the halo (see Sect. 5.5). Hence, we conclude that the $\lambda 20$ cm map suffers from missing zero-spacing flux even though the effect is much smaller than

at $\lambda 6.2$ cm because the primary beam is larger. As the missing zero-spacing flux of the $\lambda 6.2$ cm map has been filled up with the Effelsberg single dish map the flattening of the $\lambda 20$ cm/ $\lambda 6.2$ cm spectral index can be explained by the missing zero-spacing flux at $\lambda 20$ cm.

A map obtained with the Effelsberg telescope could have filled up the missing zero-spacing flux at $\lambda 20$ cm but the demands on very good cleaning are even higher than with the $\lambda 6.2$ cm Effelsberg map, because the beam of the Effelsberg telescope at $\lambda 20$ cm is $8'$ (HPBW). Therefore we decided to use the $\lambda 90$ cm/ $\lambda 6.2$ cm to study the vertical spectral index profiles. This also provides a higher accuracy because of the larger wavelength difference.

5. Cosmic ray transport

In this section we will investigate the CR transport. The main assumption that we make is that all CRs are created and accelerated in the disk. We can thus investigate the transport of CRs perpendicular to the disk. As we have shown there is extra-planar emission (the radio halo). The CRs must have been transported from the disk into the halo. At the same time the CREs are subject to several energy losses. This connection can be used to determine the CR bulk speed in Sect. 5.4.

5.1. The thick radio disk

The disk of NGC 253 has an inclination angle of $i = 78.5^\circ$. Thus any emission profile taken perpendicular to the disk is the superposition of disk and halo emission. This effect is increased by beam smearing which would cause even an infinitely thin disk to show extra-planar emission. In order to simulate this effect we compressed the total power emission profile along the major axis with the aspect ratio of the inclination $\cos(i) = 0.199$ and convolved the profile with a Gaussian to the observed clean beam of $30''$. The resulting profile was fitted with a Gaussian of $1.21'$ Half Power Beam Width (HPBW). This value is slightly larger what a simple estimate provides: the HPBW of the major axis profile is $5.71'$. Compressing it by the inclination factor we get $1.14'$. The excess can be understood as the beam convolution which smoothes out the profile even more. Hence, any emission profile perpendicular to the disk that does not exceed this *effective beam size* cannot be attributed to extra-planar emission but is just the observed inclined emission of the disk.

For the following analysis of the extended emission at $\lambda 6.2$ cm we subtracted all point sources with Gaussian fits from the total power map. The emission profiles were obtained using a strip integration perpendicular to the major axis. The width of the strips is $1.5'$ with a point separation of $0.25'$. The coordinates of the center strip positions are listed in Tab. 5. With the fitting routine presented in Dumke et al. (1995) profiles consisting of two exponential functions were extracted taking the effective beam size into account. Each fit yields a scaleheight of the thin and the thick radio disk for the northern and the southern hemisphere, respectively (see Tab. 6). The corresponding total power profiles with the fitted exponential profiles for the strips are presented in Fig. 12. We note that we are observing only the projection of the perpendicular emission where we neglect the correction of 2 percent at the inclination angle of 78.5° . Taking the mean scaleheight of all strips we find at $\lambda 6.2$ cm a scaleheight for the thin radio disk of $0.3'$ (0.3 kpc) and for the thick radio disk of $1.48'$ (1.70 kpc). This values agree well with the scaleheights reported for other galaxies Krause (2004) at the same wavelength.

The measured scaleheight of the thick radio disk proves the finding of extra-planar emission which proves thereby the existence of a radio halo.

Table 5. Center coordinates of the the strip integration perpendicular to the major axis.

| | R.A. | Dec. |
|-----------------------|---|----------------|
| x_1, \tilde{x}_1 | 00 ^h 48 ^m 10 ^s .95 | −25° 09' 54".5 |
| x_2 | 00 ^h 48 ^m 06 ^s .23 | −25° 10' 49".9 |
| x_3, \tilde{x}_2 | 00 ^h 48 ^m 01 ^s .50 | −25° 11' 45".3 |
| x_4 | 00 ^h 47 ^m 56 ^s .77 | −25° 12' 40".8 |
| x_5, \tilde{x}_3 | 00 ^h 47 ^m 52 ^s .04 | −25° 13' 36".2 |
| x_6 | 00 ^h 47 ^m 47 ^s .31 | −25° 14' 31".8 |
| x_7, \tilde{x}_4 | 00 ^h 47 ^m 42 ^s .59 | −25° 15' 27".0 |
| x_8 | 00 ^h 47 ^m 37 ^s .86 | −25° 16' 22".4 |
| x_9, \tilde{x}_5 | 00 ^h 47 ^m 33 ^s .13 | −25° 17' 17".8 |
| x_{10} | 00 ^h 47 ^m 28 ^s .40 | −25° 18' 13".2 |
| x_{11}, \tilde{x}_6 | 00 ^h 47 ^m 23 ^s .67 | −25° 19' 08".6 |
| x_{12} | 00 ^h 47 ^m 18 ^s .95 | −25° 20' 04".0 |
| x_{13}, \tilde{x}_7 | 00 ^h 47 ^m 14 ^s .22 | −25° 20' 59".4 |
| x_{14} | 00 ^h 47 ^m 09 ^s .49 | −25° 21' 54".8 |
| x_{15}, \tilde{x}_8 | 00 ^h 47 ^m 04 ^s .76 | −25° 22' 50".3 |
| x_{16} | 00 ^h 47 ^m 00 ^s .03 | −25° 23' 45".7 |
| x_{17}, \tilde{x}_9 | 00 ^h 46 ^m 55 ^s .31 | −25° 24' 41".1 |

The strips with $90''$ width are denoted by $x_1 \dots x_{17}$ whereas the wide strips with $180''$ are denoted by $\tilde{x}_1 \dots \tilde{x}_9$. A sketch of the thin strips can be found in Fig. 15 as an overlay on the map of the total magnetic field strength.

The same analysis was carried out at $\lambda 20$ cm and $\lambda 90$ cm, where the effective beam sizes are $1.2'$ and $2.1'$, respectively. The scaleheights of $\lambda 20$ cm are presented in Tab. 7, with a mean of 0.4 kpc (0.5 kpc) for the thin radio disk and $1.3'$ (1.5 kpc) for the thick radio disk. The corresponding total power profiles along with the fits are presented in Fig. 13. The total power profiles for $\lambda 90$ cm could be best described by a single exponential function, which means only a thick radio disk is observed. The scaleheights are found in Tab. 8 and the corresponding profiles along with the fits are presented in Fig. 14. For these profiles we find a mean scaleheight of the thick radio disk of $2.2'$ (2.5 kpc).

Table 8. Local scaleheights of the total power emission at $\lambda 90$ cm with the synchrotron lifetime computed using the magnetic field strength presented in Tab. 6.

| strip | \tilde{h}_N | \tilde{h}_S | h_{Syn} | $t_{\text{Syn},0}$ [10^6 yr] |
|----------|-----------------|---------------|------------------|---------------------------------|
| x_3 | 1.3 ± 0.3 | 2.3 ± 0.2 | 1.8 ± 0.5 | 59 ± 8 |
| x_4 | 3.4 ± 0.3 | 1.6 ± 0.3 | 2.5 ± 0.9 | 59 ± 8 |
| x_5 | 4.6 ± 0.4 | 3.9 ± 0.1 | 4.3 ± 0.3 | 57 ± 7 |
| x_6 | 3.0 ± 0.1 | 3.6 ± 0.1 | 3.3 ± 0.3 | 44 ± 4 |
| x_7 | 2.05 ± 0.10 | 2.1 ± 0.2 | 2.1 ± 0.2 | 34.3 ± 2.7 |
| x_8 | 1.6 ± 0.3 | 1.2 ± 0.2 | 1.4 ± 0.3 | 29.6 ± 2.7 |
| x_9 | 1.5 ± 0.1 | 1.4 ± 0.2 | 1.5 ± 0.2 | 27 ± 3 |
| x_{10} | 1.2 ± 0.2 | 1.7 ± 0.2 | 1.5 ± 0.3 | 28.4 ± 2.7 |
| x_{11} | 1.6 ± 0.1 | 1.6 ± 0.2 | 1.6 ± 0.2 | 33.1 ± 2.7 |
| x_{12} | 1.9 ± 0.1 | 2.1 ± 0.2 | 2.0 ± 0.2 | 45 ± 5 |
| x_{13} | 2.4 ± 0.3 | 2.7 ± 0.3 | 2.6 ± 0.3 | 59 ± 9 |

Table 6. Local scaleheight of the total power emission at $\lambda 6.2$ cm.

| strip | \tilde{h}_N | \tilde{h}_S | d_N | d_S | h_N | h_S | h_{Syn} | B_0 [μ G] | $t_{\text{Syn},0}$ [10^6 yr] |
|----------|---------------|---------------|-------|-------|-------|-------|-------------------|------------------|---------------------------------|
| x_2 | 0.41 | 0.48 | | 0.18 | 0.41 | 4.96 | 2.69 ± 2.28 | | |
| x_3 | 1.13 | 1.18 | | 0.53 | 2.62 | 2.62 | 2.62 ± 0.3 | 9.07 ± 0.14 | 15.4 ± 2.1 |
| x_4 | 0.86 | 2.00 | 0.29 | 0.05 | 1.52 | 2.01 | 1.77 ± 0.24 | 9.88 ± 0.17 | 15.4 ± 2.1 |
| x_5 | 1.00 | 1.53 | 0.30 | 0.21 | 1.88 | 1.57 | 1.73 ± 0.16 | 10.09 ± 0.19 | 14.8 ± 2.1 |
| x_6 | 1.19 | 0.80 | 0.21 | 0.10 | | 1.22 | $1.21 \pm (0.10)$ | 11.91 ± 0.19 | 11.3 ± 1.1 |
| x_7 | 0.84 | 0.80 | 0.56 | | 1.24 | 0.80 | 1.02 ± 0.22 | 14.19 ± 0.13 | 8.9 ± 0.7 |
| x_8 | 0.72 | 0.45 | | 0.19 | 0.72 | 0.93 | 0.83 ± 0.10 | 15.61 ± 0.16 | 7.7 ± 0.7 |
| x_9 | 0.46 | 0.57 | | 0.29 | 0.98 | 0.72 | 0.72 ± 0.26 | 16.31 ± 0.4 | 7.0 ± 0.8 |
| x_{10} | 0.51 | 0.86 | 0.15 | 0.32 | 0.93 | 1.38 | 1.16 ± 0.22 | 16.02 ± 0.26 | 7.4 ± 0.7 |
| x_{11} | 0.72 | 0.96 | 0.46 | 0.34 | 0.98 | 1.46 | 1.22 ± 0.24 | 14.51 ± 0.06 | 8.6 ± 0.7 |
| x_{12} | 1.16 | 1.25 | 0.21 | 0.57 | 1.31 | 1.62 | 1.47 ± 0.15 | 11.75 ± 0.04 | 11.7 ± 1.3 |
| x_{13} | 1.70 | 1.45 | | | 1.70 | 1.45 | 1.58 ± 0.13 | 9.71 ± 0.12 | 15.2 ± 2.3 |
| x_{14} | 1.81 | 0.91 | 0.07 | | 1.99 | 0.92 | 1.46 ± 0.53 | 8.97 ± 0.53 | 17.0 ± 6 |
| x_{15} | | 0.50 | 0.12 | | 1.99 | | 1.25 ± 0.74 | | |

The scaleheights obtained from the one-component exponential fits are \tilde{h}_N in the northern and \tilde{h}_S in the southern hemisphere, respectively. The two-component exponential fits resulted in the scaleheight of the thin radio disk d_N and d_S and the thick radio disk h_N and h_S in the northern and in southern hemisphere, respectively. The mean scaleheight h of the thick radio disk, the maximum of the total magnetic field strength B_0 , and minimum of the local synchrotron CRE lifetime $t_{\text{Syn},0}$ are also included (see text).

Table 7. Local scaleheights of the total power emission at $\lambda 20$ cm and the synchrotron lifetime computed using the magnetic field strength presented in Tab. 6.

| strip | \tilde{h}_N | \tilde{h}_S | d_N | d_S | h_N | h_S | h_{Syn} | $t_{\text{Syn},0}$ [10^6 yr] |
|----------|---------------|---------------|-------|-------|-------|-------|------------------|---------------------------------|
| x_2 | 0.30 | 0.31 | | | 0.26 | 0.31 | | |
| x_3 | 0.86 | 0.68 | | | | 0.72 | 0.79 | 28.2 ± 4 |
| x_4 | 1.14 | 1.07 | 0.37 | 0.58 | 1.76 | 1.33 | 1.6 ± 0.2 | 28.2 ± 4 |
| x_5 | 1.24 | 2.06 | 0.44 | | 3.15 | | 2.6 ± 0.5 | 27.1 ± 3 |
| x_6 | 1.05 | 1.15 | 0.82 | 0.58 | 1.68 | 6.38 | 1.8 ± 0.1 | 20.7 ± 2 |
| x_7 | 0.89 | 0.89 | 0.68 | 0.11 | 1.19 | 1.25 | 1.2 ± 0.1 | 16.3 ± 1.2 |
| x_8 | 0.92 | 0.42 | | 0.11 | 0.92 | 1.32 | 1.2 ± 0.3 | 14.1 ± 1.3 |
| x_9 | 0.53 | 0.44 | 0.36 | 0.55 | 1.03 | 1.71 | 1.1 ± 0.1 | 12.8 ± 1.5 |
| x_{10} | 0.54 | 0.76 | 0.41 | 0.14 | 0.98 | 0.83 | 0.9 ± 0.1 | 13.5 ± 1.3 |
| x_{11} | 0.81 | 0.79 | | 0.53 | | 0.96 | 0.9 ± 0.1 | 15.7 ± 1.3 |
| x_{12} | 1.10 | 1.07 | | 0.20 | 1.09 | 1.29 | 1.2 ± 0.1 | 21.4 ± 2.4 |
| x_{13} | 1.00 | 1.20 | | | 1.04 | 1.20 | 1.1 ± 0.1 | 27.8 ± 4 |
| x_{14} | 0.58 | 0.78 | | 0.18 | 0.49 | 1.27 | 0.8 ± 0.3 | 31 ± 11 |
| x_{15} | 1.02 | 0.92 | | | | | 1.0 ± 0.1 | |

5.2. The total magnetic field

From the nonthermal total power emission one can determine the total magnetic field strength assuming equipartition between the energy density of the CRs and the magnetic field. We used the revised equipartition formula by Beck & Krause (2005) assuming a pathlength of 6.35 kpc, a non-thermal spectral index of $\alpha_{\text{nt}} = 1.0$, a fractional polarization of 5.5 % (the ratio of the flux density of the polarized emission to that of the total power emission, see Paper II), and a proton to electron ratio of $K = 100$. We stress that the last assumption might not be well fulfilled at large distances from the disk, because the CREs suffer high synchrotron losses whereas the CR protons are almost unaffected. Hence, the observed K factor increases with increasing distance from the CR sources which are located in the disk. The magnetic field strength is then underestimated as we observe only the synchrotron emission of the electrons.

The structure of the regular magnetic field is a superposition of a disk-parallel and a vertical component (see Paper II). The disk-parallel component is a spiral following the structure of the galaxy and has the same inclination angle as the disk. The vertical component is orientated perpendicular to the disk. The

above presented parameters as well as the geometry of the magnetic field were assumed to be constant when computing the total magnetic field strength. To check the sensitivity of this assumption we varied the parameters in a certain range and observed its influence on the total magnetic field strength. We used an integration path length between 5 kpc and 20 kpc, a fractional polarization between 5 % and 20 %, a nonthermal spectral index between 0.8 and 1.2, and assumed once a disk-parallel field and once a vertical field. The first one describes the geometry of the magnetic field structure in the disk, where all possible magnetic field directions along the line of sight are taken into account. The second one describes the geometry of the magnetic field in the halo where a constant magnetic field direction along the line of sight is assumed. The variation of the total magnetic field strength in this range of conditions was found to be 20 %, which we thus adopt as an estimate for the systematic error of the total magnetic field strength. The total magnetic field strength was then scaled with the nonthermal synchrotron intensity I_n using the standard equipartition textbook formula:

$$B \propto I_n^{1/(3+\alpha_{\text{nt}})}. \quad (1)$$

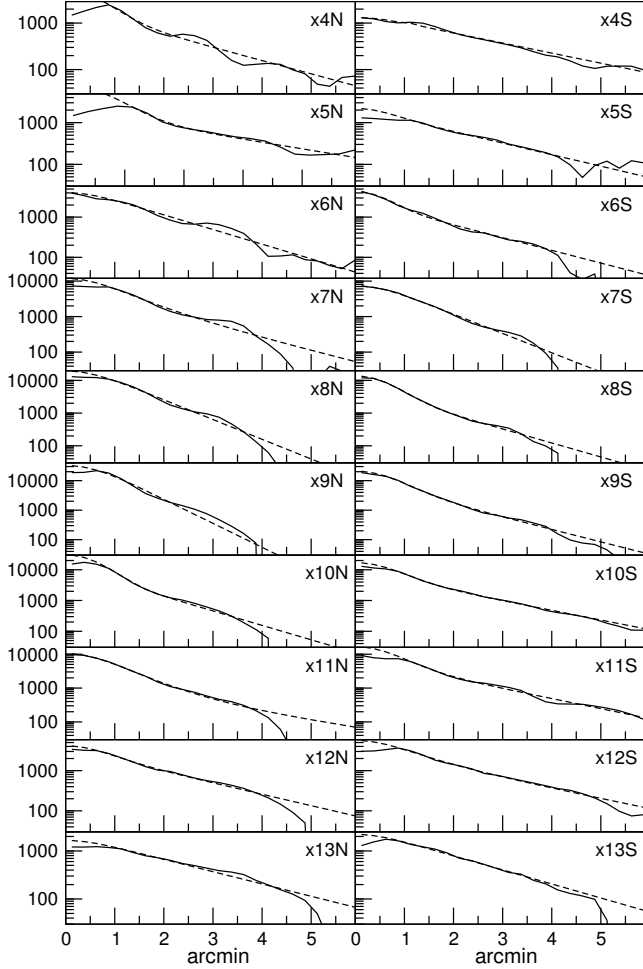


Fig. 12. Total power emission profiles at $\lambda 16.2$ cm perpendicular to the disk obtained from the strip integration ranging from x_4 (top) to x_{13} (bottom) for the northern (left) and southern hemisphere (right), respectively. The solid line shows the measured profile and the dashed line shows the fitted distribution consisting of two exponential functions.

The total magnetic field strength ranges from $5 \mu\text{G}$ to $25 \mu\text{G}$ with the highest field strength located in the center of the disk. Note the subtracted nucleus which is highlighted by a notable residual hole in the center of the map which we present in Fig. 15. The strip integration as described above applied on the map of the total magnetic field strength was used in order to find the maximum of the total magnetic field strength B_0 in each strip. This gives a lower time limit on the lifetime of the CREs as described in the next section.

5.3. Loss processes of the cosmic ray electrons

There are several significant processes through which the CREs lose energy and which have different timescales. These are synchrotron radiation, inverse Compton (IC) losses, nonthermal bremsstrahlung, ionization losses, and adiabatic losses. The timescales determine the lifetimes of the CREs after they have lost a considerable fraction of their energy. In order to calculate the timescales we adopt here the equations by Pohl (1990). The synchrotron lifetime of CREs is

$$t_{\text{syn}} = 8.352 \times 10^9 E(\text{GeV})^{-1} B(\mu\text{G})^{-2} \text{ yr}, \quad (2)$$

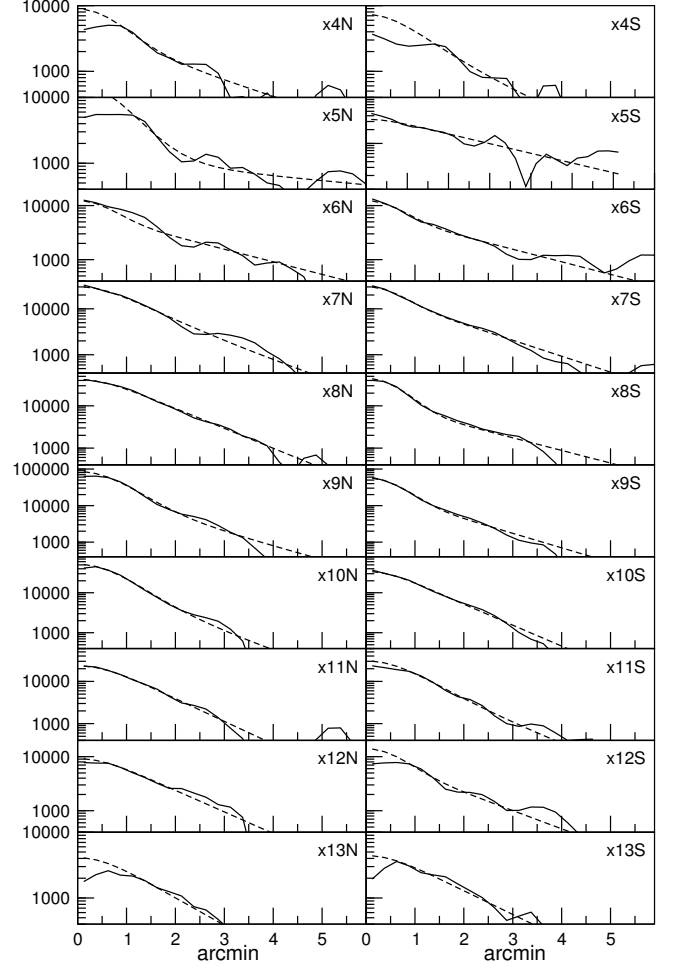


Fig. 13. Total power emission profiles at $\lambda 120$ cm perpendicular to the disk obtained from the strip integration ranging from x_4 (top) to x_{13} (bottom) for the northern (left) and southern hemisphere (right), respectively. The solid line shows the measured profile and the dashed line shows the fitted distribution consisting of two exponential functions.

where E is the CRE energy and B is the total magnetic field strength. We now use the textbook relation between the CRE energy E and the observing frequency ν , dependent on the total magnetic field strength B :

$$E(\text{GeV}) = (\nu / (16.1 \text{ MHz}))^{1/2} B(\mu\text{G})^{-1/2}. \quad (3)$$

For the $\lambda 16.2$ cm observations with $\nu = 4855 \text{ MHz}$ and a typical magnetic field strength of $15 \mu\text{G}$ we find $E = 4.5 \text{ GeV}$ and hence $t_{\text{syn}} = 8.2 \times 10^6 \text{ yr}$. Inverse Compton (IC) radiation losses have the same energy dependency as synchrotron losses and the corresponding lifetime reads

$$t_{\text{IC}} = 3.55 \times 10^8 (E(\text{GeV}))^{-1} (w / (10^{-12} \text{ erg cm}^{-3}))^{-1} \text{ yr}, \quad (4)$$

where w is the photon energy density. From the infrared observations of Radovich et al. (2001) we find a photon energy density of $1.3 \times 10^{-12} \text{ erg cm}^{-3}$, which leads to $t_{\text{IC}} = 6.1 \times 10^7 \text{ yr}$ using again $E = 4.5 \text{ GeV}$. This is almost a magnitude larger than the synchrotron lifetime since the ratio $t_{\text{syn}}/t_{\text{IC}}$ is equal to w/u , where u is the energy density of the magnetic field. From the typical total field strength of $15 \mu\text{G}$ we obtain $u = 9 \times 10^{-12} \text{ erg cm}^{-3}$ which explains why the synchrotron lifetime is considerably shorter than the IC lifetime.

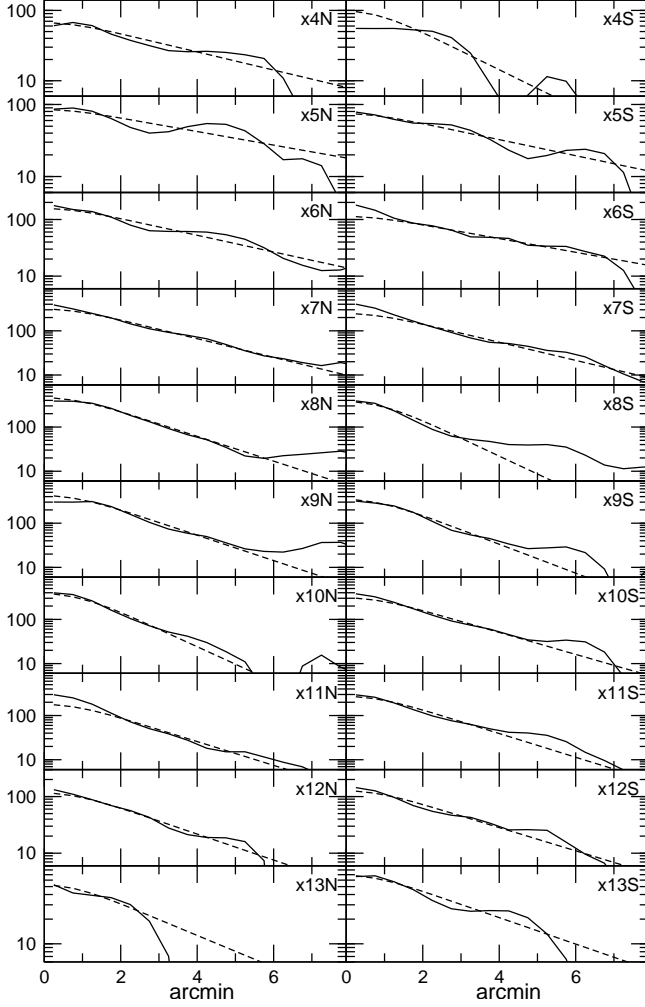


Fig. 14. Total power emission profiles at $\lambda 90$ cm perpendicular to the disk obtained from the strip integration ranging from x_4 (top) to x_{13} (bottom) for the northern (left) and southern hemisphere (right), respectively. The solid line shows the measured profile and the dashed line shows the fitted distribution consisting of one exponential function.

For the nonthermal CRE bremsstrahlung lifetime we use

$$t_{\text{brems}} = 3.96 \times 10^7 n(\text{cm}^{-3})^{-1} \text{ yr}, \quad (5)$$

where n is the gas density of the ISM. The ionization losses lead to a CRE lifetime of:

$$t_{\text{ion}} = 9.5 \times 10^6 n(\text{cm}^{-3})^{-1} E(\text{GeV}) \text{ yr}. \quad (6)$$

We now assume a mean gas column density of $4 M_{\odot} \text{ pc}^{-2}$ for the total gas as determined from the H I observations by Puche et al. (1991). We define a cylinder with the diameter of the disk $D_{25} = 27.7'$ (31.7 kpc) and adopt a height of twice the scale-height of the thick radio disk, or 1.70 kpc. Thus we find a mean density of $\rho = 7.9 \times 10^{-26} \text{ g cm}^{-3}$ or $n \approx 0.05 \text{ cm}^{-3}$. Hence, the bremsstrahlung lifetime is $t_{\text{brems}} = 8 \times 10^8 \text{ yr}$. Using the $15 \mu\text{G}$ as a typical magnetic field strength the CRE energy at $\lambda 6.2 \text{ cm}$ of 4.5 GeV gives a ionization lifetime of $t_{\text{ion}} = 8.6 \times 10^8 \text{ yr}$. The adiabatic timescale depends only on the velocity gradient:

$$t_{\text{ad}} = 3 \left(\frac{dv}{dz} \right)^{-1}. \quad (7)$$

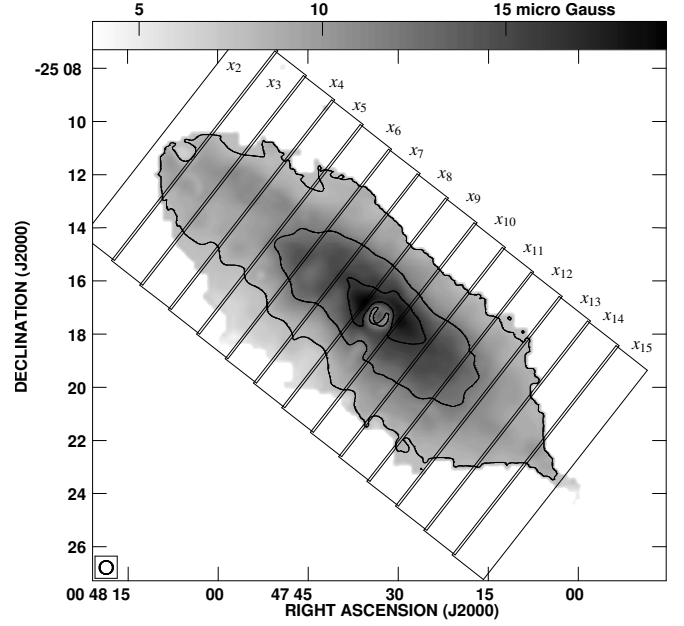


Fig. 15. Map of the total magnetic field strength. Contours are at 8, 12, 16, 20, and $24 \times 1 \mu\text{G}$. The integration strips in order to find the maximum of the magnetic field strength are shown as an overlay.

At this point we do not have any information on the velocity profiles and thus we cannot calculate an estimate for the adiabatic losses which will be discussed later in Sect. 5.

From our estimates in this section we thus conclude that the synchrotron radiation losses are the dominating contribution to the energy losses of the CREs. Hence, we will use the synchrotron lifetime as an upper limit for the CRE lifetime. Using Eq. 2 we constructed a map of the local synchrotron lifetime from the map of the total magnetic field strength. This is Fig. 16. The lifetimes range from $6 \times 10^6 \text{ yr}$ to $25 \times 10^6 \text{ yr}$ with a minimum near the center of the disk and a maximum in the halo. This, of course, only reflects the total magnetic field strength having its maximum in the center of the disk which causes high synchrotron losses and hence a small synchrotron lifetime of the CREs.

The local CRE synchrotron lifetime always overestimates the lifetime of the CR ensemble, because we observe at a certain location the superposition of locally produced CRs and CRs, which have been transported there from their origins. The latter have already lost a fraction of their original energy and thus have shorter lifetimes than indicated by the local synchrotron losses. This becomes obviously more severe with increasing distance from the disk as almost all CRs have been transported away from their origins.

For the determination of the CR bulk speed we used the lifetime at the base of the halo. That means the maximum magnetic field strength B_0 was converted into the minimum local synchrotron lifetime $t_{\text{syn},0}$ using Eq. 2. At the location where the CRE synchrotron lifetime has a minimum we observe the highest fraction of locally produced CRs. Hence $t_{\text{syn},0}$ is the best estimate for the synchrotron lifetime of the CREs transported away from the disk into the halo (see Tab. 6).

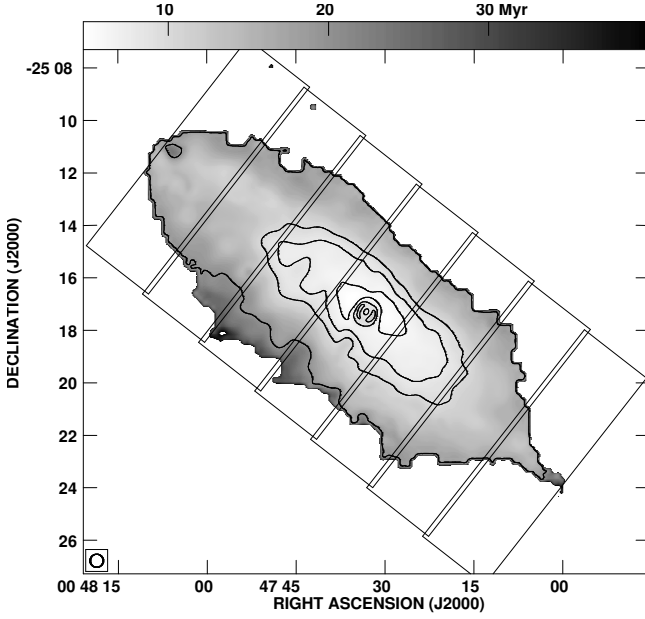


Fig. 16. Map of the local CRE synchrotron lifetime. Contours are at 4, 6, 8, 10, and 20×10^6 yr.

5.4. The cosmic ray bulk speed

In Sect. 3 we found the total power emission to resemble a dumbbell shape at all observed wavelengths. The contour lines show a strong thinning in the center close to the nucleus where we find the brightest part of the disk. The analysis of the scaleheight of the thick radio disk confirms this morphological analysis: it increases with distance from the center with the minimum at the strip at the position of the nucleus. The opposite behavior is found for the magnetic field strength which decreases going from the center to the outer part of the disk. The correlation between the local scaleheight and the local synchrotron lifetime of the CREs can be explained by a CR transport which preferentially proceeds in the vertical direction. In this section we use the following ansatz to calculate the CR bulk speed:

$$v = \frac{h_e}{t_{\text{syn}}}, \quad (8)$$

where h_e is the scaleheight of the CREs, which can be determined using the equipartition condition $n_e \propto B^2$ from the scaleheight of the synchrotron emission h_{syn} :

$$h_e = \frac{3 + \alpha_{\text{nt}}}{2} h_{\text{syn}}. \quad (9)$$

The resulting CR bulk speeds in the individual strips are presented in Tab. 9. The mean bulk speeds are $\bar{v}_{\lambda 90} = (116 \pm 9) \text{ km s}^{-1}$ for $\lambda 90$ cm, $\bar{v}_{\lambda 20} = (136 \pm 14) \text{ km s}^{-1}$ for $\lambda 20$ cm, and $\bar{v}_{\lambda 6.2} = (268 \pm 11) \text{ km s}^{-1}$ for $\lambda 6.2$ cm. The CR bulk speed is almost constant in the northeastern part of the halo in the strips x_5 to x_9 . In the southwestern halo strips x_{10} to x_{13} we find the CR bulk speed to decrease with galactocentric radius. In order to check this observation we plot in Fig. 17 the scaleheight of the thick radio disk for each strip as a function of the synchrotron lifetime. We find a (roughly) linear dependence between the scaleheight of the synchrotron emission h_{syn} and the synchrotron lifetime t_{syn} . Though we present the error bars both in x- and y-direction, for the fit we used only the y-error of the data points.

Table 9. CR bulk speeds in the individual strips.

| strip | $v_{\lambda 90} [\text{km s}^{-1}]$ | $v_{\lambda 20} [\text{km s}^{-1}]$ | $v_{\lambda 6.2} [\text{km s}^{-1}]$ |
|----------|-------------------------------------|-------------------------------------|--------------------------------------|
| x_3 | 68 ± 28 | 64 | 400 ± 100 |
| x_4 | 92 ± 48 | 130 ± 40 | 260 ± 80 |
| x_5 | 170 ± 32 | 220 ± 60 | 270 ± 60 |
| x_6 | 170 ± 30 | 200 ± 30 | 250 ± 40 |
| x_7 | 138 ± 28 | 170 ± 30 | 260 ± 80 |
| x_8 | 106 ± 32 | 200 ± 60 | 250 ± 40 |
| x_9 | 126 ± 30 | 200 ± 40 | 240 ± 120 |
| x_{10} | 120 ± 36 | 160 ± 30 | 360 ± 100 |
| x_{11} | 110 ± 22 | 130 ± 26 | 320 ± 100 |
| x_{12} | 100 ± 22 | 128 ± 26 | 300 ± 60 |
| x_{13} | 100 ± 26 | 90 ± 22 | 240 ± 60 |
| x_{14} | | 60 ± 40 | 200 ± 140 |

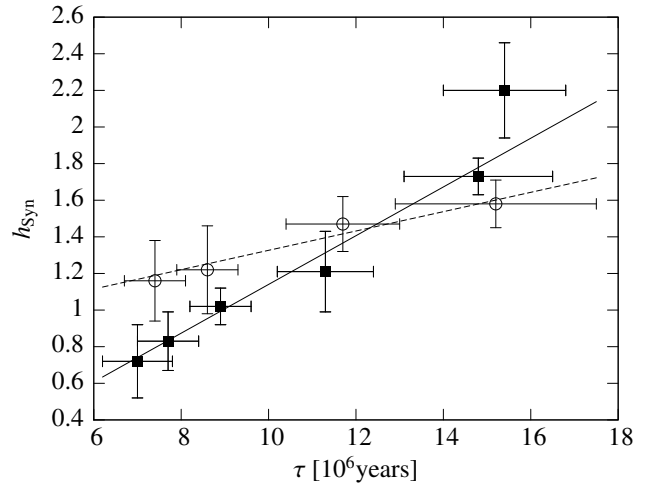


Fig. 17. The scaleheight h of the total power emission at $\lambda 6.2$ cm versus the minimum of the CRE synchrotron lifetime $t_{\text{syn},0}$. The filled triangles are for the northeastern part and the squares for the southwestern part. The linear correlation requires a constant velocity of the galactic wind.

The slope of the curve can be interpreted as the bulk speed of the CRs.

Thus from the slope of the fitting curve we find the CRE bulk speed using:

$$v_e = \frac{3 + \alpha_{\text{nt}}}{2} \frac{\Delta h_e}{\Delta t_{\text{syn}}}. \quad (10)$$

Taking the nonthermal spectral index again as $\alpha_{\text{nt}} = 1$ we find a CR bulk speed at $\lambda 6.2$ cm of $(300 \pm 30) \text{ km s}^{-1}$ for the northeastern halo and $(120 \pm 20) \text{ km s}^{-1}$ for the southwestern halo (see Fig. 17). For $\lambda 20$ cm we find $(220 \pm 20) \text{ km s}^{-1}$ and $(38 \pm 2) \text{ km s}^{-1}$, respectively (Fig. 18), and for $\lambda 90$ cm we find $(234 \pm 22) \text{ km s}^{-1}$ and $(82 \pm 6) \text{ km s}^{-1}$, respectively (Fig. 19).

The close relation between scaleheight and synchrotron lifetime explains the observed pattern of the dumbbell total power emission. In the center of the galaxy the magnetic field strength is highest and hence the synchrotron lifetime is smallest; this hampers the transport of CREs into the halo. This effect even overcomes the excess of emission in the center. The contour lines thus show a neck in the center above and below the nucleus.

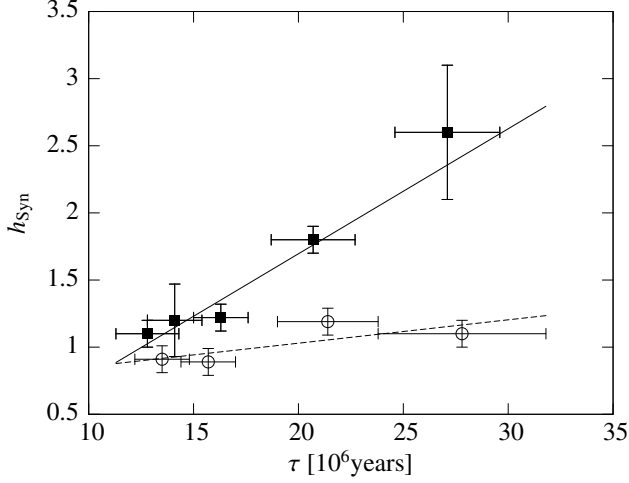


Fig. 18. The scaleheight h of the total power emission at $\lambda 20$ cm versus the minimum of the CRE synchrotron lifetime $t_{\text{syn},0}$. The filled triangles are for the northeastern part and the squares for the southwestern part. The linear correlation requires a constant velocity of the galactic wind.

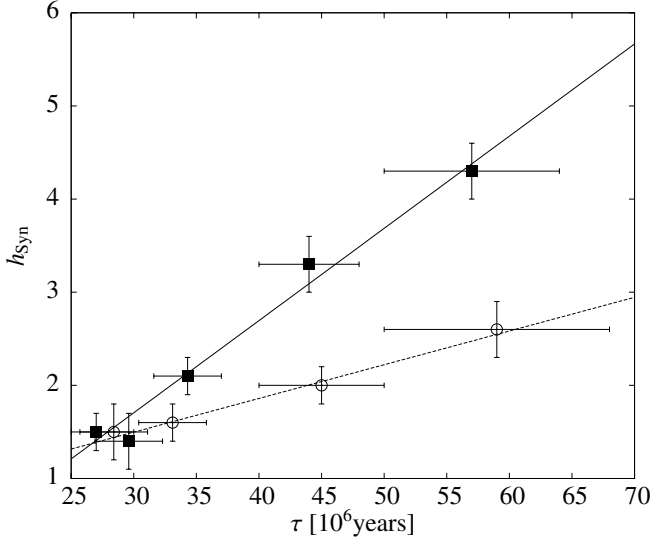


Fig. 19. The scaleheight h of the total power emission at $\lambda 90$ cm versus the minimum of the CRE synchrotron lifetime $t_{\text{syn},0}$. The filled triangles are for the northeastern part and the squares for the southwestern part. The linear correlation requires a constant velocity of the galactic wind.

5.5. Cosmic ray aging

The steepening of the spectral index in the halo suggests radiation losses to be the dominant energy loss of CREs. The total synchrotron emitting power of a single CRE with the energy E reads

$$P = \frac{\sigma_T c B^2}{8\pi} \left(\frac{E}{mc^2} \right)^2, \quad (11)$$

where $\sigma_T = 6.65 \times 10^{-25} \text{ cm}^2$ is the Thomson cross section, B is the total magnetic field strength and $m = 511 \text{ keV}/c^2$ is the electron rest mass. Converting to more practical units gives:

$$P = 1.89 \times 10^{-18} E(\text{GeV})^2 B(\mu\text{G})^2 \text{ GeV s}^{-1}. \quad (12)$$

Replacing the CRE energy with the observing frequency using equation 3 yields the total synchrotron emission of a single CRE at a given frequency ν :

$$P = 1.89 \times 10^{-18} \left(\frac{\nu}{16.1 \text{ MHz}} \right) B(\mu\text{G}) \text{ GeV s}^{-1}. \quad (13)$$

Using the differential equation for the energy $dE/dt = P(E)$ we find the time dependency of the CRE energy as $E(t) = E_0/(1 + t/t_{\text{syn}})$ where the synchrotron lifetime t_{syn} is defined as time where a CRE has lost half of its initial energy E_0 . The total energy radiated away during the time T is found by integrating $\int P \cdot dt = 1/2P \cdot T$. Thus the synchrotron lifetime is defined by $P \cdot t_{\text{syn}} = E$, which reads:

$$t_{\text{syn}} = \frac{8.352 \times 10^9 \text{ yr}}{(\nu/(16.1 \text{ MHz}))^{1/2} B(\mu\text{G})^{3/2}}. \quad (14)$$

The energy dependency of the synchrotron lifetime means that CREs observed at two different observing frequencies ν_1 and ν_2 have a different lifetime. Using the ansatz for the energy time dependency we can construct two energy functions corresponding to the two frequencies:

$$E_1(t) = \frac{E_1}{1 + t/t_1} \quad E_2(t) = \frac{E_2}{1 + t/t_2}. \quad (15)$$

The spectral index α can be computed from the ratio of the two energies:

$$\alpha = \frac{\ln(E_1/E_2)}{\ln(\nu_1/\nu_2)}. \quad (16)$$

Inserting the ansatz from Eq. 15 we find for the spectral index:

$$\alpha(t) = \ln \left(\frac{\nu_2}{\nu_1} \right) \cdot \ln \left(\frac{1 + t/t_2}{1 + t/t_1} \right). \quad (17)$$

Now computing the time derivative for the spectral index we find:

$$\frac{\Delta\alpha}{\Delta t} = \ln \left(\frac{\nu_2}{\nu_1} \right) \cdot \frac{t_1 - t_2}{(t + t_1)(t + t_2)}. \quad (18)$$

For times much shorter than the synchrotron lifetimes $t \ll t_1, t_2$ the derivative is:

$$\frac{\Delta\alpha}{\Delta t} = \ln \left(\frac{\nu_2}{\nu_1} \right) \cdot \left(\frac{1}{t_2} - \frac{1}{t_1} \right). \quad (19)$$

Inserting the synchrotron lifetimes t_1, t_2 for the two observing frequencies from Eq. 13 we find:

$$\frac{\Delta\alpha}{\Delta t} = \frac{B(\mu\text{G})^{3/2}}{\ln(\nu_1/\nu_2) \cdot 8.352 \times 10^9 \text{ yr}} \left(\sqrt{\frac{\nu_2}{16.1 \text{ MHz}}} - \sqrt{\frac{\nu_1}{16.1 \text{ MHz}}} \right). \quad (20)$$

Using the observing frequencies for $\lambda 90$ cm and $\lambda 6.2$ cm which is $\nu_1 = 327.5 \text{ MHz}$ and $\nu_2 = 4855 \text{ MHz}$, respectively, leads to:

$$\frac{\Delta\alpha}{\Delta t} = \frac{5.70 \times 10^{-4}}{10^6 \text{ yr}} B(\mu\text{G})^{3/2} \quad (21)$$

If the time derivative of the spectral index is constant we expect a constant slope for α if the CR bulk speed is constant. Hence,

we can replace the time with the distance z from the disk by $\Delta t = \Delta z/v$. We finally get an expression for the CR bulk speed:

$$v = \frac{\Delta\alpha}{\Delta t} \cdot \left(\frac{\Delta\alpha}{\Delta z}\right)^{-1}. \quad (22)$$

Using the known distance to NGC 253 we find the relation $(1')/(10^6 \text{ yr}) = 1130 \text{ km s}^{-1}$. Hence, we get finally for the bulk speed:

$$v = 0.644 \cdot B(\mu\text{G})^{3/2} \cdot \left(\frac{\Delta\alpha}{\Delta z}\right)^{-1} \text{ km s}^{-1} \text{ arcmin}^{-1}. \quad (23)$$

We have applied a strip integration for the $\lambda 90 \text{ cm}$ map and the $\lambda 6.2 \text{ cm}$ map. The intensity profiles were converted in profiles for the spectral index which are presented in Fig. 20. The spectral index α shows regions of linear slope in almost all profiles. The constant slope can be explained by the constant change of α with time and a constant CR bulk speed v . Using linear fits in the range of $z = (1.25 \dots 4.75)'$ the slope of the decreasing spectral index with regard to the increasing distance z from the disk $\Delta\alpha/\Delta z$ has been derived which gives the CR bulk speed using Eq. 23. Table 10 lists the results for each profile and the northern and southern hemisphere respectively. The mean cosmic ray bulk speed derived from the spectral index slope is $170 \pm 70 \text{ km s}^{-1}$.

Table 10. Decrease of the spectral index α between $\lambda 90 \text{ cm}$ and $\lambda 6.2 \text{ cm}$ with increasing distance from the disk.

| strip | $\Delta\alpha/\Delta z _N$ | $\Delta\alpha/\Delta z _S$ | B_0 | $v_N[\text{km s}^{-1}]$ | $v_S[\text{km s}^{-1}]$ |
|---------------|----------------------------|----------------------------|-------|-------------------------|-------------------------|
| \tilde{x}_3 | -0.22 | -0.12 | 11 | 107 | 196 |
| \tilde{x}_4 | -0.26 | -0.31 | 14 | 130 | 109 |
| \tilde{x}_5 | -0.30 | -0.26 | 17 | 150 | 174 |
| \tilde{x}_6 | -0.16 | -0.12 | 15 | 234 | 312 |
| \tilde{x}_7 | -0.10 | -0.20 | 10 | 204 | 102 |

The slope has been derived by linear fits of the profiles presented in Fig. 20 for the northern (N) and southern hemisphere (S). The adopted magnetic field strength $B_0(\mu\text{G})$ and the cosmic ray propagation speed according to Eq. 23 are presented, too.

6. Discussion

6.1. Cosmic ray transport

The linear *local* correlation between the scaleheight and the CRE synchrotron lifetime allows us to draw some conclusions: the transport of CRs proceeds predominantly perpendicular to the disk. The diffusion timescale along the disk is much larger than the synchrotron lifetime of the CREs: $\tau_{\text{syn}} \ll \tau_{\text{diff},\perp}$. Here, $\tau_{\text{diff},\perp}$ denotes the diffusion timescale perpendicular to the magnetic field where we assume that a significant poloidal magnetic field component perpendicular to the disk exists. This will be shown in Paper II where we analyze the large scale magnetic field component using the polarization measurements. Here, we use a heuristic argumentation: if the CRs would diffuse freely in the disk, we would not expect any correlation between the scaleheight and the synchrotron lifetime estimated in the *underlying* disk. This is because in a free diffusive transport with no preferred transport direction the CRs would be equally distributed over the entire disk. Dahlem et al. (1995) showed that the CR distribution also depends on the underlying star formation, which

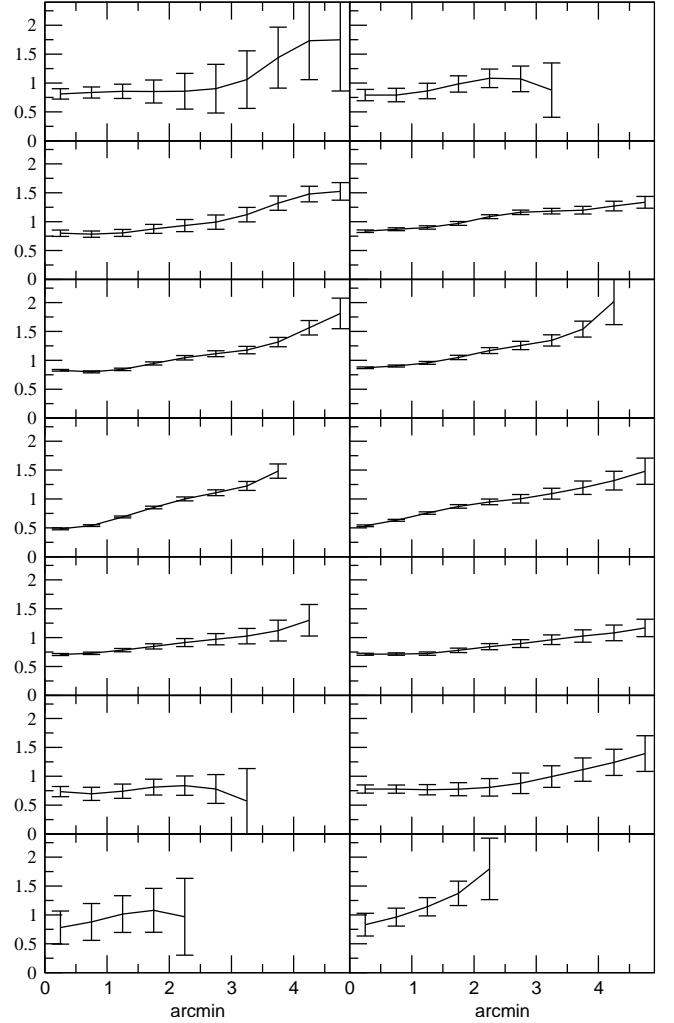


Fig. 20. Spectral index profiles $\lambda 90 \text{ cm}/\lambda 6.2 \text{ cm}$ perpendicular to the disk as a function of distance to the major axis. The strips are ranging from \tilde{x}_2 (top) to \tilde{x}_8 (bottom) for the northern (left) and southern hemisphere (right). The solid line is the connection of the points in order to highlight the decrease of the spectral index with increasing distance from the disk. For the position of the strips see Tab. 5.

supports a connection to the disk (see also Dahlem et al. 2006). Hence, the CR transport proceeds predominantly along the large scale magnetic field connecting the disk with the halo. The confinement along the poloidal magnetic field suppresses the diffusion perpendicular to it.

The confinement along the poloidal magnetic field motivates a one-dimensional description of the CR transport by the combined diffusion and convection equation. The contribution of either of these processes can dominate, which would be called diffusive or convective CR transport. From our observations we cannot make a clear decision which of these processes is dominating in NGC 253. Several arguments can be made:

1. The profiles of the total power radio continuum emission can be described by a power law even to the extent of several scaleheights from the disk. In the case of purely diffusive CR transport Gaussian profiles are expected (Schlickeiser 2007). This is not observed in any of the strips presented in Sect. 5.1.

2. The CR bulk speed is a function of the observing wavelength and thus of the CRE energy. This is in agreement with a diffusive transport and a diffusion coefficient which depends on the energy.
3. The CR bulk speed in the northeastern halo is independent of the height above the disk. This is in agreement with convection dominated transport. However, we find that the bulk speed increases with observing frequency, which supports diffusive transport.
4. In the southwestern halo part the CR bulk speed decreases with the height over the disk. This can be explained by diffusion, with the expected scaleheight which is a function of the CRE lifetime with $h_{\text{diff}} = \sqrt{2\kappa t_{\text{syn}}}$, where κ is the diffusion coefficient.

Using the information about the CR transport we can now calculate the adiabatic loss timescale mentioned in Sect. 5.3. The bulk speed of the CRs is 268 km s^{-1} , which has been reached while they are transported from the disk to vertical height of one scale-height (1.7 kpc). The adiabatic timescale is thus $t_{\text{ad}} = 1.9 \times 10^7 \text{ yr}$ using Eq. 7. This timescale is near to the synchrotron lifetime of the CREs. Hence the adiabatic losses have to be considered especially for the lower CRE energies at $\lambda 90 \text{ cm}$. A possible transition of adiabatic loss dominated CR transport to radiative dominated CR transport should be visible in the spectrum as break of flat spectral index at low frequencies to steep spectral index at high frequencies (Pohl & Schlickeiser 1990). In Sect. 4.2 we have seen, however, in the spectrum of the total integrated flux no such spectral break. As the CR transport is different for the northeastern and southwestern halo, it is worthwhile to investigate the spectra of the extended flux in these regions separately. For this we integrated the flux in three strips up to a vertical extent of $5'$ (5.7 kpc), respectively. In the northeastern halo we included the strips x_5 , x_6 , and x_7 , in the central halo the strips x_8 , x_9 , and x_{10} , and in the southwestern halo the strips x_{11} , x_{12} , and x_{13} . The corresponding spectra in Fig. 21 give spectral indices of 0.98, 0.86, and 0.89 between $\lambda 90 \text{ cm}$ and $\lambda 3.6 \text{ cm}$, respectively.

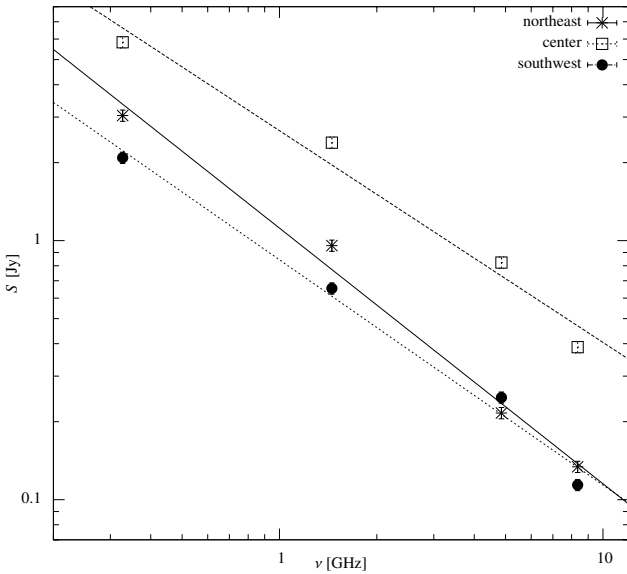


Fig. 21. Spectra for the northeastern halo (circles), the central halo (crosses), and the southwestern halo (squares). The corresponding spectral indices are 0.98, 0.86, and 0.89, respectively.

Of course, the small range of frequencies presented shows no prominent spectral break, because it is smeared out usually in frequency. The spectrum of the central halo however shows a gradually steepening to higher frequencies which is not so clearly seen for the northeastern and southwestern halo. This indication of higher adiabatic losses in the central halo than in the outer halo parts is reasonable as the adiabatic losses depend only on the velocity gradient. Since we have found a constant CR bulk speed throughout the halo the CRs are stronger accelerated in the central halo, where the scaleheights are smaller. Radiative losses are presumably still dominating as the spectral indices between 0.86 and 0.98 are rather steep. Moreover, radiative losses can explain the steepening of the spectral index with increasing distance from the disk (see Sect. 5.5). However, we should keep in mind that other loss processes still contribute and thus the inferred lifetimes of the CREs have to be considered as an upper limit. In turn the CR bulk speeds are only an estimated lower limit.

6.2. Galactic Wind

The halo of NGC 253 contains all different phases of the ISM. One of the most favoured models for the material expelled from the inner parts of NGC 253 is the so-called superwind model in which active star formation drives a thermal outflow. The superbubble explains the huge lobes seen in the $H\alpha$ and soft X-ray emission by limb brightening. The interior of the bubble is filled with hot ionized gas. We now study the possible correlation between the CR bulk speed profiles and the distribution of the extra-planar gas in the halo.

The CR bulk speed of 270 km s^{-1} is near the escape velocity of 280 km s^{-1} which can be computed by $v_{\text{esc}} = \sqrt{2} \cdot \Omega r$. Here, Ωr is the rotation speed of 200 km s^{-1} . Hence, the kinetic energy makes a CR driven galactic wind possible. In this section we use our CR bulk speed investigations in order to discuss in detail the velocity profile of this wind. We will discuss the influence of the galactocentric distance (i.e. the radial velocity profile) and the influence of the height above the disk (i.e. the vertical velocity profile). The mean CR bulk speed is constant in northeastern halo for strips x_5 to x_9 whereas in the southwestern halo the mean bulk speed is gradually decreasing with galactocentric distance for strips x_{10} to x_{13} (see Tab. 9). This can be explained assuming identical vertical bulk speed profiles in the individual strips in the northeastern and southwestern halo, respectively. This would mean that the CR bulk speed is constant for the northeastern part of the halo and thus the wind does neither accelerate nor decelerate. For the southwestern halo we find a decelerating CR bulk speed. From the local correlation between scaleheight and CRE synchrotron lifetime we can even infer the bulk speed at height of one scaleheight above the disk. From Fig. 17 we find a bulk speed of 120 km s^{-1} at $\lambda 6.2 \text{ cm}$ for the southwestern halo part. Hence the CR bulk speed in the southwestern halo at a height of one scaleheight above the disk is significantly smaller than the mean CR bulk speed of 270 km s^{-1} . The decelerating of the wind speed with the height above the disk is hence prominent in the southwestern halo.

The differences in the bulk speed profiles can be found also in the halo gas phases. There is significantly less $H I$ in the southwestern halo part, whereas the northeastern halo contains a huge spur of $H I$ gas extending up to 8 kpc from the disk (Boomsma et al. 2005). The diffusive ionized gas (DIG) traced by $H\alpha$ emission shows a huge prominent plume coinciding well with the radio spur east of the nucleus. The overall extra-planar $H\alpha$ emis-

sion is more prominent in the northeastern halo part (Hoopes et al. 1996). A similar behavior is found for the extra-planar X-ray emission measured with ROSAT. Huge lobes of soft X-ray emission are extending far in the northeastern part of the halo, whereas the southwestern part has much less extra-planar emission (Pietsch et al. 2000). This dichotomy of the extra-planar gas emission can be explained, if the galactic wind sweeps the hot gas from the disk into the halo. The decelerating CR bulk speed in the southwestern halo naturally explains the smaller vertical extent of the hot gas since the mass load is lower than in the northeastern halo. Thus our observations support not only the galactic wind hypothesis but show also convincingly that the wind sweeps along its own luminous matter. A preexisting gaseous halo possibly created by accreting gas from a minor merger with a satellite is thus not necessary. Another fact which supports this picture is that we should expect a lower wind speed in the northeastern halo part where is more extra-planar H I gas. If the H I gas would be preexisting we should expect a decelerating influence of this gas, when the wind collides with these clouds.

Whether the magnetic field or the hot gas determines the dynamical evolution of the disk-wind is connected to the pressures of both ISM phases. Thus we will make an order of magnitude estimate of the pressures of the thermal gas, the kinetic energy, and the magnetic pressure. The electron density of $n_e = 8 \times 10^{-3} \text{ cm}^{-3}$ and the temperature of $T = 3 \times 10^6 \text{ K}$ have been found by Strickland et al. (2002). That results in a thermal pressure of $P_{\text{therm}} = 7 \times 10^{-12} \text{ erg cm}^{-3}$. The lower limit estimated for the outflow velocity is $v = 270 \text{ km s}^{-1}$ which results in a kinetic energy density (i.e. the ram pressure) of $P_{\text{kin}} = 1/2 n_e v^2 = 6 \times 10^{-12} \text{ erg cm}^{-3}$. The magnetic pressure is $P_{\text{mag}} = B^2/(8\pi) = 9 \times 10^{-12} \text{ erg cm}^{-3}$. Hence from this order of magnitude calculations we infer that the thermal pressure, the ram pressure, and the magnetic pressure are in the same order of magnitude. Hence, any of the given contributions has to be taken into account when calculating the dynamical evolution.

The galactic wind must eventually escape from the gravitational potential to the intergalactic medium (IGM). From the observations we cannot make any definite conclusions because we did not observe the transition between the radio halo and the IGM which is located far away from the detected radio halo. However, our measurements suggest that in the southwestern halo the escape from the gravitational potential is not possible, because the wind speed decelerates and drops below the escape velocity of 280 km s^{-1} . In the northeastern halo the wind speed is high enough to reach the IGM and leave the gravitational potential. The wind neither accelerates nor decelerates within the measured vertical height of 6 kpc above the disk.

7. Conclusions

Our radio continuum study of NGC 253 show an extended radio halo at the wavelengths from $\lambda 90 \text{ cm}$ to $\lambda 3.6 \text{ cm}$. Because of its high dynamic range NGC 253 is a difficult target for the radio continuum observations. We treated the high dynamic range with a specially tailored data reduction technique. Our maps presented here are thus essentially noise limited. The combination of our new mosaic with the single-dish in order to fill up the missing zero-spacing flux allowed the study of the extra planar continuum emission with high resolution and sensitivity. The inclusion of the $\lambda 90 \text{ cm}$ and the $\lambda 20 \text{ cm}$ data allowed to put detailed constraints on the CR transport. Our main conclusions from this work are:

1. The scaleheight of the total power emission is a linear function of the CRE synchrotron lifetime in the underlying disk. This can be understood only if the CR transport proceeds preferentially in vertical direction. If the CR transport did not have a preferred direction then the distribution of the extra-planar CRs would be independent of the CRE lifetime in the underlying disk.
2. The steepening of the spectral index, which is a linear function of z , can be explained with dominant radiative losses of the CREs. The contribution of ionization losses and bremsstrahlung losses can be neglected. The adiabatic losses are of the same order as the radiative losses but difficult to estimate.
3. We computed the CR bulk speed as the ratio of the total power scaleheight and the CRE synchrotron lifetime. The estimated lower limit for the global CR bulk speed is 270 km s^{-1} which is near the escape velocity of $v_{\text{esc}} = 280 \text{ km s}^{-1}$.
4. The bulk speed shows a different galactocentric dependence in the northeastern and southwestern halo. In the southwestern halo the bulk speed decreases with the radius whereas in the northeastern halo bulk speed is constant. This can be understood by adopting different vertical bulk speed profiles $v(z)$ for the two halo parts. In the northeastern part the bulk speed is independent of z whereas in the southwestern part the bulk speed decreases with z .
5. The bulk speed profiles are indicative of a predominantly convective CR transport in the northeastern halo and a predominantly diffusive CR transport in the southwestern halo. This can be explained by the action of a galactic wind blowing in the northeastern halo with a higher mass load suggested by the observations of H I, H α and soft X-ray emission away from the disk.

The CR transport however is always the superposition of convective and diffusive contributions. The data presented here provide a good basis for more detailed calculations with the combined diffusion and convection equation. Calculations should include vertical profiles of the magnetic field strength, the CR number density, and the speed of the hot ionized gas.

Acknowledgements. VH would like to thank the organizers of the Graduiertenkolleg GRK 787 and the Sonderforschungsbereich SFB 591 for support and funding during the course of his PhD. The GRK 787 ‘‘Galaxy groups as laboratories for baryonic and dark matter’’ and the SFB 591 ‘‘Universal properties of non-equilibrium plasmas’’ are funded by the Deutsche Forschungsgemeinschaft (DFG).

It is out pleasure to thank Reinhard Schlickeiser for inspiring discussions and Enno Middelberg for comments on the manuscript.

References

- Baars, J. W. M., Genzel, R., Pauliny-Toth, I. I. K., & Witzel, A. 1977, *A&A*, 61, 99
- Beck, R., Biermann, P., Emerson, D. T., & Wielebinski, R. 1979, *A&A*, 77, 25
- Beck, R., Brandenburg, A., Moss, D., Shukurov, A., & Sokoloff, D. 1996, *ARA&A*, 34, 155
- Beck, R., Carilli, C. L., Holdaway, M. A., & Klein, U. 1994, *A&A*, 292, 409
- Beck, R. & Krause, M. 2005, *AN*, 326, 414
- Boomsma, R., Oosterloo, T., Fraternali, F., van der Hulst J.M., & Sancisi, R. 2005, *A&A*, 431, 65
- Braun, R. 1988, *Millimeter Array Memo.*, 46
- Breitschwerdt, D., McKenzie, J. F., & Voelk, H. J. 1991, *A&A*, 245, 79
- Breitschwerdt, D., McKenzie, J. F., & Voelk, H. J. 1993, *A&A*, 269, 54
- Carilli, C. L. 1996, *A&A*, 305, 402
- Carilli, C. L., Holdaway, M. A., Ho, P. T. P., & de Pree, C. G. 1992, *ApJ*, 399, L59
- Dahlem, M., Lisenfeld, U., & Golla, G. 1995, *ApJ*, 444, 119
- Dahlem, M., Lisenfeld, U., & Rossa, J. 2006, *A&A*, 457, 121

- Dumke, M., Krause, M., Wielebinski, R., & Klein, U. 1995, *A&A*, 302, 691
- Emerson, D. T. & Gräve, R. 1988, *A&A*, 190, 353
- Field, G. B., Goldsmith, D. W., & Habing, H. J. 1969, *ApJ*, 155, 149
- Heckman, T. M., Lehnert, M. D., Strickland, D. K., & Armus, L. 2000, *ApJS*, 129, 493
- Heesen, V. 2007, PhD thesis, Ruhr-Universität, Bochum, Germany
- Högbom, J. A. 1974, *A&AS*, 15, 417
- Hoopes, C. G., Walterbos, R. A. M., & Greenwalt, B. E. 1996, *AJ*, 112, 1429
- Ipavich, F. M. 1975, *ApJ*, 196, 107
- Karachentsev, I. D., Grebel, E. K., Sharina, M. E., et al. 2003, *A&A*, 404, 93
- Krause, M. 2004, in *The Magnetized Interstellar Medium*, ed. B. Uyaniker, W. Reich, & R. Wielebinski, 173
- Lehnert, M. D. & Heckman, T. M. 1996, *ApJ*, 472, 546
- Lenc, E. & Tingay, S. J. 2006, *AJ*, 132, 1333
- Mohan, N. R., Anantharamaiah, K. R., & Goss, W. M. 2002, *ApJ*, 574, 701
- Pietsch, W., Vogler, A., Klein, U., & Zinnecker, H. 2000, *A&A*, 360, 24
- Pohl, M. 1990, Master's thesis, Max-Planck-Institut für Radioastronomie, Bonn, Germany
- Pohl, M. & Schlickeiser, R. 1990, *A&A*, 239, 424
- Ptuskin, V. S., Voelk, H. J., Zirakashvili, V. N., & Breitschwerdt, D. 1997, *A&A*, 321, 434
- Puche, D., Carignan, C., & van Gorkom, J. H. 1991, *AJ*, 101, 456
- Radovich, M., Kahanpää, J., & Lemke, D. 2001, *A&A*, 377, 73
- Rottmann, H. 1996, PhD thesis, Friedrichs-Wilhelms-Universität, Bonn, Germany
- Schlickeiser, R. 2007, priv. comm.
- Schulz, H. & Wegner, G. 1992, *A&A*, 266, 167
- Strickland, D. K., Heckman, T. M., Weaver, K. A., & Dahlem, M. 2000, *AJ*, 120, 2965
- Strickland, D. K., Heckman, T. M., Weaver, K. A., Hoopes, C. G., & Dahlem, M. 2002, *ApJ*, 568, 689
- Suchkov, A. A., Balsara, D. S., Heckman, T. M., & Leitherner, C. 1994, *ApJ*, 430, 511
- Zirakashvili, V. N., Breitschwerdt, D., Ptuskin, V. S., & Voelk, H. J. 1996, *A&A*, 311, 113

Cosmic rays and the magnetic field in the nearby starburst galaxy NGC 253: II. The magnetic field structure

Volker Heesen¹, Marita Krause², Rainer Beck², and Ralf-Jürgen Dettmar¹

¹ Astronomisches Institut der Ruhr-Universität Bochum, Universitätsstr. 150, 44780 Bochum, Germany

² Max-Planck Institut für Radioastronomie, Auf dem Hügel 69, 53121 Bonn, Germany

Received jdate_i / Accepted jdate_e

ABSTRACT

Context. There are so far only few known cases where the magnetic field structure has been investigated in the halo of spiral galaxies. The cosmic ray (CR) transport, however, is closely connected with three-dimensional structure of the magnetic field.

Aims. NGC 253 possesses one of the brightest radio halos so far discovered. In the previous paper we found a vertical CR transport with a bulk speed close to the escape velocity. Using radio continuum polarimetry we want to investigate the three-dimensional structure of the large-scale magnetic field.

Methods. The polarization information of the previously presented continuum observations is used to create sensitive maps of the intrinsic magnetic field structure in the disk and halo of NGC 253. The high dynamic range needed because of the strong nuclear point-like source has been addressed in our polarization calibration. The instrumental polarization of the Effelsberg telescope was corrected with the appropriate beam patterns. The mosaic obtained with the VLA required a specially tailored polarization calibration in order to cope with the strong spurious polarization caused by the off-axis location of the nuclear point-like source in the primary beam.

Results. We found an intrinsic magnetic field orientation in the disk, which is disk-parallel only for small galactocentric radii and small distances from the galaxy midplane. The previously known large "radio spur" contains a vertical magnetic field component. The magnetic field in the disk can be well described by an even axisymmetric spiral magnetic field with prescribed inclination and pitch angle. We used that for the decomposition of the large-scale magnetic field into a toroidal and poloidal component. The poloidal magnetic field structure has a distinct "X"-shaped pattern centered on the nucleus which correlates well with the distribution of the extra-planar hot interstellar medium traced by H α and X-ray emission. The expanding superbubble amplifies the large-scale magnetic field by compression while expanding into the extra-planar distribution of cold gas traced by H I emission. The presence of this gas can be explained by a disk wind transporting cold gas from the disk into the halo.

Key words. jkeyword 1 - keyword 2 - keyword 3_e

1. Introduction

There is increasing observational evidence for the existence of gaseous halos around disk galaxies. They consist of different interstellar medium (ISM) species, mainly the diffuse ionized gas, dust, cosmic rays (CRs), and magnetic fields (for a review, see e.g. Dettmar 1992). To explain these halos, various models have been proposed, which all propose a galactic wind driven by supernova explosions as the energy source driving the formation of the halo. The effects of star formation on the ISM are dramatic: the heated gas in supernova remnants (SNRs) and accelerated energetic particles are injected into the base of the halo. The fundamental parameter, which determines the formation of a halo, is therefore the energy input by supernova explosions. Thus, the halo does not form above the entire disk, but only at radial distances where the star formation takes place (Dahlem et al. 1995). Moreover, the compactness of the star forming regions determines the threshold condition where the hot gas can break out against the pull of the gravitational field (Dahlem et al. 2006). This corroborates the picture of the hot gas injected by supernova explosions and stellar winds of massive stars (see e.g. Dettmar & Soida 2006). The transport of the gas from the disk into the halo has been discussed in the past in the form of galactic chimneys (Norman & Ikeuchi 1989) and superbubble blow outs (Mac Low & Ferrara 1999).

Direct evidence for supernova heated galactic halos stems from imaging and spectroscopy of diffuse soft X-ray emission. This has been impressively demonstrated by XMM-Newton observations of NGC 253 where the nuclear X-ray plume is found to be explained only by star formation without the contribution of an active galactic nucleus (Pietsch et al. 2001). Moreover, it clearly shows that the galactic starburst must drive a thermal outflow, since there are strong indications of collisionally excited oxygen and iron L line complexes in the spectrum (Breitschwerdt 2003).

In a pioneering work Ipavich (1975) pointed out the importance of CRs for the generation of a galactic wind. This is motivated by the observation that CRs and the magnetic field each contribute the same amount of pressure and energy to the ISM as the hot gas (Beck et al. 1996). This contribution might be enough to sustain a galactic wind with the pressure generated by the CRs, because the CR nucleons, which contain the bulk of the energy, do not suffer from strong radiative losses like the hot gas. The CR driven galactic wind is hence another scenario which needs consideration when discussing gaseous halos.

The theoretical framework for the CR transport is given by the combined diffusion convection equation which can be applied in the local comoving coordinate system, if the bulk speed of the background medium is non-relativistic. This is motivated by observing the isotropic pitch angle distribution relative to the

local plasma which is a consequence of the fast scattering of CR particles by the low-frequency magnetohydrodynamic turbulence as, for example, Alfvén waves and fast magnetosonic waves (Schlickeiser 2002). Breitschwerdt et al. (1991, 1993) applied the transport equation for different magnetic field configurations in the Milky Way. They concluded that the CR transport can be split in an *entirely diffusive* and an *entirely convective* regime, dependent only on the local magnetic field configuration. For the lower Milky Way halo they assumed the magnetic field lines to be turbulently excited by stochastic gas motions caused by expanding and overlapping SNRs. Thus there will be no preferred direction of propagation of these magnetic fluctuations and hence no net Alfvénic drift. In the halo the magnetic field lines of the superbubbles begin to overlap and form “open” field lines which might be enhanced by magnetic reconnection (Parker 1992).

From these observations it is clear that there is a need for understanding the three-dimensional structure of the magnetic field in the halo of spiral galaxies. That restricts the observations to a few nearby edge-on galaxies which allow the study of the extra-planar magnetic field with high spatial resolution and sensitivity. A small sample of such galaxies has been presented in Dettmar & Soida (2006) (see also Dumke & Krause 1998; Krause 2004); one sample member was the nearby starburst galaxy NGC 253 which contains one of the brightest radio halos discovered so far.

This paper is the successive paper of Heesen et al. (2007) (Paper I thereafter) where the cosmic ray distribution was found to be consistent with a vertical CR transport from the disk into the halo. In contradiction to this finding there was so far no poloidal magnetic field discovered in the halo of NGC 253. The most detailed discussion of the magnetic field structure in NGC 253 has been presented by Beck et al. (1994), where a mainly disk-parallel magnetic field was found in the disk and halo. This was explained by a strong shearing of the magnetic field due to differential rotation. The study presented in this paper will provide new sensitive observations of the large-scale magnetic field in the halo of NGC 253. We used the polarimetry information of the observations presented in Paper I at different wavelengths which allowed us to apply a correction for the Faraday rotation and thus to determine the intrinsic magnetic field orientation.

This paper is organized as follows: we start with the description of the observations and explain especially the calibration of the polarization in order to cope with the instrumental polarization caused by the high dynamic range (Sect. 2). Then we will present the continuum maps of NGC 253 along with the vectors of the intrinsic magnetic field and briefly describe its morphology (Sect. 3). In Sect. 4 we will investigate the magnetic field structure and present a model for the large-scale magnetic field. In Sect. 5 we will discuss the consequences of our findings for the radio halo of NGC 253 and the observed other phases of the ISM. Finally we summarize our results and present the conclusions in Sect. 6.

2. Observations and data reduction

2.1. Effelsberg observations

In Paper I we have described our radio continuum observations of NGC 253 with the 100-m Effelsberg telescope¹. The high dynamic range ($\gtrsim 1000$) due to the strong nuclear point-like source

(hereafter for simplicity called the nucleus) requires several additional steps in the data reduction. In Paper I we explained how we removed the sidelobes of the nucleus via a Högbom cleaning of the total power maps. But the high dynamic range has also an impact on the polarization via the leakage from the total power emission to the polarized intensity. This so-called *instrumental polarization* is at a level of few % for the Effelsberg telescope with respect to the total power intensity. Thus, it can be neglected only for observations with a dynamic range significantly less than 100 which is not fulfilled for our observations.

In order to apply a correction for the instrumental polarization we used beam patterns for Stokes Q and U obtained from deep observations of the unpolarized point-like source 3C84. The cleaned total power emission was convolved with the beam patterns and the computed instrumental contribution was subtracted from the Stokes Q and U maps, respectively. Finally we obtained the map of the polarized intensity from the corrected Stokes Q and U maps using COMB of the Astronomical Image Processing Package² (AIPS). We applied a correction for the noise bias in order to preserve the mean zero level of the polarized intensity. The noise level of the final maps are $200 \mu\text{Jy}/\text{beam}$ for $\lambda 6.2 \text{ cm}$ at a resolution of $144''$ Half Power Beam Width (HPBW) and $100 \mu\text{Jy}/\text{beam}$ for $\lambda 3.6 \text{ cm}$ at a resolution of $84''$ (HPBW) in polarized intensity, respectively.

2.2. VLA observations

With the VLA³ observations we covered NGC 253 with a mosaic consisting of 15 pointings in order to be sensitive also to the extra-planar emission (for details see Paper I). Thus we met the challenge of obtaining the polarization maps when the nucleus is located at the edge of the primary beam in some of our pointings. In the center of the primary beam the instrumental polarization is less than 0.1 % but at the edge of the primary beam it rises to more than 1 %. The variability in time, when the nucleus moves on a circle in the primary beam around the center since the VLA antennas have an alt-azimuthal mount, complicates the situation even further. This prevents the removing of sidelobes with the Högbom clean algorithm as it works only for non-variable sources. Thus the standard polarization calibration technique leads to a polarization map which is completely dominated by instrumental polarization (Heesen 2007).

Hence, we developed a specially tailored technique for the pointings with the nucleus located at the edge of the primary beam. The polarization calibration PCAL (part of AIPS) was applied on the nucleus itself instead on the secondary (phase) calibrator in order to find a solution for the off-axis instrumental polarization. The appropriate beam patterns in Stokes Q and U allowed us to subtract the nucleus from the (u,v)-data of individual “snapshots”, which contained less than 10 minutes of observing time. This effectively removes the time variable contribution of the instrumental polarization caused by the nucleus. Thus we were able to use the full set of (u,v)-data in order to get the best (u,v)-coverage which resulted in the expected sensitivity of the extended emission.

The other pointings not influenced by the nucleus were calibrated with the secondary calibrator using PCAL. Inverting the (u,v)-data with natural weighting (i.e. Briggs Robust=8) we produced maps of all pointings in Stokes Q and U which were convolved with a Gaussian to $30''$ (HPBW). The combination of the

² AIPS is distributed by the NRAO as free software.

³ The VLA (Very Large Array) is operated by the NRAO (National Radio Astronomy Observatory).

¹ The Effelsberg 100-m telescope is operated by the Max-Planck Institut für Radioastronomie (MPIfR).

pointings was done with LTESS (part of AIPS) which performs a linear superposition with a correction for the VLA primary beam attenuation using information from each pointing out to the 7 % level of the primary beam (Braun 1988). The final maps are essentially noise limited with a sensitivity of $30 \mu\text{Jy}/\text{beam}$ at a resolution of $30''$ (HPBW) in Stokes Q and U , respectively. We used IMERG (part of AIPS) for the combination of the VLA and Effelsberg Stokes Q and U maps in order to fill up the missing zero-spacing flux. The map of the polarized intensity has been computed using again POLC with a correction for the noise bias.

3. Morphology of the polarized emission

In this section we briefly discuss the morphology of the polarized emission and the magnetic field orientation. The polarization vectors (E-vectors) have been rotated by 90° in order to display the orientation of the magnetic field vectors (B-vectors). A correction for the Faraday rotation has been applied and thus the orientation of the intrinsic magnetic field is presented (see Sect. 4.3 for details). The contour plots were overlaid onto an optical image obtained from the DSS (Digital Sky Survey)⁴.

First we present the B-vectors together with the total power emission contours. In Fig. 1 we present the $\lambda 6.2$ cm combined VLA + Effelsberg map with a resolution of $30''$ (HPBW). The length of the vectors is proportional to the polarized intensity where we have clipped the vectors – in this figure and in all other figures presented in this paper – below a two-sigma level in polarized intensity. The high resolution allows a comparison between the optical image and the magnetic field orientation. The spiral arms and the magnetic field are well aligned. Hence, we can presume that the magnetic field follows the spiral arms. This presumption will be tested with calculation of the Rotation Measure (RM) in Sect. 4.3. The magnetic field orientation is in general disk-parallel. However, we find at some locations a stronger vertical component, where the magnetic field orientation is almost perpendicular to the orientation of the major axis. This is especially the case for the large “radio spur” southeast of the nucleus where the magnetic field gradually opens from a disk-parallel field to a perpendicular field. A second less prominent radio spur is found west of the nucleus, where the magnetic field orientation is roughly inclined by 45° with respect to the major axis. Its western tip is found at the point-source with the position (Ra: $00^{\text{h}}47^{\text{m}}12^{\text{s}}.09$, Dec: $-25^\circ17'45''$.0). At the notable extension of total power emission northwest of the nucleus the magnetic field orientation is moderately inclined with respect to the major axis. In general we find the magnetic field orientation to be disk-parallel only along the midplane of the galaxy with an increasing vertical component further away from the midplane. The pattern of the magnetic field orientation is similar to an “X”-shaped pattern centered on the nucleus. Such magnetic field configurations have been found in other edge-on spiral galaxies, too (see Soida 2005; Krause et al. 2006; Krause 2007).

The magnetic field orientation together with the total power contours obtained from the $\lambda 6.2$ cm Effelsberg observations alone is presented in Fig. 2. The low resolution of $144''$ (HPBW) smears out the fine structure but comparing with the high-resolution merged VLA + Effelsberg map we find a good agreement of the magnetic field orientation. This partially stems from

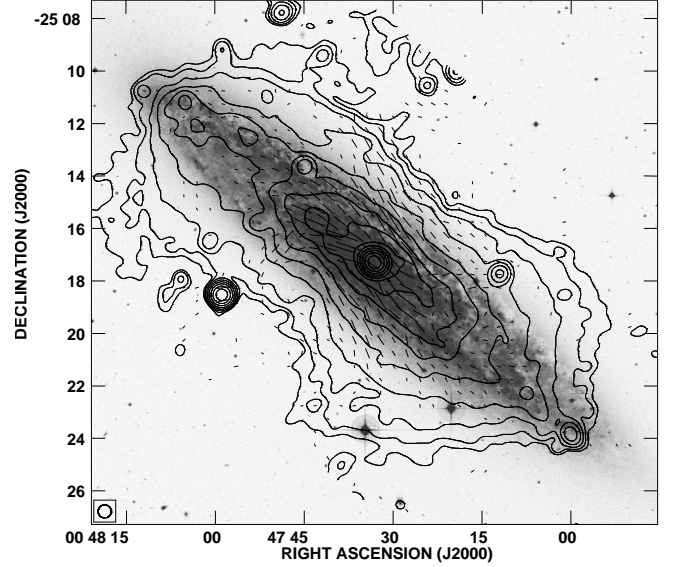


Fig. 1. Total power radio continuum obtained from the combined VLA + Effelsberg observations at $\lambda 6.2$ cm. The overlaid vectors indicate the orientation of the intrinsic regular magnetic field. The length of the vectors is defined by $1''$ to be equivalent to $12.5 \mu\text{Jy}/\text{beam}$ of polarized intensity. Contours are at 3, 6, 12, 24, 48, 96, 192, 384, 768, 1536, 3077, 6144, 12288, and $24576 \times 30 \mu\text{Jy}/\text{beam}$.

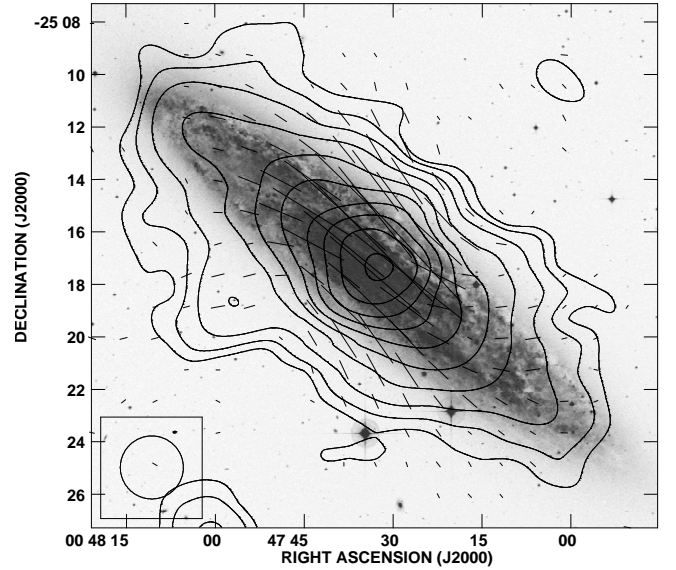


Fig. 2. Total power radio continuum obtained from the Effelsberg observations at $\lambda 6.2$ cm. Contours are at 3, 6, 12, 24, 48, 96, 192, 384, 768, and $1536 \times 1 \text{ mJy}/\text{beam}$. The overlaid vectors indicate the orientation of the intrinsic regular magnetic field. The length of the vectors is defined by $1''$ to be equivalent to $50 \mu\text{Jy}/\text{beam}$ of polarized intensity.

the fact that the Effelsberg map introduces the large-scale of the extended emission via filling up the missing zero-spacing flux. We find in general the magnetic field orientation more disk-parallel, for instance at the location of the large radio spur, in comparison to Fig. 1. Also we see the second radio spur west of the nucleus. The magnetic field orientation on the large-scales reminds again of an “X”-shaped pattern centered on the nucleus.

The $\lambda 3.6$ cm map presented in Fig. 3 shows a similar magnetic field orientation with a resolution of $84''$ (HPBW). Only in

⁴ The compressed files of the “Palomar Observatory - Space Telescope Science Institute Digital Sky Survey” of the northern sky, based on scans of the Second Palomar Sky Survey are ©1993-1995 by the California Institute of Technology and are distributed herein by agreement.

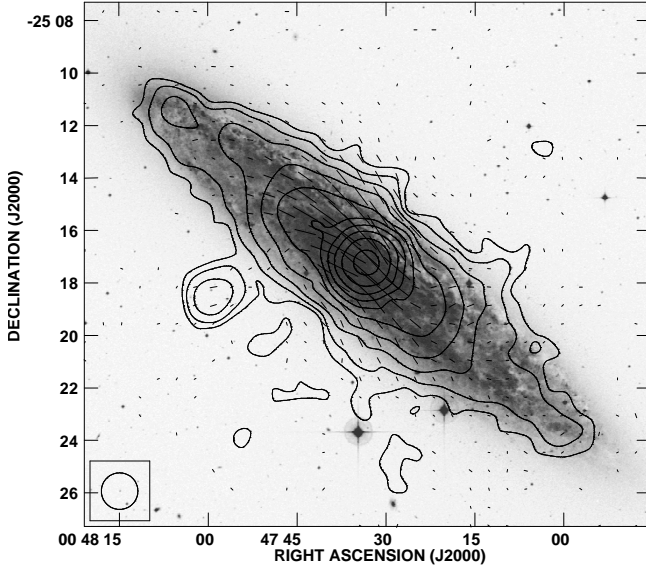


Fig. 3. Total power radio continuum obtained from the Effelsberg observations at $\lambda 13.6$ cm. Contours are at 3, 6, 12, 24, 48, 96, 192, 384, 768, and $1536 \times 500 \mu\text{Jy/beam}$. The overlaid vectors indicate the orientation of the intrinsic regular magnetic field. The length of the vectors is defined by $1''$ to be equivalent to $50 \mu\text{Jy/beam}$ of polarized intensity.

the center we find a disk-parallel magnetic field whereas away from the center at larger galactocentric radii and away from the midplane the field lines start to open with the large radio spur southeast of the nucleus sticking out as finger from the disk with the B-vectors aligned perpendicular to the disk. The noise level of the polarized intensity is $100 \mu\text{Jy/beam}$ compared to $500 \mu\text{Jy/beam}$ in total power which explains why many vectors are plotted outside the total power contours.

In the next plots we highlight the actual distribution of polarized intensity in contour plots overlaid on the intrinsic magnetic field orientation. The polarized intensity obtained from the combined VLA + Effelsberg observations at $\lambda 16.2$ cm is presented in Fig. 4. The polarized emission is unlike to the total power emission as it reveals almost no disk-like structure. Indeed it is hard to guess at all where the disk is located without having the optical image. This is partially caused by an asymmetry of the disk which is more point- than mirror- symmetric. In fact the emission reminds of an “S”-shaped structure which follows roughly the spiral arms. The bulk of the emission forms a huge box including the inner part of the disk whereas in the outer parts of the disk the polarized emission is weak at this small beam size. The impression of the box is increased by the large extension of polarized emission perpendicular to the disk. Hence, the detection of extra-planar polarized emission is confirmed. Compared to the total power distribution we find the polarized emission extending to larger vertical heights above the inner disk than the total power emission. We find the contour lines between the large radio spur and the southeastern extension to show a notch that is caused by a low level of polarized intensity there. We will refer these regions to as *depolarization regions*. The depolarization might be caused by the overlapping of two magnetic field components where one component is disk-parallel and the other component has an orientation perpendicular to the disk. The disk-parallel magnetic field with radial and azimuthal (r, ϕ) components we will refer to as the *toroidal* magnetic field. The vertical magnetic field with radial, azimuthal, and vertical (r, ϕ, z) we will refer to as the *poloidal* magnetic field. We will investi-

gate this model for the magnetic field structure in more detail in Sect. 4.

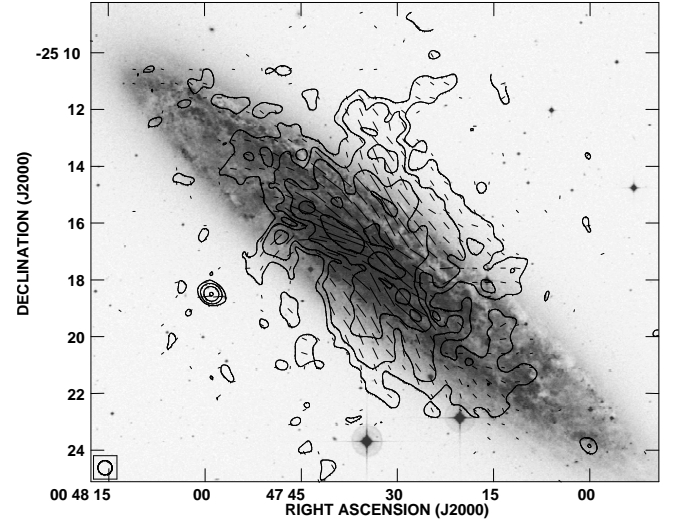


Fig. 4. Polarized intensity obtained from the combined VLA + Effelsberg observations at $\lambda 16.2$ cm. Contours are at 3, 6, 12, and $24 \times 30 \mu\text{Jy/beam}$. The overlaid vectors indicate the orientation of the intrinsic regular magnetic field. The length of the vectors is defined by $1''$ to be equivalent to $12.5 \mu\text{Jy/beam}$ polarized intensity.

This general description is approved also for the $\lambda 16.2$ cm Effelsberg polarized intensity map presented in Fig. 5 where the low resolution of $144''$ highlights the large-scale distribution of the polarized emission. We find the two radio spurs well visible, where the small radio spur west of the nucleus is even better visible than in the combined VLA + Effelsberg high resolution map. Also we find the two previously mentioned depolarization regions associated with the radio spurs. The eastern one is visible as a notch in the contour lines almost extending to the nucleus. The western one is visible as a dip in the polarized intensity near the northern edge of the optical disk. Due to the large beam size this map is more sensitive to weak emission and we find the emission distributed over almost the entire length along the major axis of the disk. Also the extra-planar polarized emission is detected at even higher distances from the disk than in the combined VLA + Effelsberg map.

With the Effelsberg $\lambda 13.6$ cm map of the polarized intensity presented in Fig. 6 we can check these assumptions for a shorter wavelength. We find the magnetic field orientation again aligned with the major axis of the galaxy only at small galactocentric radii. The emission shows an “S”-shape with the largest extension perpendicular to the disk at the position of the spiral arms. The two depolarization regions are also found associated with the two radio spurs. Further, the emission is slightly more concentrated to the disk than at $\lambda 16.2$ cm which can be related to the smaller scaleheight of the total power emission that influences also the polarized emission. Again we find the magnetic field vectors of the large radio spur southeast of the nucleus already well in the disk bending up from a disk-parallel to an orientation which is perpendicular to the disk. The $\lambda 13.6$ cm polarization map was important in order to determine the *RM* distribution from the rotation of the B-vectors by Faraday rotation as it is discussed in Sect. 4.3.

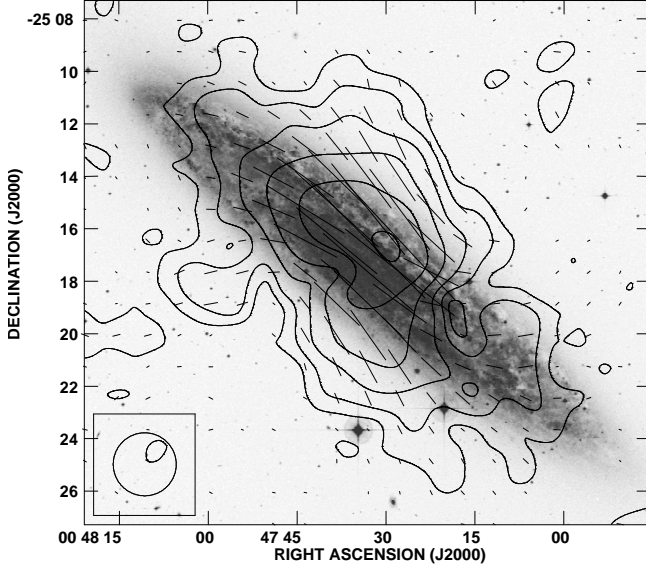


Fig. 5. Polarized intensity obtained from the Effelsberg observations at $\lambda 6.2$ cm. Contours are at 3, 6, 12, 24, 48, and 96 times $200 \mu\text{Jy}/\text{beam}$. The overlaid vectors indicate the orientation of the intrinsic regular magnetic field. The length of the vectors is defined by $1''$ to be equivalent to $50 \mu\text{Jy}/\text{beam}$ of polarized intensity.

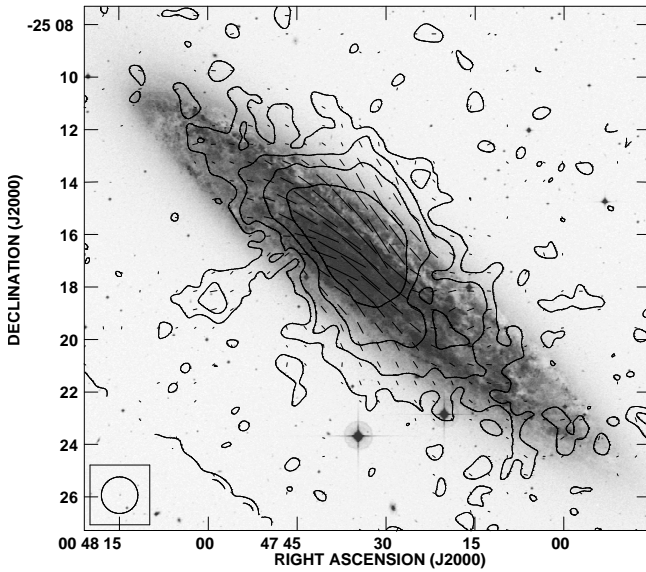


Fig. 6. Polarized intensity obtained from the Effelsberg observations at $\lambda 3.6$ cm. Contours are at 3, 6, 12, and $24 \times 100 \mu\text{Jy}/\text{beam}$. The overlaid vectors indicate the orientation of the intrinsic regular magnetic field. The length of the vectors is defined by $1''$ to be equivalent to $50 \mu\text{Jy}/\text{beam}$ of polarized intensity.

4. The magnetic field structure

4.1. Total polarized flux

The linear polarization is caused by cosmic ray electrons (CREs) spiraling in a magnetic field and emitting linear polarized synchrotron radiation. The turbulent magnetic field gives no linear polarized signal as the field direction is randomly distributed and so is the polarization direction. Thus, the synchrotron emission is totally unpolarized. Even when the magnetic field would consist only of a regular magnetic field component one would measure

only up to 70 % of fractional polarization which is defined as the ratio of the polarized intensity to the total power intensity and also referred to as the degree of polarization. The observed total power emission has also some fraction of thermal contribution which comes from the free-free radiation which is not polarized. Hence, the assumption is used that the polarization degree is a measure for the fraction of the regular magnetic field with respect to the turbulent magnetic field.

The total integrated polarized fluxes have been obtained by integration in ellipses which includes the extra-planar emission as described in Paper I. In Tab. 1 the total polarized fluxes measured at different frequencies and different instruments are listed. The polarization degree has been computed by taking only the extended total power emission into account which means that the flux of the nucleus has been subtracted. We find a fractional polarization of 5 % to 10 % which is similar to values found in other galaxies.

Table 1. Total integrated polarized flux S_{pi} and the degree of polarization P .

| λ [cm] | Instrument | S_{pi} [Jy] | P [%] |
|----------------|------------------------|----------------------|---------|
| 6.2 | VLA + Effelsberg | 0.0796 ± 0.002 | 5.5 |
| 6.2 | VLA | 0.0635 ± 0.002 | 5.5 |
| 6.2 | Effelsberg (uncleaned) | 0.0874 ± 0.0006 | 4.8 |
| 6.2 | Effelsberg (cleaned) | 0.0869 ± 0.0006 | 6.1 |
| 3.6 | Effelsberg (uncleaned) | 0.0624 ± 0.0007 | 8.3 |
| 3.6 | Effelsberg (cleaned) | 0.0583 ± 0.0007 | 8.6 |

The degree of polarization is calculated with respect to the extended total power flux (see Paper I).

4.2. Distribution of the fractional polarization

More insight into the actual magnetic field structure is obtained by studying the distribution of the polarization degree. Dividing the map of the polarized intensity by the total power intensity we created maps of the polarization degree. In Fig. 7 we present the map of the polarization degree for the $\lambda 6.2$ cm combined VLA + Effelsberg observations with a resolution of $30''$ (HPBW). The fractional polarization has a minimum along a line connecting the two depolarization regions which is roughly aligned in an east-west direction. Otherwise the polarization degree shows a general trend of rising values from the disk into the halo i.e. with increasing distance from the major axis. Thus we find in the box-shaped polarization distribution (as described in Sect. 3) the highest polarization degrees toward the northern and southern edge, respectively. The polarization degree has an absolute maximum at the large extension northeast of the nucleus with more than 30 %.

The map of the fractional polarization for the $\lambda 6.2$ cm Effelsberg observations is presented in Fig. 8. With a resolution of $144''$ (HPBW) we see preferentially the large-scale distribution of the polarization degree. This distribution is consistent with the high resolution map discussed in the previous paragraph. At the position of the nucleus we find a local minimum of the polarization degree just because the nucleus is virtually unpolarized with a polarization degree less than 0.1 %. We note that the polarization degree is not exceptional high at the location of the large radio spur southeast of the nucleus.

We now compare these results with the distribution of the polarization degree obtained from the $\lambda 3.6$ cm Effelsberg observations which is presented in Fig. 9 with a resolution of $84''$

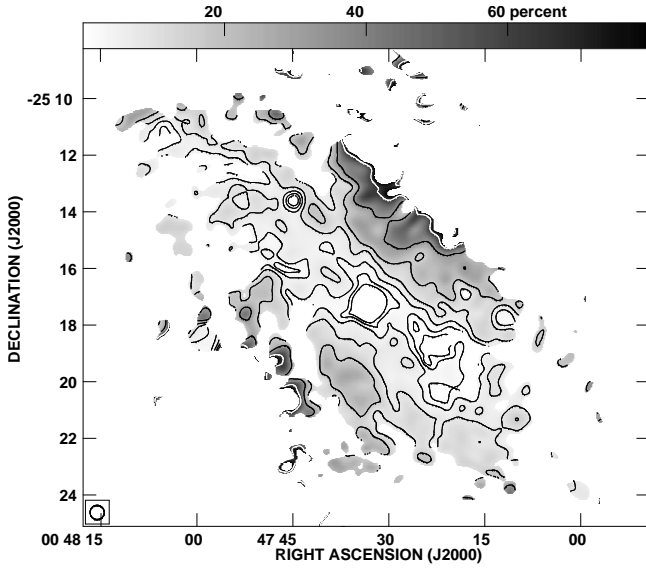


Fig. 7. Distribution of the polarization degree obtained from the combined VLA + Effelsberg observations at $\lambda 6.2$ cm. Contours are at 1, 2, 4, 8, 16, 32, and $64 \times 1\%$. The grey scale is coded with the polarization degree as shown in the wedge at the top.

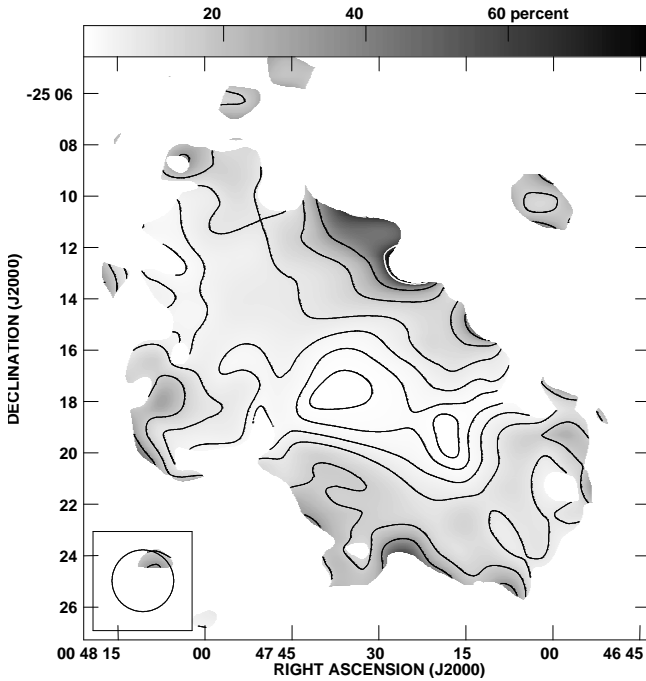


Fig. 8. Distribution of the polarization degree obtained from the Effelsberg observations at $\lambda 6.2$ cm. Otherwise same as Fig. 7.

(HPBW). The two depolarization regions located at the base of the radio spurs are connected by a line with the nucleus the middle as a local minimum. The highest degree of polarization is again found at the large extension northeast of the nucleus. The polarization degree rises with increasing distance from the mid-plane. The morphological analysis of the distribution of the polarized emission and the fractional polarization suggests the decomposition of the large-scale magnetic field into the toroidal and the poloidal magnetic field component. This will be investigated in the following sections.

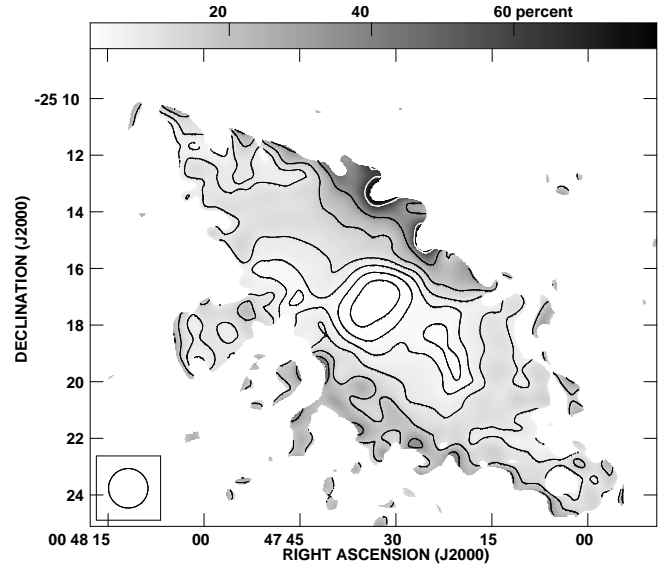


Fig. 9. Distribution of the polarization degree obtained from the Effelsberg observations at $\lambda 3.6$ cm. Otherwise same as Fig. 7.

4.3. Distribution of the Rotation Measure

The polarization angle of the magnetic field vectors is changed by the Faraday rotation for which the amount of rotation strongly depends on the wavelength. The measure for the Faraday rotation is the RM which is defined by

$$\Delta\psi = RM \cdot \lambda^2, \quad (1)$$

where $\Delta\psi$ is the rotation of the polarization vector and λ is the observing wavelength. The RM can be expressed as a path integral over the line-of-sight component B_{\parallel} of the large-scale magnetic field and the density of thermal electrons n_e from the source of polarized emission to the observer:

$$RM = \int n_e B_{\parallel} ds. \quad (2)$$

The RM distribution can be computed using Eq. 1 from the difference $\Delta\psi$ of the orientation angle of the B-vectors between two maps at different wavelengths. In Fig. 10 we present the distribution of the RM between $\lambda 6.2$ cm and $\lambda 3.6$ cm obtained from the Effelsberg observations only. The resolution is thus limited by the $\lambda 6.2$ cm Effelsberg beam of $144''$ (HPBW) and allows the study of the large-scale RM distribution. The large-scale RM distribution shows a gradual change of positive RM s in the northeastern part of the disk and halo to negative RM s in the southwestern part. Of course there are some local deviations, one of them is a region southwest of the nucleus with strong negative RM ($< -200 \text{ rad m}^{-2}$) associated with a depolarization region.

The large-scale magnetic field has thus in the northeastern part a direction pointing to the observer and in the southwestern part a direction pointing away from the observer. Together with the observed intrinsic B-vectors (Sect. 3) this agrees well with the large-scale toroidal field in the disk of NGC 253 as expected by the mean-field $\alpha\Omega$ dynamo. This is the first mode (S0) in an axisymmetric (ASS) field that spirals in a uniform direction (Baryshnikova et al. 1987). Comparing these results with rotation curves from spectroscopic H α and H I observations by (Pence 1981) and Puche et al. (1991), respectively, we find an opposite direction of the velocity field in the galaxy disk. The northeastern part contains a receding radial velocity and the

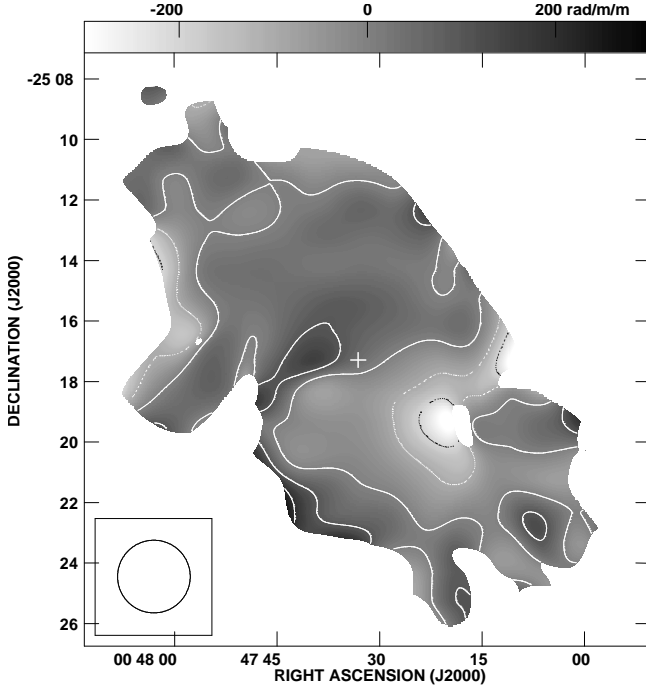


Fig. 10. *RM* distribution between $\lambda 6.2$ cm and $\lambda 3.6$ cm obtained from Effelsberg observations. Contours are at -200 , -100 , 0 , 100 , and $200 \times 1 \text{ rad m}^{-2}$. The position of the nucleus is marked by a cross.

southwestern part a preceding radial velocity. The analysis of Krause & Beck (1998) showed that for such a case we find a spiral magnetic field with the direction of the field lines pointing inwards.

The *RM* was also computed for the highest resolution using the combined VLA + Effelsberg $\lambda 6.2$ cm and the Effelsberg $\lambda 3.6$ cm maps. For this the high resolution combined VLA + Effelsberg map has been convolved with a Gaussian to $84''$ HPBW, the resolution of the Effelsberg map. The vector maps at both wavelengths have been clipped below a 4σ -level in polarized intensity prior to the combination. In Fig. 11 we present the corresponding distribution of the *RM* with a resolution of $84''$ (HPBW). We find the same trend for the sign of the *RM* as described above: the northeastern part contains positive *RM*s and the southwestern part contains negative *RM*s. Thus the finding of an inwards pointed spiral magnetic field is confirmed. With the higher resolution (though still coarse as limited by the $\lambda 3.6$ cm Effelsberg observations) we can find some more details. The base of the large radio spur has a higher *RM*. In contrast the point-like source, which is located at the southern tip of the radio spur, has a significantly smaller *RM*. Here, we should note that the point-like source is dominating the polarized emission there, which can be clearly seen in the contour plots of the polarized emission in Figs. 4 and 6. This makes it likely that it is a background source with an internal *RM* because otherwise the *RM* rises gradually following the spur from the disk into the halo. Another feature that is the region with strong negative *RM*s ($< -200 \text{ rad m}^{-2}$) at the western depolarization region which itself contains a small region with strong positive *RM*s ($> 200 \text{ rad m}^{-2}$).

The observed *RM* distribution was also used in order to create maps of the intrinsic magnetic field orientation. Using Eq. 1 the rotation $\Delta\psi$ of the polarization vector can be computed for each position. This rotation angle was subtracted from the po-

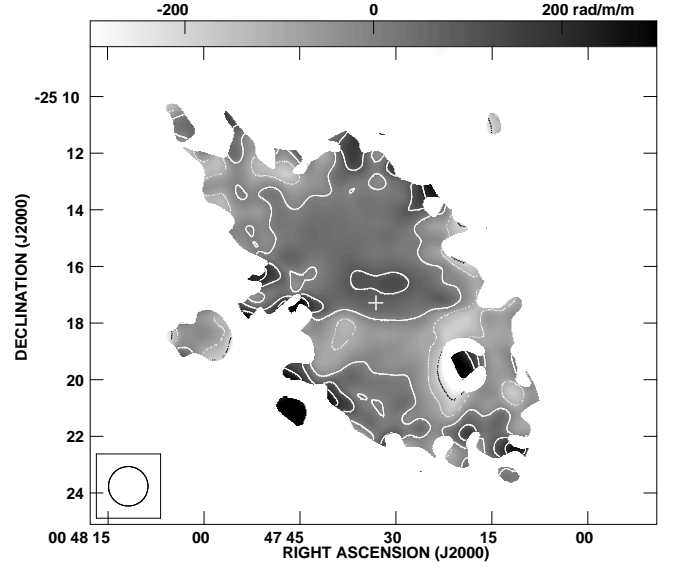


Fig. 11. *RM* distribution between $\lambda 6.2$ cm (VLA + Effelsberg) and $\lambda 3.6$ cm (Effelsberg). Contours are at -200 , -100 , 0 , 100 , and $200 \times 1 \text{ rad m}^{-2}$. The position of the nucleus is marked by a cross.

larization angle in order to get the unrotated polarization angle of the intrinsic magnetic field. The same procedure was applied for the high resolution maps with $30''$ (HPBW) too, though we do not have a *RM* map with sufficient resolution. However, using the combined VLA + Effelsberg map allows us to apply a correction for the Faraday rotation for scales larger than $84''$. For the correction of the $\lambda 6.2$ cm Effelsberg map we used the *RM* map obtained from the Effelsberg observations with $144''$ (HPBW) and for the $\lambda 3.6$ cm Effelsberg map we could use the combined VLA + Effelsberg *RM* map without any loss of resolution for the Faraday correction.

The effect of the Faraday correction is especially important at the base of the large radio spur. The outward bending of the magnetic field vectors is much more gradually after applying the Faraday correction. In general the Faraday correction made the magnetic field orientation more disk-parallel and thus reduced the inclination of the vectors with respect to the major axis.

4.4. The toroidal magnetic field in the disk

A detailed analysis of the *RM* is possible integrating them in sectors (Krause et al. 1989). The integration is done in the azimuthal angle θ that is defined in the plane of the inclined galaxy disk. It is related to the azimuthal angle ϕ defined in the sky plane by $\cos(\theta) = \cos(\phi) \cdot \sin(i)$, where i is the inclination angle of the disk. Hence we find a sine wave for the *RM* with respect to the internal azimuthal angle θ . The phase shift $\Delta\theta$ with respect to the major axis is the pitch angle of the magnetic spiral. Therefore the maximum and minimum of the *RM* do not fall on the major axis but they occur later or earlier with the azimuthal angle running counter clockwise. Hence, we can parametrize the *RM* using the following ansatz

$$RM = A_0 \cos(\theta - \Delta\theta) + A_1, \quad (3)$$

where A_0 is the amplitude and A_1 takes a possible absolute shift of the zero level into account. Using this description we find for the *RM* a good agreement with the actual measured distribution. In Fig. 12 we present the fit using Eq. 3 applied to the *RM* distribution obtained from the Effelsberg observations between a

radius of $r = 72''$ (1.4 kpc) and $r = 216''$ (4.1 kpc). The maximum is found near $\theta = 0^\circ$ and the minimum near $\theta = 180^\circ$. That confirms the result previously obtained by the morphological description of the RM : the northeastern part of the galaxy contains positive RM s ($-90^\circ \lesssim \theta \lesssim 90^\circ$) whereas the southwestern part of the galaxy contains negative RM s ($90^\circ \lesssim \theta \lesssim 270^\circ$). Using the fit we determine the phase shift of $\Delta\theta = -6^\circ$ with respect to the major axis.

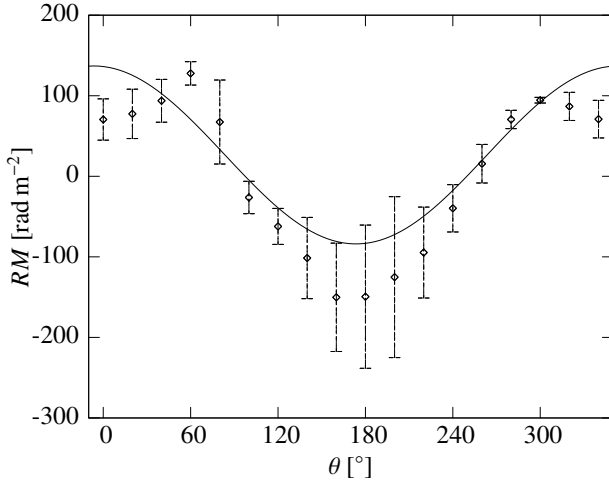


Fig. 12. The integration in sectors of the RM distribution between $\lambda 6.2$ cm and $\lambda 3.6$ cm obtained from the Effelsberg observations.

This value is smaller than the pitch angle of the spiral arms $\beta = 20^\circ$ which has been obtained by Pence (1981) from optical observations. The difference might be explained by the influence of the small bar in the center of NGC 253. Investigations by Krause et al. (1989) showed that the phase shift of the RM must agree with the pitch angle of the optical spiral arms. However, there may be many reasons why this is not the case. One of them, beside the bar, is the contribution of the poloidal magnetic field, which will be discussed in Sect. 4.6.

In Fig. 13 we present the fit for the integration in sectors of the combined VLA + Effelsberg RM distribution between $\lambda 6.2$ cm and $\lambda 3.6$ cm between a radius of $r = 42''$ (0.8 kpc) and $r = 128''$ (2.5 kpc). We find a phase shift of $\Delta\theta = -16^\circ$ which is slightly less than the value obtained from the Effelsberg observations alone.

4.5. Axisymmetric model for the toroidal magnetic field

Using our results presented above we find the magnetic field configuration consisting of a toroidal field which has no component in z -direction perpendicular to the disk and a poloidal field with a component in z -direction. In order to investigate the two components of the regular magnetic field we will first make a model for the toroidal component. Using this model we can make also predictions about the poloidal magnetic field.

With the simplest assumption the toroidal magnetic field can be described by a spiral magnetic field corresponding to an even ASS mode of a galactic dynamo. Our model can be fully described by the Full Width Half Mean (FWHM) of the Gaussian polarization distribution along the major axis, the inclination angle of disk, and the pitch angle ζ of the spiral magnetic field. The inclination angle of 78.5° prescribed we found the model

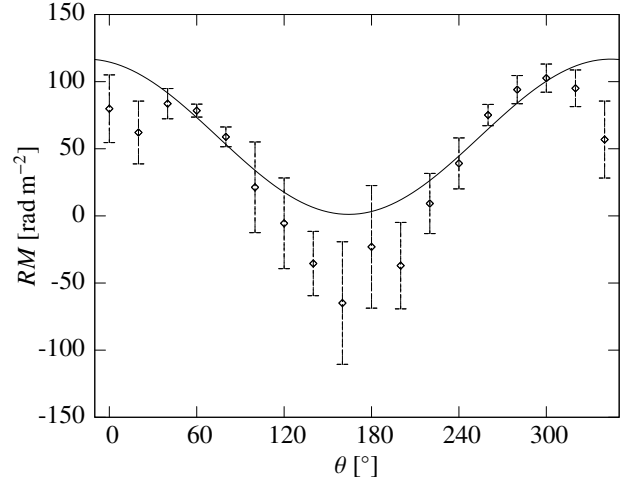


Fig. 13. The integration in sectors of the RM distribution between $\lambda 6.2$ cm and $\lambda 3.6$ cm obtained from the combined VLA + Effelsberg observations.

with $FWHM = 700''$ and $\zeta = 25^\circ$ best resembling the observed polarization distribution. Finally we have convolved the model distribution with a Gaussian to $180''$ HPBW in order to obtain a larger extension perpendicular to the disk. The model distribution was checked with the observed intensity distribution comparing profiles along the major and minor axis. With this procedure we arrived at the model presented in Fig. 14.

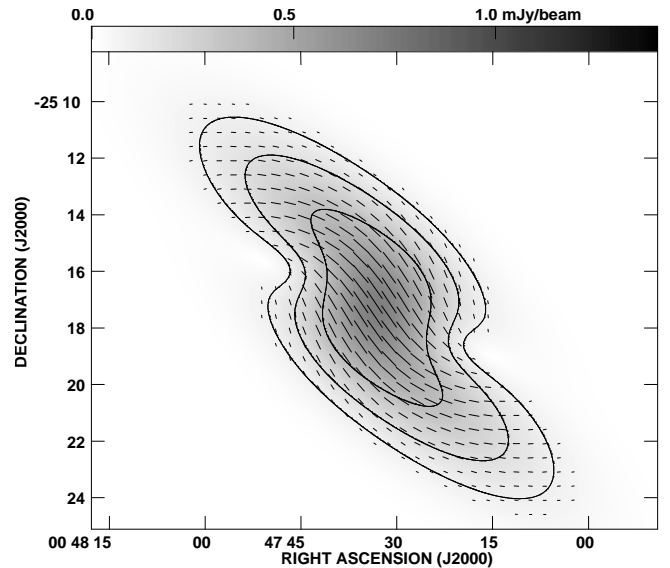


Fig. 14. Axisymmetric model for the toroidal magnetic field with a pitch angle of 25° of the magnetic field spiral. Contours and vectors are identical to Fig. 4. The model explains the depolarization features as a purely geometrical effect caused by the inclination as the disk is not exactly edge-on.

The model of the toroidal magnetic field shows clearly why the map of polarized emission is not symmetric with respect to the minor axis: the maximum and minimum of the polarized intensity are shifted by the pitch angle of the spiral magnetic field. The depolarization regions which are visible as necks in the contour lines can be explained by the model, too. We find the depo-

larization regions to be a purely geometrical effect where the different components of the magnetic field cancel each other. The shift of the depolarization regions with respect to the major axis is also caused by the pitch angle of the magnetic field spiral. The overall shape of the polarized distribution reminds of the “S”-shape observed in the polarization distribution. The amplification of the polarization along the northeastern and southwestern part of the disk can also be attributed to a purely geometrical effect. Moreover, we note the magnetic field orientation to be mainly disk-parallel. Only at the outer edges along the major axis the orientation of the field bends around the edge of the disk as it is expected for a spiral magnetic field.

The depolarization regions however are the only locations where in the inner disk significant deviations from the disk-parallel magnetic field orientation are found. This is reasonable since in the depolarization regions the two components of the magnetic field overlap with no dominating component. Thus, the orientation is not predominantly disk-parallel in the depolarization region. The good coincidence between the model and the observed distribution justifies the choice of the model with its assumptions. Moreover, the model is simple which is a good starting point at the very least.

4.6. The poloidal magnetic field

From this simple model we conclude that the toroidal field is dominating the observed regular magnetic field distribution in the disk. In addition this model allows us to discuss some properties of the magnetic field. First, we note that the two radio spurs are located roughly at the position of the two depolarization regions of the model. Here, the contribution of the toroidal field is much smaller than anywhere else. Hence the question arises whether the poloidal field is hidden elsewhere by the dominating contribution of the toroidal field. Especially in the northeastern and southwestern part where the toroidal field has a maximum due to the favourable aspect angle (near 90°) on the regular magnetic field. In order to study the poloidal magnetic field we subtracted the model magnetic field from the observed magnetic field. We computed the complex polarization angle Π using the expression of Burn (1966) with a path integral

$$\Pi = p_i \frac{\int \epsilon(\mathbf{r}) \cos[\psi(\mathbf{r})] A ds}{\int \epsilon(\mathbf{r}) A ds}, \quad (4)$$

where p_i is the internal polarization vector, $\epsilon(\mathbf{r})$ the local synchrotron emission per unit volume, A the area given by projected beam size at the distance of the source, and $\psi(\mathbf{r})$ the local polarization angle. Our observed quantities, Stokes Q and U , can be retained from the complex polarization angle by the decomposition in the real and imaginary part:

$$Q = \Re(\Pi) \quad U = \Im(\Pi). \quad (5)$$

The observed polarization angle is the superposition of the toroidal and poloidal component and thus $\Pi = \Pi_{\text{tor}} + \Pi_{\text{pol}}$. Using the decomposition in Stokes Q and U of Eq. 5 we find $Q = Q_{\text{tor}} + Q_{\text{pol}}$ and $U = U_{\text{tor}} + U_{\text{pol}}$. Subtracting the maps of Stokes Q_{tor} and U_{tor} from the observed maps of Stokes Q and U leads to maps of Q_{pol} and U_{pol} . From these the polarized intensity and the polarization angle can be computed as explained in Sect. 2. In Fig. 15 we present the polarized emission and the magnetic field orientation of the poloidal magnetic field.

The field configuration of the poloidal magnetic field resembles a “X”-shape with the B-vectors centered on the nucleus. The

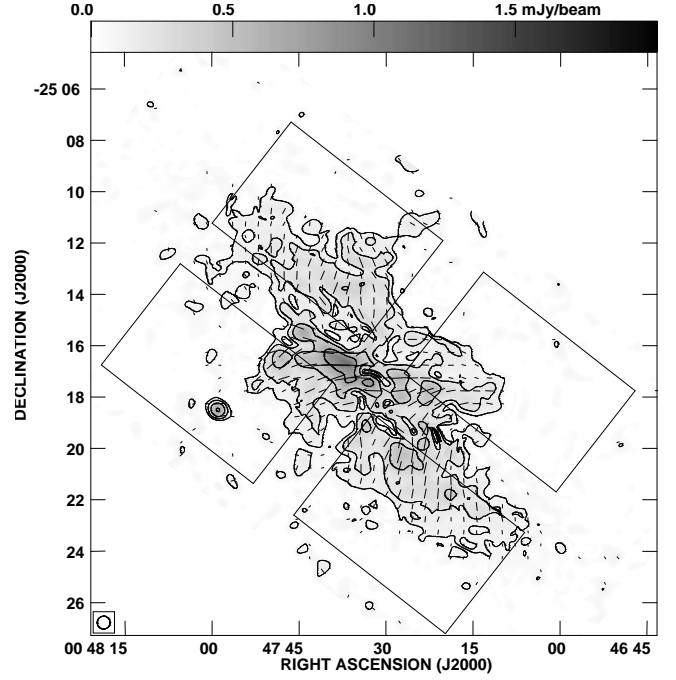


Fig. 15. Polarized intensity and magnetic field orientation of the poloidal magnetic field which was created by subtracting the model of the toroidal magnetic field from the observed magnetic field (for details see text). Contours and vectors are identical to Fig. 4. The boxes for the integration of the orientation angle $\hat{\psi}$ are shown.

field pattern is now almost mirror symmetric to the minor axis. That holds for the polarized emission as well as for the orientation of the magnetic field vectors. We still find that at the large radio spur southeast of the nucleus the B-vectors have the highest inclination angle with respect to the major axis. Otherwise the inclination angle is similar in all quadrants.

In order to quantify our observations of the poloidal magnetic field we have determined a mean orientation angle $\hat{\psi}$ with respect to minor axis. This was done using an integration in four boxes located in the quadrants (see Fig. 15) where we have spared some space between them. We have integrated Stokes Q and U , respectively, and then we calculated the orientation angle of the magnetic field by

$$\hat{\psi} = \arctan\left(\frac{U}{Q}\right) - PA + 90^\circ, \quad (6)$$

where $PA = 52^\circ$ is the position angle of the major axis and 90° has been included in order to use the orientation of the B-vectors instead of the E-vectors. However, as we have defined the orientation angle $0^\circ \leq \hat{\psi} \leq 90^\circ$ we have to add some corrections of 90° , 180° , or 270° depending on the quadrant. We find a mean orientation angle of $\hat{\psi} = 33^\circ$ with respect to the minor axis.

The orientation angle of the magnetic field can be used to make a comparison between the rotational velocity and the outflow speed. Zirakashvili et al. (1996) express the orientation angle α of the magnetic field with respect to the minor axis by

$$\tan \alpha = \frac{\Omega r}{v}, \quad (7)$$

where Ωr is the rotation velocity of the disk and v the outflow velocity perpendicular to the disk. If we use the estimate for the CR bulk speed from Paper I of 270 km s^{-1} and adopt a rotation

speed of 200 km s^{-1} (Pence 1981), we find an orientation angle of $\alpha = 37^\circ$. This is remarkably close to our finding. We should note the case when the outflow speed equals the escape velocity which can be expressed by the rotation speed via $v = \sqrt{2} \cdot \Omega r$. In this case we would expect an orientation angle of $\alpha = 35^\circ$. The conclusion is that the orientation angle of the poloidal magnetic field is near the theoretical expected value with the outflow velocity equal to the escape velocity. The kinetic energy of the CR bulk speed is thus high enough to escape from the gravitational potential. The influence of the cosmic ray driven wind on the formation on the halo is discussed in the next section.

5. Discussion

The contribution of our radio continuum observations to the understanding of the formation of the halo must comprise the results from the total power study presented in Paper I, the polarimetry study presented here, and the observations of other phases of the ISM.

5.1. The CR distribution and the magnetic field structure

The extra-planar distribution of the total power emission does depend only on the CRE synchrotron lifetime. First, we note that the CR bulk speed profiles of Paper I explain the different abundances gas in the halo. In the northeastern halo the CR bulk speed does not decelerate up to a height of 6 kpc. We can not trace the CRs to larger distances from the disk as the CREs have lost their energy after several synchrotron lifetimes and hence are not visible any more. However, as the CR bulk speed is near the escape velocity in the northeastern halo we can speculate that it can reach heights above the disk up to 8 kpc where the largest filaments of soft X-ray emission are found. In the southwestern halo we find the wind speed decreasing and the vertical extent of soft X-ray emission is indeed less than in the northeastern halo.

The transport of CRs was found to be dominated by a convective transport (see Paper I). The turbulent magnetic field of the disk contains the CREs which are scattered in the tangled magnetic field. However, the large-scale magnetic field is frozen into the plasma. The field-lines in the disk are almost following the local velocity vector, i.e. the rotation vector if we neglect the small radial contribution $\sin\beta$. Hence, as the field lines are frozen in the plasma, the local velocity vector must agree with the local B-vector. Using this assumption we find the flow of the hot interstellar medium (HIM) together with the magnetic field consistent with a force-free transport.

5.2. The superwind model

Our findings so far are consistent with a *global* wind over the total extent of the disk of NGC 253. However, this finding must be consistent with the distribution of the extra-planar HIM. From these considerations we expect a correlation of the distribution of the poloidal magnetic field and the hot gas traced by the $\text{H}\alpha$ and soft X-ray emission in the halo of NGC 253. However, at larger galactocentric radii we do not find a significant decrease of the CR bulk speed. This is in contradiction to the observation of the extra-planar HIM concentrated only at small galactocentric radii with sharp transition that creates the impression of lobes.

The distribution of the polarized intensity of the poloidal magnetic field fits the distribution of the extra-planar HIM much better. This presumption can be checked with observations of the extra-planar hot gas by $\text{H}\alpha$ and soft X-ray emission. In Fig. 16

the distribution of the poloidal magnetic field is shown on top of $\text{H}\alpha$ emission obtained from Hoopes et al. (1996) and here convolved with a Gaussian to $20''$ HPBW. There are several $\text{H}\alpha$ plumes extending from the disk into the halo where the most prominent one is located southeast of the nucleus. This nicely coincides with the prominent radio spur. On the prominent extension northeast of the nucleus there is also much extra-planar $\text{H}\alpha$ emission. The map of the soft X-ray emission has been obtained from the ROSAT archive and convolved with a Gaussian to $20''$ in order to highlight the extended emission. In Fig. 17 we see that the extra-planar soft X-ray emission is distributed in prominent lobes which extend up to 8 kpc from the disk. Again the prominent southeastern lobe is associated with the radio spur. The northeastern lobe extends furthest from the disk. The prominent missing emission on the northwest side of the disk can be explained by absorption in the disk and proofs that the southeastern halo on the near side and the northwestern halo is on the far side (Pietsch et al. 2000).

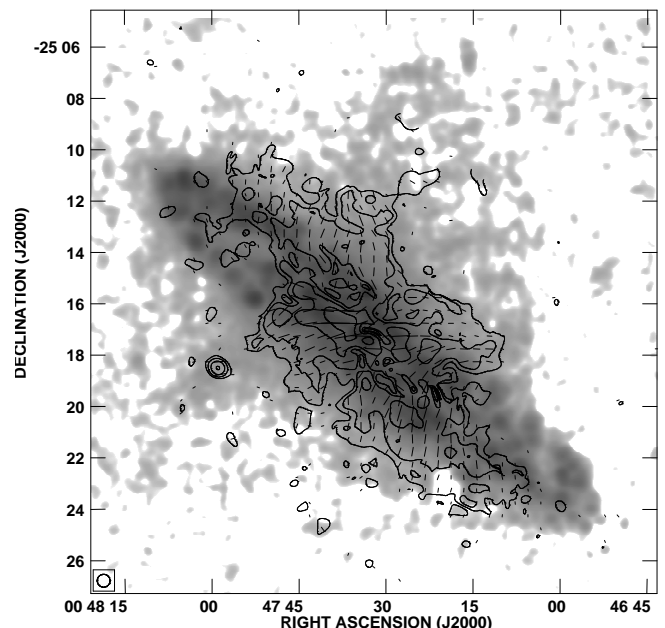


Fig. 16. Distribution and orientation of the poloidal magnetic field with $\text{H}\alpha$ emission. Contours and vectors are identical to Fig. 15.

Thus, we need an explanation why the large-scale magnetic field traces the extra-planar HIM much better than the total magnetic field traced by the total power. Here, we turn to the current understanding of the halo formation of NGC 253. The most attractive scenario is the *superwind* model (Strickland et al. 2002). This model contains a wind that is driven by a small region of active star formation in the center. The lateral pressure compresses the magnetic field. Shock waves convert the kinetic energy into thermal energy. These thermalization regions are concentrated in the lobes seen in the HIM. If the shock waves are small compared to the beam size, the degree of polarization is amplified but the total power emission is not affected. Thus, we can explain the high degree of polarization consistently with the lobes of the HIM. Polarization can hence be an excellent tracer of shock waves.

The global wind of the disk explains the existence of gas in the halo. Outside the lobes of the superwind model there is neutral H I gas (Boomsma et al. 2005). The superwind model

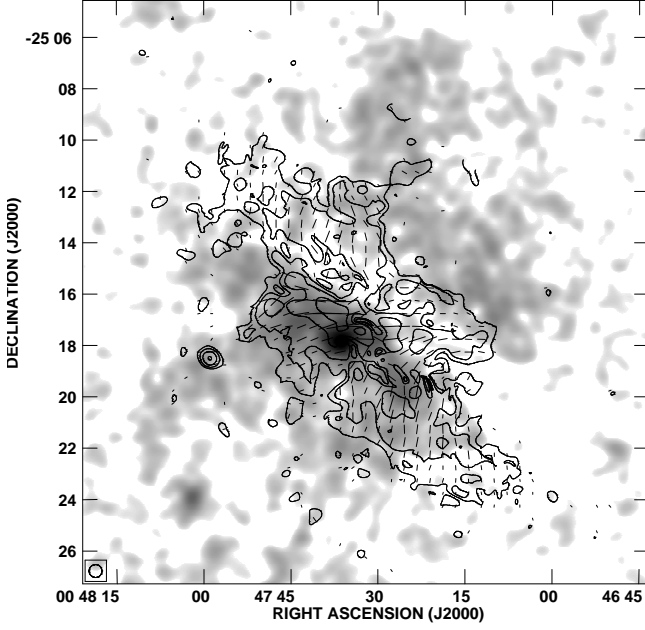


Fig. 17. Distribution and orientation of the poloidal magnetic field with soft X-ray emission. Contours and vectors are identical to Fig. 15.

requires preexisting cold gas in the halo. The abundance of the cold gas in the halo can be explained by the *disk wind* traced by the vertical CR transport.

5.3. Galactic dynamo

The expelling of magnetic field is not only important for the CR propagation but also for the applicability of the *dynamo theory* for the creation of the magnetic field itself. The $\alpha\Omega$ -dynamo relies on the differential rotation of the galactic disk (Ω -effect) and the cyclonic motions of the ionized gas (α -effect). The latter one can be generated by subsequent supernovae explosions (Ferriere 1992). As Kulsrud (1999) has pointed out in his review the amplification of the magnetic field with a galactic dynamo requires the expelling of the magnetic field with the wrong sign. A galactic wind can transport the magnetic field from the disk into the halo and maybe beyond. The investigations of Brandenburg et al. (1993) showed that indeed a galactic wind can under certain circumstances even amplify the galactic dynamo.

6. Summary and conclusions

The three-dimensional magnetic field structure can be best investigated using sensitive radio continuum polarimetry. Our main results are:

1. Only in the inner part of the disk we find a truly disk-parallel magnetic field. The magnetic field is slowly opening with a curvature. The vertical magnetic field component is most prominent at the edge of the inner disk where we find two "radio spurs" especially the large one southeast of the nucleus. The magnetic field configuration can be hence described as "X"-shaped pattern similar to other galaxies.
2. The large-scale magnetic field can be decomposed into the toroidal (r, ϕ) and the poloidal magnetic field (r, ϕ, z) components.
3. The toroidal magnetic field can be described in the innermost part within a galactocentric radius of about 4 kpc by a spiral

magnetic field with a constant pitch angle of $\zeta = 25^\circ$. This leads to a simple axisymmetric model of the spiral magnetic field with a prescribed pitch and inclination angle. The model shows a good resemblance of the observed magnetic field in the disk.

4. The model of the toroidal magnetic field was used to construct a map of the poloidal magnetic field. The distribution of the polarized intensity and the orientation of the poloidal magnetic field shows a distinct "X"-shaped pattern centered on the nucleus.
5. The orientation angle of the poloidal magnetic field is consistent with a transport of the magnetic field which can be described by the superposition of two velocity components: the vertical CR bulk speed and the rotation velocity.
6. The distribution of the poloidal magnetic field coincides in shape with the extra-planar HIM suggested by H α and soft X-ray observations. This can be explained by the compression of the large-scale magnetic field of the expanding superbubble.

Future investigations should include polarimetry at low frequencies. Thus one will obtain the advantage of studying the magnetic structure far from the disk illuminated only by an aged population of CREs. This might be done with the upcoming class of telescopes operating at low frequencies like EVLA, LOFAR, and the SKA.

Acknowledgements. VH would like to thank the organizers of the Graduiertenkolleg GRK 787 and the Sonderforschungsbereich SFB 591 for support and funding during the course of his PhD. The GRK 787 "Galaxy groups as laboratories for baryonic and dark matter" and the SFB 591 "Universal properties of non-equilibrium plasmas" are funded by the Deutsche Forschungsgemeinschaft (DFG).

We thank Dieter Breitschwerdt and Andrew Fletcher for helpful discussions. Moreover, we would like to thank Charles Hoopes for kindly providing us his H α map of NGC 253.

References

- Baryshnikova, I., Shukurov, A., Ruzmaikin, A., & Sokoloff, D. D. 1987, A&A, 177, 27
- Beck, R., Brandenburg, A., Moss, D., Shukurov, A., & Sokoloff, D. 1996, ARA&A, 34, 155
- Beck, R., Carilli, C. L., Holdaway, M. A., & Klein, U. 1994, A&A, 292, 409
- Boomsma, R., Oosterloo, T., Fraternali, F., van der Hulst J.M., & Sancisi, R. 2005, A&A, 431, 65
- Brandenburg, A., Donner, K. J., Moss, D., et al. 1993, A&A, 271, 36
- Braun, R. 1988, Millimeter Array Memo., 46
- Breitschwerdt, D. 2003, in Revista Mexicana de Astronomía y Astrofísica Conference Series, Vol. 15, Revista Mexicana de Astronomía y Astrofísica Conference Series, ed. J. Arthur & W. J. Henney, 311–316
- Breitschwerdt, D., McKenzie, J. F., & Voelk, H. J. 1991, A&A, 245, 79
- Breitschwerdt, D., McKenzie, J. F., & Voelk, H. J. 1993, A&A, 269, 54
- Burn, B. J. 1966, MNRAS, 133, 67
- Dahlem, M., Lisenfeld, U., & Golla, G. 1995, ApJ, 444, 119
- Dahlem, M., Lisenfeld, U., & Rossa, J. 2006, A&A, 457, 121
- Dettmar, R. J. 1992, Fundamentals of Cosmic Physics, 15, 143
- Dettmar, R.-J. & Soida, M. 2006, AN, 327, 495
- Dumke, M. & Krause, M. 1998, in Lecture Notes in Physics, Berlin Springer Verlag, Vol. 506, IAU Colloq. 166: The Local Bubble and Beyond, ed. D. Breitschwerdt, M. J. Freyberg, & J. Truemper, 555–558
- Ferriere, K. 1992, ApJ, 391, 188
- Heesen, V. 2007, PhD thesis, Ruhr-Universität, Bochum, Germany
- Heesen, V., Beck, R., Krause, M., & Dettmar, R.-J. 2007, A&A, in prep.
- Hoopes, C. G., Walterbos, R. A. M., & Greenwalt, B. E. 1996, AJ, 112, 1429
- Ipavich, F. M. 1975, ApJ, 196, 107
- Krause, F. & Beck, R. 1998, A&A, 335, 789
- Krause, M. 2004, in The Magnetized Interstellar Medium, ed. B. Uyaniker, W. Reich, & R. Wielebinski, 173
- Krause, M. 2007, Memorie della Società Astronomica Italiana, 78, 314
- Krause, M., Hummel, E., & Beck, R. 1989, A&A, 217, 4
- Krause, M., Wielebinski, R., & Dumke, M. 2006, A&A, 448, 133

- Kulsrud, R. M. 1999, *ARA&A*, 37, 37
- Mac Low, M.-M. & Ferrara, A. 1999, *ApJ*, 513, 142
- Norman, C. A. & Ikeuchi, S. 1989, *ApJ*, 345, 372
- Parker, E. N. 1992, *ApJ*, 401, 137
- Pence, W. D. 1981, *ApJ*, 247, 473
- Pietsch, W., Roberts, T. P., Sako, M., et al. 2001, *A&A*, 365, L174
- Pietsch, W., Vogler, A., Klein, U., & Zinnecker, H. 2000, *A&A*, 360, 24
- Puche, D., Carignan, C., & van Gorkom, J. H. 1991, *AJ*, 101, 456
- Schlickeiser, R. 2002, *Cosmic ray astrophysics* (Berlin, Germany: Springer)
- Soida, M. 2005, in *The Magnetized Plasma in Galaxy Evolution*, ed. K. T. Chyzy, K. Otmianowska-Mazur, M. Soida, & R.-J. Dettmar, 185–190
- Strickland, D. K., Heckman, T. M., Weaver, K. A., Hoopes, C. G., & Dahlem, M. 2002, *ApJ*, 568, 689
- Zirakashvili, V. N., Breitschwerdt, D., Ptuskin, V. S., & Voelk, H. J. 1996, *A&A*, 311, 113

Chapter 4

Summary and Outlook

4.1 Summary

The evolution, structure, and origin of magnetic fields are still open problems in fundamental physics and astrophysics. Until now, it remains unclear how the evolution of magnetic fields proceeds as galaxies evolve, what properties the possibly magnetized intergalactic medium possesses, and whether the fields in galaxy clusters are primordial or generated locally. The possible connection between structure formation and the magnetic field formation in the early Universe is ultimately to be established by future observations. Nearby galaxies offer the unique opportunity to study how the large-scale magnetic field is generated and sustained by characterizing and comparing their three-dimensional magnetic field structure. The diffuse synchrotron emission and its polarization can be compared with HI, H α , and continuum observations at various wavelengths. It is possible to study in external galaxies how magnetic features interact with other features of the interstellar medium in a much more direct way than in our own Galaxy with its confused lines of sight.

One favoured object to carry out such studies is NGC 253, which not only possesses one of the brightest radio halos discovered so far, but several ISM phases have been detected in its halo, too. The presented study of NGC 253 in radio continuum comprised interferometric and single-dish observations in order to get high resolution combined with the best sensitivity for large-scale emission. The requirements of the high dynamic range due to the strong nuclear point source were met with a specially tailored data reduction for both the single-dish and the interferometric data.

The observations revealed a bright radio halo at all observing wavelengths between $\lambda 90$ cm and $\lambda 3.6$ cm. Due to the brightness of the radio halo and the high sensitivity of the observations, the emission is traced out to an extent of 6 kpc from the disk. However, with 1.7 kpc, the scaleheight of the combined VLA + Effelsberg observations is within the range of other galaxies (Krause 2004). Hence the scaleheight of the cosmic rays and the magnetic field does not depend on the star formation rate (SFR) which is high in NGC 253 ($\text{SFR} \approx 10 \text{ M}_{\odot} \text{ yr}^{-1}$). The local scaleheight does also not depend on the SFR. In the inner regions of the disk, where the SFR is highest, the scaleheights are smallest. The local scaleheight depends, however, almost linearly on the synchrotron lifetime of the cosmic ray electrons (CREs) which in turn depends on the total magnetic field strength. From this behavior I draw two important conclusions as described in Chap. 2: firstly, the CR transport must proceed predominantly in the vertical direction. If the CRs would freely diffuse in the disk and halo, the scaleheight should be uniform along the extent of the disk. The same conclusion has been drawn by Dahlem et al. (1995, 2006), who found a correlation between the radial extent of star formation regions and the synchrotron halo. Secondly, we can define a cosmic ray bulk speed as the ratio of the total power scaleheight to the CRE lifetime. The global CR bulk speed of 270 km s^{-1} is close to the escape velocity of $v_{\text{esc}} = 280 \text{ km s}^{-1}$ which I have estimated

using $v_{\text{esc}} = \sqrt{2} \cdot \Omega r$, where $\Omega r = 200 \text{ km s}^{-1}$ is the rotation velocity of NGC 253 determined by Pence (1981). The kinetic energy of the CR gas is thus almost high enough to drive a wind which escapes from the gravitational potential. Since the emission profiles are not Gaussian but rather strictly exponential, the CR transport is predominantly convective where the CRs and the magnetic field are advected by the *disk wind* blowing from the disk into the halo. While the CREs are transported from their origin in the disk into the halo, they lose their energy by synchrotron radiation which depends quadratically on the CRE energy. The steepening of the spectral index with increasing distance from the disk indicates CR aging and is thus another constraint for dominating radiative losses.

Using the vertical total power emission profiles, I made an investigation of the local CR bulk speed in the disk wind. In the northeastern part of the galaxy, the bulk speed is independent of the galactocentric radius. In contrast, in the southwestern part the bulk speed decreases with increasing galactocentric radius. Observing that the local scaleheight increases with the galactocentric radius, this can be understood by adopting a vertical CR bulk speed profile $v(z)$ for the northeastern and southwestern half, respectively. With this assumption the CR bulk speed is constant with increasing height above the disk in the northeastern part. In the southwestern part, however, the CR bulk speed is decelerating with increasing height above the disk.

The analysis of the three-dimensional magnetic field structure, as described in Chap. 3, further constrains the properties of the disk wind. The polarization vectors of the continuum emission were obtained using polarimetry. The combination of two wavelengths ($\lambda 6.2 \text{ cm}$ and $\lambda 3.6 \text{ cm}$) yielded the distribution of the Rotation Measure (RM) in the magnetized plasma. This was used to correct the Faraday Rotation and to obtain the intrinsic magnetic field orientation. The magnetic field structure was found to possess an “X”-shaped distribution with a disk-parallel field only in the inner part of the disk. The magnetic field lines start to open at larger galactocentric radii and further away from the midplane of the galaxy. This “X”-shaped pattern of the magnetic field vectors has also been found in other edge-on galaxies (Soida 2005; Dettmar & Soida 2006; Krause 2007). The analysis of the RM distribution in sectors, presented in Chap. 3, showed that the magnetic field can be described by an axisymmetric spiral field pointing inwards. Hence, a model was constructed for the *toroidal* (r, ϕ) magnetic field with a prescribed inclination angle of the disk and pitch angle of the magnetic field spiral. The *poloidal* magnetic field (r, ϕ, z) was computed by subtracting the model field from the observations. The poloidal magnetic field distribution resembles a pronounced “X”-shaped distribution centered on the nucleus with a magnetic field orientation angle of 35° with respect to the minor axis. This can be explained if the disk wind advects the toroidal magnetic field together with the disk material and if the orientation of the magnetic field vectors are identical to the vector of the CR bulk speed. The determined orientation angle of the poloidal magnetic field is consistent with the superposition of the vertical outflow velocity – the CR bulk speed – and the rotation velocity of 200 km s^{-1} .

This picture, as presented so far, offers important complementary information to other observed phases of the ISM in the halo of NGC 253. The disk wind creates a thick disk of cold disk material, through which the superwind emerges into the halo (e.g. model 5 of Strickland et al. 2002). The visible lobes in $\text{H}\alpha$ and soft X-ray emission are the layer heated through shocks and turbulent mixing on the contact surface between the hot superwind fluid and the cold disk material. If the swept-up shell cools, an $\text{H}\alpha$ -emitting shell around the superbubble will form. The thick disk component has to be created by material lifted up from the disk through star formation activity (Rosen & Bregman 1995). We can support this model now by measuring the vertical transport of disk material using the CR bulk speed profiles. The decelerating CR bulk speed causes a thick disk with smaller vertical extent in the southwestern part than in the northeastern part of the galaxy. This is confirmed by the finding of less extra-planar HI emission in the southwestern part which led Boomsma et al. (2005) to the speculation that ionization might prevent the detection of HI. The vertical extent of $\text{H}\alpha$ and soft X-ray emission in the southwestern part is also

significantly smaller than in the northeastern part. This corroborates the picture that the cosmic ray transport determines the vertical extent of the thick disk of cool disk gas.

We can further constrain this model by using our polarimetry information. I have shown that the poloidal magnetic field correlates remarkably well with the $H\alpha$ and soft X-ray emission (see Figs. 16 and 17 in Chap. 3). There is clearly an excess of polarized emission that is not seen in total power emission. This can be explained by compression of the swept-up shells of the disk material by the expanding superbubble. The magnetic field orientation is roughly tangential to the shell of the superbubble which shows the pressure gradient to be perpendicular to the shell (for a cartoon of the halo structure see Fig. 4.1). The orientation of the magnetic field could also be explained by the flow of the disk wind as mentioned above, but the amplification of the polarized emission is most likely created by the compression due to the expansion of the superbubble.

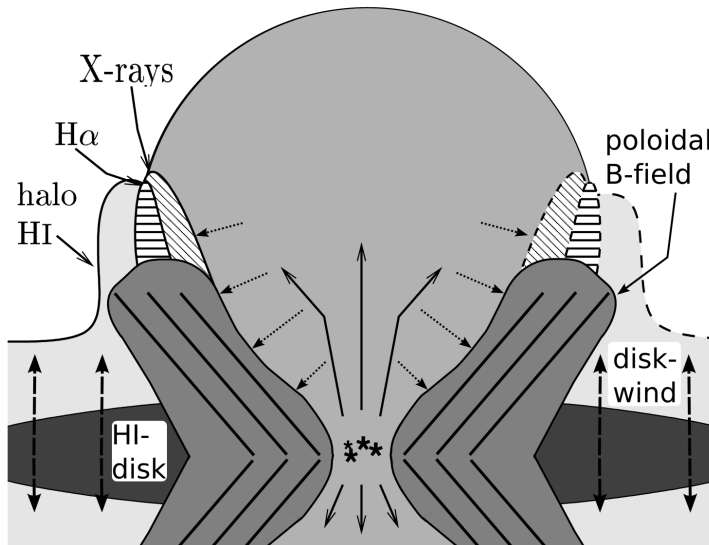


Figure 4.1: Same as Fig. 8 of Boomsma et al. (2005), but with the intensity and the orientation of the poloidal magnetic field added. The disk wind has been indicated, too. The dashed lines on the right show parts that have not been detected.

4.2 Extending the investigations to other spiral galaxies

The discussion of the results of NGC 253 clearly shows that radio continuum observations (including polarimetry) are a powerful tool to study galactic outflows. Thus, it is desirable to study the distribution of cosmic rays and the structure of the large-scale magnetic fields in a larger sample of nearby spiral galaxies. The dependence of the brightness on the radio halo of the star formation in the disk introduces an observational bias towards star forming, gas rich galaxies. NGC 253 is an extreme example with a concentration of high star formation in the central regions. Hence, it is instructive to study galaxies with star formation more uniformly distributed in the disk. Observations of a small sample consisting of three galaxies are presented and briefly discussed in the following section. After that I will give an outlook of what could be learned from future studies in Sect. 4.3.

4.2.1 Observations and data reduction

NGC 4634 was observed with the VLA in May 2007 in D-configuration. Four observing runs with a total of 1 hour integration time (including time for calibration) resulted in approximately 2 hours on-source integration time. The observing runs were scheduled with 1 hour in between in order to get a reasonable

| Galaxy | Array | Date |
|----------|-------|--------------|
| NGC 7090 | EW352 | 2006, Jan 16 |
| | 750D | 2006, Jan 21 |
| | 1.5C | 2005, Nov 29 |
| | 6A | 2005, Dec 08 |
| | 6A | 2005, Dec 09 |
| NGC 7462 | EW352 | 2006, Jan 14 |
| | 750D | 2006, Jan 22 |
| | 1.5C | 2005, Nov 28 |
| | 6A | 2005, Dec 10 |
| | 6A | 2005, Dec 11 |

Table 4.1: *ATCA observation details.*

(u,v)-coverage. This resulted in a good coverage of parallactic angles which allowed polarization calibration. 1331+305 was used as the primary calibrator and 1221+282 for calibration and polarization and phase. The flux intensity scale of Baars et al. (1977) was adopted. The data reduction was performed in a standard fashion, using AIPS. With an angular extent of the radio emission of less than $2.5'$ (see below), the observed galaxy is small enough to fit easily into the primary beam of the VLA's 25-m antennae (HPBW = $8'$ at 4.85 GHz) and hence the missing zero-spacing flux is negligible.

NGC 7090 and NGC 7462 were observed with the Australia Telescope Compact Array¹ in November 2005, December 2005, and January 2006. Each galaxy was observed with one configuration in the 352 m array, the 750 m array, the 1.5 km array, and the 6 km array (see Table 4.1). In order to get a good (u,v)-coverage the individual observing runs were 12 hours long (including time for calibration). We obtained a total on-source integration time of 55 hours for NGC 7090 and NGC 7462. We chose to observe at 4.544 GHz and 4.800 GHz (λ 6 cm) in order to get the best sensitivity instead of observing at two (wider spaced) frequencies simultaneously. All data have been polarization calibrated. 1934-638 was used as the primary flux calibrator, 2117-642 (NGC 7090) and 2311-452 (NGC 7462) as polarization and phase calibrators. The adopted flux of 1934-638 is 5.83 Jy at 4.800 GHz. The data reduction was performed in a standard fashion, using the software package MIRIAD. With angular extents of their radio emission of less than $5'$ (see below), the observed galaxies are small enough that they fit easily into the primary beam of the ATCA's 22-m antennae (HPBW = $10'$ at 4.85 GHz). With a shortest spacing of 46 m and good (u,v)-coverage, the missing zero-spacing flux is negligible.

4.2.2 Morphology of the radio continuum emission

NGC 4634 is a member of the Virgo cluster at a distance of 19.1 Mpc (Teerikorpi et al. 1992). Bright extra-planar $H\alpha$ emission up to distances of 1.1 kpc above the galactic plane has been detected by Rossa & Dettmar (2000) with several $H\alpha$ -filaments reaching into the halo. A patch of extra-planar $H\alpha$ emission in the northwest of the galaxy disk is located 1.4 kpc above the galactic plane. From the $H\alpha$ flux density Rossa & Dettmar (2000) derived a star formation rate of $0.51 M_{\odot} \text{ yr}^{-1}$. Tüllmann et al. (2006) presented X-ray observations of NGC 4634 with an extension of the soft X-ray emission up to 4.0 kpc to the east and 2.6 kpc to the west of the disk plane. The radio continuum emission presented in Fig. 4.2 has a radial extent of $2'$ (11 kpc) and shows a peak at the center. Extra-planar continuum emission is detected in the northeastern and southwestern halo. The southwestern halo is more prominent with a vertical extension of the continuum emission up to $1'$ (5 kpc) from the disk. The polarized intensity presented in Fig. 4.3 shows a clear asymmetry between the northeastern and southwestern halo. Extra-planar

¹The Australia Telescope is funded by the Commonwealth of Australia for operation as a National Facility managed by CSIRO.

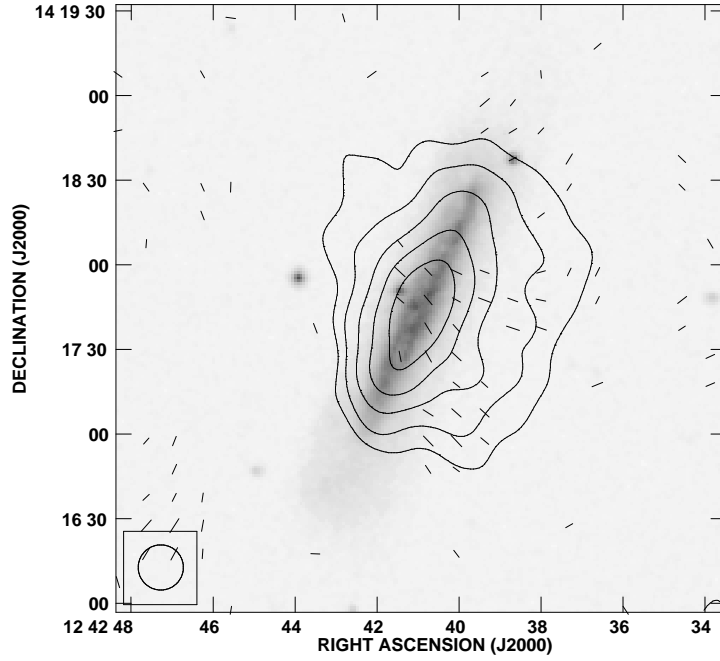


Figure 4.2: NGC 4634 total power radio continuum obtained from observations with the VLA at $\lambda 6.2$ cm. The optical image plotted in grey-scale is from the DSS. Contours are at 3, 6, 12, 24, and $48 \times 35 \mu\text{Jy}/\text{beam}$. The overlaid vectors indicate the orientation of the ordered magnetic field. The length of the vectors is defined by $1''$ to be equivalent to $25 \mu\text{Jy}/\text{beam}$ of polarized intensity.

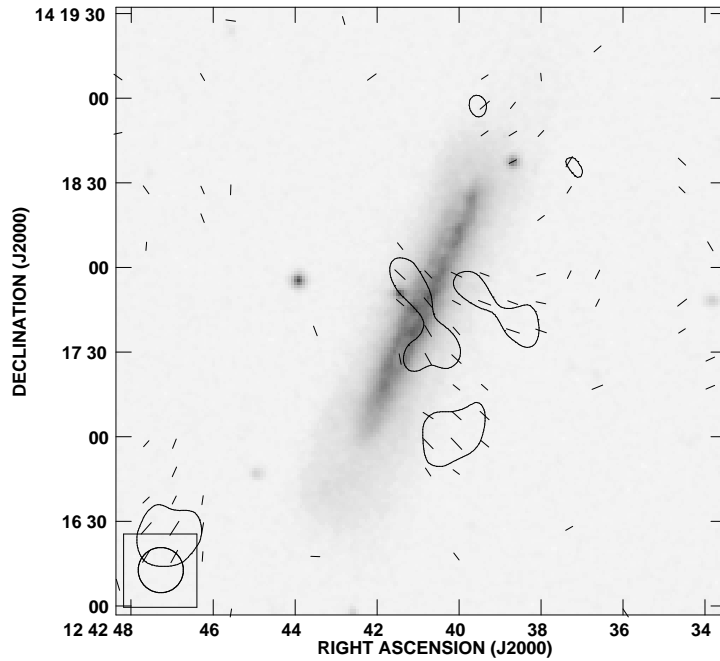


Figure 4.3: NGC 4634 polarized intensity obtained from observations with the VLA at $\lambda 6.2$ cm. Contours are at $3 \times 35 \mu\text{Jy}/\text{beam}$. The overlaid vectors indicate the orientation of the ordered magnetic field. The length of the vectors is defined by $1''$ to be equivalent to $25 \mu\text{Jy}/\text{beam}$ of polarized intensity.

polarized emission is detected only in the southeastern halo. The magnetic field orientation is strongly inclined to the major axis. There are two resolved “radio spurs” which connect the inner disk with the halo with a vertical magnetic field orientation. The northern spur coincides with the patch of extra-planar $\text{H}\alpha$ emission by Rossa & Dettmar (2000) (see their Fig. 7). The magnetic field structure indicates thus an outflow in the southwestern halo. It remains, however, unclear why the soft X-ray emission is found to be more prominent with a larger extension in the northwestern halo.

NGC 7090 (Fig. 4.4) exhibits centrally peaked radio continuum emission from its disk with a radial extent of the disk emission of about $5'$. Beside the central maximum there is a second local maximum visible southeast of the center. There are also clear indications of extra-planar emission detected in the

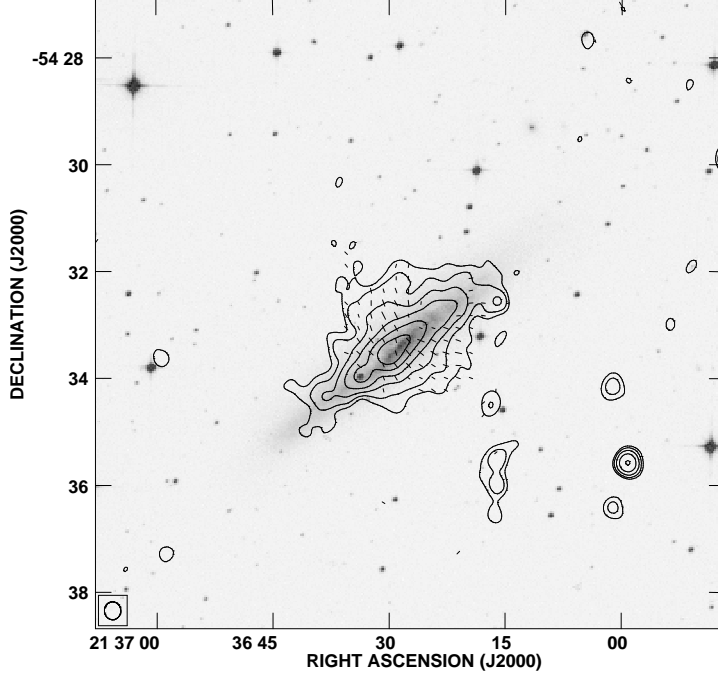


Figure 4.4: NGC 7090 total power radio continuum obtained from observations with the ATCA at $\lambda 6$ cm. The optical image plotted in grey-scale is from the DSS. Contours are at $3, 6, 12, 24, 48,$ and $96 \times 20 \mu\text{Jy/beam}$. The overlaid vectors indicate the orientation of the ordered magnetic field. The length of the vectors is defined by $1''$ to be equivalent to $12.5 \mu\text{Jy/beam}$ of polarized intensity.

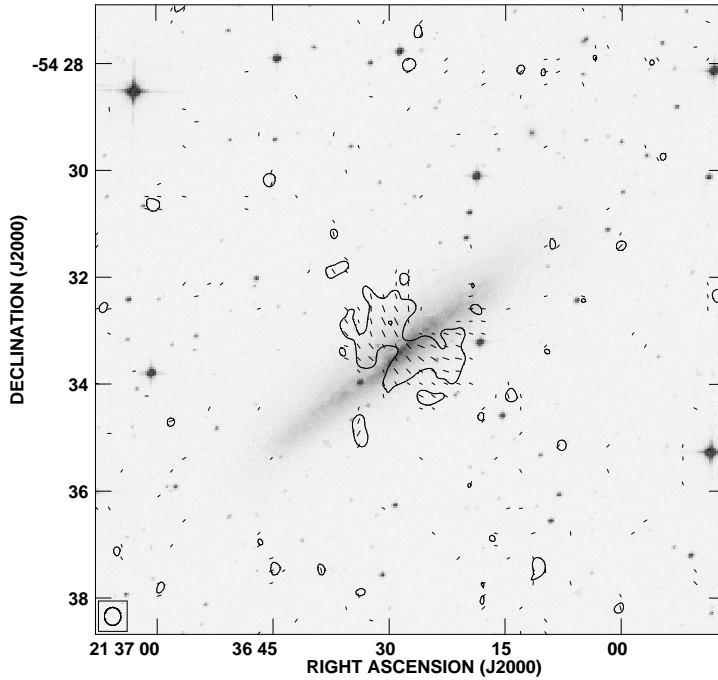


Figure 4.5: NGC 7090 polarized intensity obtained from observations with the ATCA at $\lambda 6$ cm. Contours are at 3 and $6 \times 20 \mu\text{Jy/beam}$. The overlaid vectors indicate the orientation of the ordered magnetic field. The length of the vectors is defined by $1''$ to be equivalent to $12.5 \mu\text{Jy/beam}$ of polarized intensity.

northeastern and southwestern halo, which has been already detected by Harnett & Reynolds (1985) at $\lambda 36$ cm and was confirmed by Dahlem et al. (2001) at $\lambda 13$ cm and $\lambda 20$ cm. The vertical orientation of the regular magnetic field suggests an outflow in the central regions of that galaxy. The distribution of the polarized intensity presented in Fig. 4.5 clearly shows the concentration of the polarized emission to the minor axis. The drop of polarized intensity in the plane of the disk is prominently which might be attributed to Faraday depolarization. However, with only one wavelength observed we cannot make any firm statement.

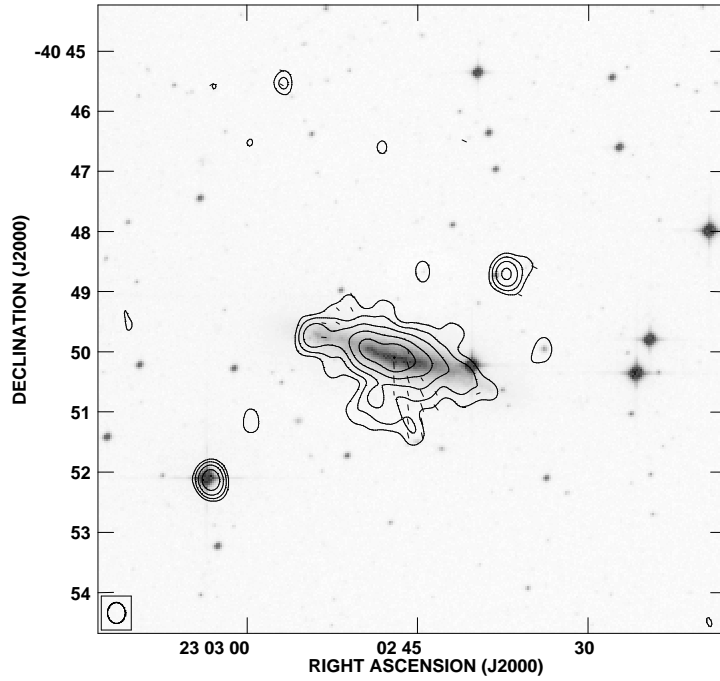


Figure 4.6: *NGC 7462 total power radio continuum obtained from observations with the ATCA at $\lambda 6$ cm. The optical image plotted in grey-scale is from the DSS. Contours are at 3, 6, 12, 24, and $48 \times 20 \mu\text{Jy/beam}$. The overlaid vectors indicate the orientation of the ordered magnetic field. The length of the vectors is defined by 1'' to be equivalent to 12.5 $\mu\text{Jy/beam}$ of polarized intensity.*

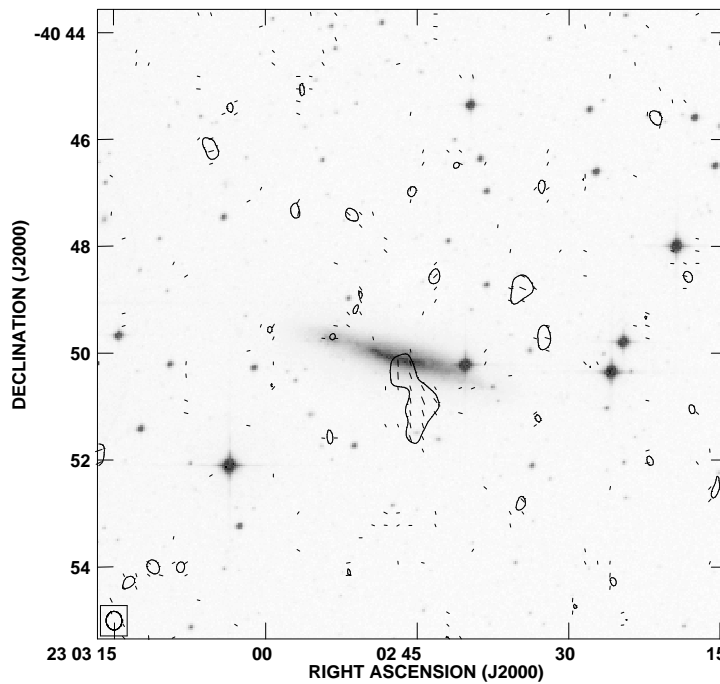


Figure 4.7: *NGC 7462 polarized intensity obtained from observations with the ATCA at $\lambda 6$ cm. Contours are at $3 \times 20 \mu\text{Jy/beam}$. The overlaid vectors indicate the orientation of the ordered magnetic field. The length of the vectors is defined by 1'' to be equivalent to 12.5 $\mu\text{Jy/beam}$ of polarized intensity.*

NGC 7462 presented in Fig. 4.6 displays centrally peaked emission in the disk with a radial extent of $3'$. The map exhibits a secondary emission maximum about $1.3'$ east of the center and a weaker corresponding maximum to the west of the nucleus. There is also some emission south of the center, outside the disk of NGC 7462. The asymmetry of the halo is apparent, the brighter emission being observed on the south side. There is a detection of extra-planar radio continuum emission from ATCA observations by Dahlem et al. (2001) at $\lambda 13$ cm and $\lambda 20$ cm. However, they did not detect any polarization. Our detection of a large-scale magnetic field in the halo of NGC 7462 confirms the existence of extra-planar emission (see Fig. 4.7). The vertical extent of polarized emission is $1.6'$ in the southern halo. The magnetic field orientation is almost exactly perpendicular to the disk. It is worthwhile to note that the ordered magnetic field is located on the western edge of the radio spur.

4.3 Outlook

A possible explanation for the observed magnetic field structure in spiral galaxies is the mean-field $\alpha\Omega$ -dynamo (Beck et al. 1996). The dynamo operates by the interaction of two magnetohydrodynamical processes (Cline et al. 2003): the production of toroidal magnetic field from poloidal field by shear (Ω -effect), and the regeneration of poloidal loops from toroidal field due to the combined action of magnetic buoyancy and Kelvin-Helmholtz instabilities (α -effect). An alternative scenario is that the presence of rotational shear and the resulting magnetic shear instability described by Balbus & Hawley (1991) can lead to strong toroidal, large-scale magnetic fields (Brandenburg et al. 1995). The magnetic fields generated by this mechanism are similar to those in ordinary $\alpha\Omega$ -dynamos.

There are only a few more examples of spiral galaxies with known polarization information for the halo. Among these, the “X”-shaped magnetic field structure is quite common as mentioned above. NGC 253 is a good example for such a configuration, where the toroidal magnetic field component dominates almost throughout the disk. Only at locations where the toroidal component is weak due to geometrical reasons the orientation of the magnetic field is perpendicular to the disk. Subtracting the dominant toroidal component a residual magnetic field with a significant vertical component was revealed, i.e. the poloidal magnetic field. In contrast to NGC 253 the structure of the large-scale magnetic field in the three newly observed spiral galaxies resembles not clearly an “X”-shape. The extra-planar polarized emission is more prominent than the polarized emission in the disk and the magnetic field orientation is almost perpendicular to the disk. This suggests a dominant poloidal magnetic field.

The conclusion is therefore that the large-scale magnetic field in spiral galaxies of the local Universe spans a wide range of configurations. These can be explained by the possible influence of several factors. First, the combined distribution of mass and star formation in the stellar disk governs the outflow pattern and thus affects the magnetic field configuration (see e.g. Dahlem et al. 2006). A galactic wind traced by the abundance of extra-planar hot gas is expected to sustain the poloidal magnetic field. Second, the shearing of the magnetic field due to the differential rotation in the disk amplifies the toroidal magnetic field. The strength of the shearing can be obtained from $H\alpha$ rotation curves. Finally, the dropping of the rotation velocity with increasing height over the disk also increases the strength of the toroidal magnetic field.

The aim of further investigations is to reveal which processes determine to the first order the structure of the toroidal and poloidal magnetic field. With the current generation of telescopes only 20 galaxies can be used to study the toroidal magnetic field (Beck 2000). However, these studies will be boosted soon by the advent of the next generation of radio telescopes, most notable the EVLA, the LOFAR, and the SKA. With these telescopes the sensitivity and resolution of radio continuum observations will be increased by several orders of magnitude. The number of objects observable in diffuse synchrotron emission can be increased by up to three orders of magnitude (Gaensler et al. 2004). Thus, observing a

large sample of spiral galaxies in radio polarimetry can help us to distinguish between the influences of the factors discussed above on the magnetic field structure.

Appendix A

High dynamic range single-dish imaging

The Effelsberg 100-m telescope has been our choice for high sensitivity, low angular resolution observations of NGC 253, which we also need to fill up the missing zero-spacing information for the interferometric $\lambda 6.2$ cm VLA observations. The combination of single-dish and interferometer data is in fact important to reveal the extended halo structures of that galaxy. However, NGC 253 is a good testbed case proving what can be done with the Effelsberg telescope mainly for two reasons: first, it has a very bright central nucleus of more than 1 Jy emission in total power. To reach a typical noise level of 1 mJy/beam requires therefore a dynamic range larger than 1000. Even when the sidelobes are only at a level of 1 % they are disturbing the total power image at signal to noise ratio of ≈ 10 . This contribution has to be disentangled from the true emission of the source. And second, it is located at a declination of -25° , which means that the elevation during the observation is less than 20° . This requires a high rigidity of the telescope construction, because any distortions of the dish lead to distortions of the telescope beam, too.

These two demands and their implications for the high dynamic range imaging with single-dish telescopes will be discussed in this appendix on the example of the Effelsberg 100-m telescope. First, we show in section A.1 how we constructed appropriate beam patterns for the Effelsberg telescope in order to match the beam of the actual observations of NGC 253. Second, we apply in section A.2 the well known procedure that reconstructs the true emission pattern from the sidelobes affected observations: the so-called "CLEAN"-algorithm was originally introduced by Högbom (1974) in order to correct interferometric observations. This algorithm can be applied to single-dish observations as well. In section A.3 we will extend the cleaning procedure to polarization maps in order to remove the instrumental effects which are generally referred to as *instrumental polarization*.

A.1 Constructing the beam pattern

A.1.1 Observations and data reduction

A difference of much practical relevance between the cleaning of single-dish and interferometric observations is the availability of an appropriate beam pattern. Whereas the interferometric (u,v)-data set directly provides a beam pattern by computing the Fourier-transform of the (u,v)-coverage, single-dish observations lack this possibility. Here, additional observations have to be made specifically for the cleaning purpose. This can be accomplished by deep observations of a non-polarized point source which lead to a map that defines the response of the telescope to the point source. This obtained beam pattern of the single-dish telescope can be regarded as *Point Spread Function (PSF)* known from optical astronomy.

We note that the dynamic range of the beam pattern must be equal or higher than that of the maps to be cleaned.

The observations which had to be cleaned were obtained with the Effelsberg telescope at $\lambda 6.2$ cm and at $\lambda 3.6$ cm. For a starting point we chose Effelsberg beam patterns from the archive which included patterns at both wavelengths. These first attempts were unsatisfying as there were large parts in the map, which had negative flux density more than 5 times the actual noise level. The missing fluxes occurred especially in regions extending around the nucleus and could be attributed to the cleaning. Hence, we concluded that the beam patterns of the archive were not accurate enough to match the actual observations and new observations had to be made in order to get high quality beam patterns.

We chose the bright point source 3C84 as target to obtain new beam patterns. Observations were performed during the year of 2005 by R. Beck. The elevation of the telescope during the observations of 3C84 was specifically chosen to be roughly $\eta = 20^\circ$ corresponding to the observations of NGC 253. In order to improve the quality of the final map several coverages scanned in perpendicular directions were obtained. We used circular Gauss-fits in order to check the position of the point-source prior to the combination of the individual maps. The reached accuracy was $10''$ and $5''$ for the $\lambda 6.2$ cm and $\lambda 3.6$ cm maps, respectively. The $\lambda 6.2$ cm-receiver consists of two horns (dual-horn receiver) whereas the $\lambda 3.6$ cm-receiver has only one horn (single-horn receiver). The Picture A.1 of the secondary focus cabin (SFK) of the 100-m Effelsberg telescope shows the position of the feed horns. Hence, the construction of the beam pattern is slightly different for both receivers.

For the dual-horn $\lambda 6.2$ cm-receiver the so-called restoration process makes use of the two horns in order to subtract time dependent weather effects. It has turned out that the restoration process is not suited to obtain the beam pattern as there were some residuals left especially at the left/right flanks of the sidelobes. Thus we omitted the restoration and constructed the beam pattern using the mean of all maps.

The single-horn $\lambda 3.6$ cm maps were combined in each Stokes RR and LL channel individually and thus two beam patterns for the Stokes RR and LL channel were obtained. These were needed in order to clean the channels separately. However, for the presentation of the beam pattern we present the mean of both channels which are anyway not very much different either.

Additionally to the beam pattern obtained from the 3C84 observations we constructed another $\lambda 6.2$ cm beam pattern from calibrator measurements of the source 0237-23. The construction process was identical to the one presented above.

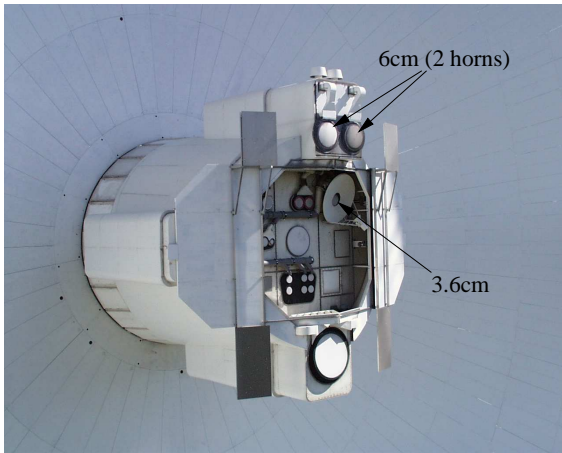


Figure A.1: Secondary focus cabin (SFK) of the 100-m Effelsberg telescope. The position of the $\lambda 6.2$ cm and $\lambda 3.6$ cm is depicted by arrows.

A.1.2 The Effelsberg beam pattern

In this section I discuss the actual beam pattern of the Effelsberg telescope. Although much attention has been paid in order to make the beam pattern almost Gaussian, there are nevertheless considerable deviations from this ideal shape. These come mainly from several different contributions, namely:

- The four legs of the primary reflector cast a shadow on the surface of the dish. This obstruction of the reflecting area decreases the effective aperture of the telescope but even more importantly are the two-fold symmetric sidelobes which extend around the central part of the beam.
- The shape of the dish is elevation dependent as gravity distorts the dish differently in the horizontal and vertical position. The outer rim of the Effelsberg telescope deforms by about 60 mm when the telescope is tilted from zenith to horizon (Rohlfs & Wilson 2004). The Effelsberg telescope is build such that the distortion proceeds in a *homologous* way. Otherwise observations with the telescope would severely be affected by the large elevation dependent distortion. Still, the remaining deviations of the parabolic shape cause flux to be transferred from the main-beam into the sidelobes.

I will briefly discuss some of the general features of the beam pattern: the central part has an almost Gaussian shape which covers 95 % of the dynamic range. The non-circular shape of the central part of the beam reminds of a slight sawtooth-pattern. It can be attributed to the observational setup of the single-dish Effelsberg maps. In this so-called “scanning”-mode the beam of the telescope sweeps in lines back and forth over the source (see Fig. A.2). The map is hence constructed by converting the time-dependent signal to a position dependent signal. Considering a small time-shift in the pointing of the telescope shifts the emission once too far left and too far right as the telescope sweeps horizontally in lines over the source. Thus one can explain the sawtooth-pattern for the central part of the beam pattern which should ideally be a Gaussian (Mack 2005).

Four lines of sidelobes are found around the central part for all beam patterns at the level of a few percent with several maxima and minima along the lines. They are aligned with the telescope i.e. the azimuth-elevation coordinate-system (*az-el*), because the beam patterns are caused by the single-dish surface and its reflector legs. In the following I will discuss in particular the properties of the sidelobes because they have the dominant influence on the cleaning process.

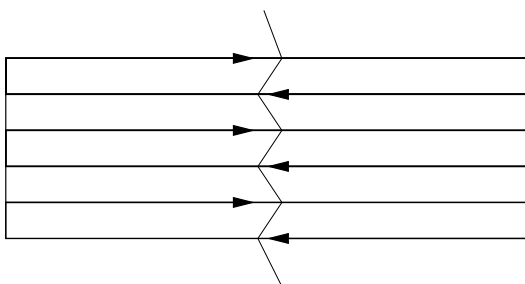


Figure A.2: *Scanning procedure of the Effelsberg maps. The beam sweeps back and forth over the scanned area. The map is eventually reconstructed at each point. A small time shift in the pointing can introduce a sawtooth pattern as observed in the beam patterns.*

A.1.3 Elevation dependent sidelobes

In this section I discuss the properties of the sidelobes and especially the dependence on the observing elevation. The beam patterns are observed in the *az-el* coordinate system, the maps have been mirrored at the vertical axis. This corrects for the opposite direction of the azimuthal angle (increasing from left to right) with respect to the direction of the right ascension (decreasing from left to right). Thus the

maps show the sky appearance of 3C84. The sidelobes are aligned with the north-south and east-west orientation because of the az-el coordinates. The maps have been transformed using AIPS to the observed position of NGC 253 to give a better comparison with the object to be cleaned.

The beam patterns at $\lambda 6.2$ cm are shown in Figs. A.3, A.4 and A.5 for the elevations of $\eta = 55^\circ$, $\eta = 40^\circ$, and $\eta = 20^\circ$, respectively. The first two beam patterns are very similar with the northern sidelobe being the most prominent one. This is in contrast to the third beam pattern, which shows the strength of the southern sidelobe to exceed the northern one. In Table A.1 we have summarized the properties of the sidelobes for our various beam patterns for a quantitative discussion. We can see that the beam patterns ($\eta = 55^\circ$ and $\eta = 40^\circ$) from the archive have a northern sidelobe with a peak value of 2.7 % of the total peak flux and a southern sidelobe at only 1.4 %. The third beam pattern shows the opposite behavior with the northern sidelobe at 1.7 % and the southern sidelobe at 2.9 %. This behavior can be attributed to an elevation difference but also to the restoration of the Effelsberg-dish (where new panels were installed), which was undertaken after the observations of the archived beams. Hence, we found the new patterns to match the actual beam of the observations only poorly, because the cleaning with the new patterns caused deep holes north of the nucleus. Therefore we chose for the cleaning a pattern obtained from calibration measurements of the source 0237-23 shown in Fig. A.6, which was obtained during the observations of NGC 253 at a low elevation of $\eta = 20^\circ$. The observations of 3C84 were however useful to apply the correction for the instrumental influence on the polarization (see below).

The situation is different for the $\lambda 3.6$ cm beam patterns. The archived pattern at $\eta = 40^\circ$ shown in Fig. A.7 has a strong southern sidelobe (3.4 %) and a weak northern sidelobe (0.9 %). The new pattern at $\eta = 20^\circ$ shown in Fig. A.8 has roughly equal sidelobes in the north (1.6 %) and south (2.0 %). This explains why the cleaning with the archived patterns caused deep holes south of the nucleus.

| elevation | 55° | 40° | 20° | 45° | 20° |
|-----------------------------|-------|-------|-------|-------|-------|
| λ [cm] | 6.2 | 6.2 | 6.2 | 3.6 | 3.6 |
| flux peak [mJy/beam] | 27150 | 27236 | 16698 | 16372 | 15325 |
| flux N-sidelobe [mJy/beam] | 721 | 745 | 288 | 135 | 262 |
| flux W-sidelobe [mJy/beam] | 554 | 609 | 281 | 293 | 301 |
| flux S-sidelobe [mJy/beam] | 374 | 373 | 484 | 527 | 329 |
| flux E-sidelobe [mJy/beam] | 500 | 516 | 267 | 225 | 273 |
| flux ratio N-sidelobe [%] | 2.65 | 2.74 | 1.69 | 0.88 | 1.60 |
| flux ratio W-sidelobe [%] | 2.04 | 2.24 | 1.65 | 1.91 | 1.84 |
| flux ratio S-sidelobe [%] | 1.38 | 1.37 | 2.85 | 3.44 | 2.01 |
| flux ratio E-sidelobe [%] | 1.84 | 1.89 | 1.57 | 1.47 | 1.66 |
| flux ratio polarization [%] | 2.14 | 1.93 | 1.04 | 0.958 | 0.858 |

Table A.1: *Beam properties of the 100-m Effelsberg telescope at $\lambda 6.2$ cm and $\lambda 3.6$ cm. The values are obtained from observations of the unpolarized point source 3C84 respectively. The elevations of $\eta = 55^\circ$ and $\eta = 40^\circ$ ($\lambda 6.2$ cm) and $\eta = 45^\circ$ ($\lambda 3.6$ cm) represent the standard beam patterns whereas the observations at $\eta = 20^\circ$ were carried out especially for cleaning at low elevations (see text).*

The radio receivers of the Effelsberg telescope have been designed in order to detect polarized emission. But on the level of a few percent the total power contributes also to the polarized emission. This intrinsically receiver leakage causes, in the presence of strong total power emission, a significant contribution to the polarized emission. This is the dominant contribution to the instrumental polarization for

the Effelsberg telescope. Thus, we choose 3C84 to be our target for obtaining the beam patterns not only because it is a strong radio source but also because it is almost unpolarized. This allows us to obtain also beam patterns in Stokes Q and U , which show the response of the Effelsberg telescope to a total power point source. The corresponding beam patterns of 3C84 in Stokes Q and U are presented in Figs. A.9 and A.10 for $\lambda 6.2$ cm and in Figs. A.11 and A.12 for $\lambda 3.6$ cm. Though the instrumental polarization is only at the level of 1 % for our new obtained beam patterns this still results in more than 10 mJy of polarized flux caused by the nucleus. Thus we have corrected this influence of the high dynamic range using the beam patterns as described in section A.3.

A.2 The cleaning procedure

A.2.1 The Högbom cleaning

The measured map is the convolution of the true emission in the sky with the beam of the telescope, thus the beam has to be deconvolved from the measured map. In the previous section I explained how to obtain an appropriate beam pattern for a single-dish telescope. The deconvolution can be best done in the Fourier domain, where the Fourier-transform of the map is simply divided by the Fourier-transform of the beam (according to Parseval's theorem). However, this is not applicable for interferometric measurements as the (u,v) -plane is not entirely filled since there are always missing (u,v) -visibilities. Now the deconvolution in the Fourier space would require the division by zero, which obviously leads to numerical problems. Högbom (1974), however, could show that the deconvolution can be successfully done in the image plane as well. He assumed the radio sky to be a random distribution of point sources on an empty background, where the emission consists of point sources with a Gaussian emission profile. The well known Högbom algorithm now replaces the response of a point source including sidelobes with a Gaussian. Starting with the highest intensities and proceeding to the low intensities all emission in the map is replaced by Gaussians. It has turned out that the algorithm works also very well on extended structures though it was originally designed for point sources only. Nowadays it is the most wide-spread method to remove sidelobes from interferometric observations.

Based on the Högbom algorithm Klein & Mack (1995) have designed a cleaning algorithm for the Effelsberg telescope. The program “clean” uses the NOD2-library (Haslam 1974) and runs only on Solaris UNIX-machines. The program expects two input maps in NOD-format: the beam pattern in az-el coordinates and the map to be cleaned given in Ra-Dec coordinates. If the beam pattern has to be mirrored before use (because of the az-el observing mode of Effelsberg), the program offers an option to do this. The so-called loop-gain is multiplied with each cleaning-component prior to subtraction from the map. Factors between 0.02 and 0.25 are recommended. In principle, the smaller the factor the more accurate is the cleaning as the numbers of cleaning components is larger. However, in practice it has turned out that the result was not much improved for factors smaller than 0.1. This may depend also on the structure of the emission so this value has to be adjusted to obtain a sufficient cleaning procedure. The most important parameter is, however, the cleaning threshold. The cleaning algorithm has to be stopped at least when the noise is reached. Moreover, the cleaning algorithm does not converge if there are too many cleaning components with a negative flux. The best results cleaning the Effelsberg maps were obtained when using only very few negative cleaning components. Hence, the cleaning threshold was adjusted such that the fraction of negative cleaning components remained small (for details see Tab. A.2).

The cleaning then needs another important parameter and that is the so-called *parallactic angle*. This is the angle between the beam pattern and the northern direction in the map to be cleaned. One has to remember that the beam pattern always stays in the az-el observing frame as the beam pattern is connected directly to the Effelsberg-telescope which has an alt-azimuthal mount. The parallactic angle is

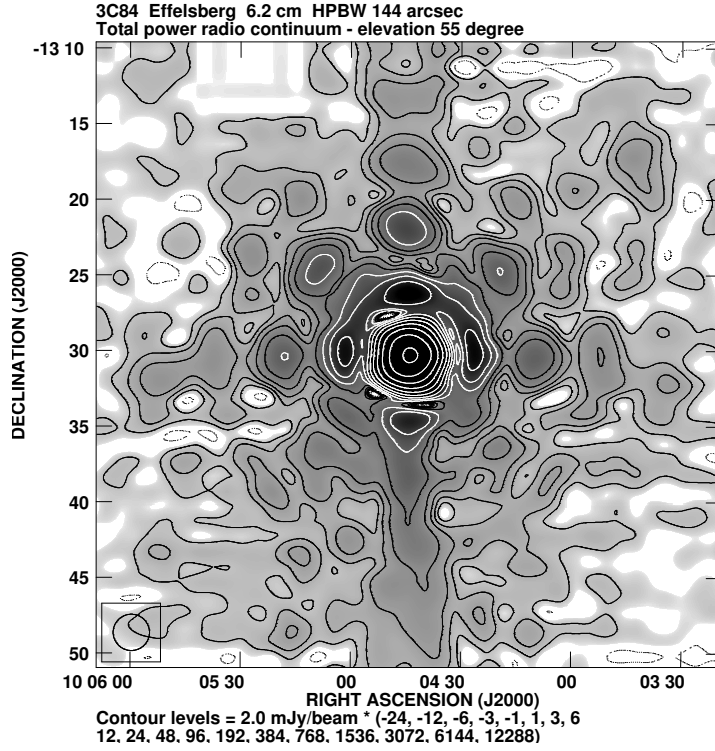


Figure A.3: 3C84 Effelsberg $\lambda 6.2$ cm total power distribution obtained at an elevation of $\eta = 55^\circ$. Contours are at -24, -12, -6, -3, -1, 1, 3, 6, 12, 24, 48, 96, 192, 384, 768, 1536, 3072, 6144, and 12888×2 mJy/beam. Note that the northern sidelobe is most prominent in contrast to the observation obtained at a lower elevation of $\eta = 20^\circ$ (Fig. A.5).

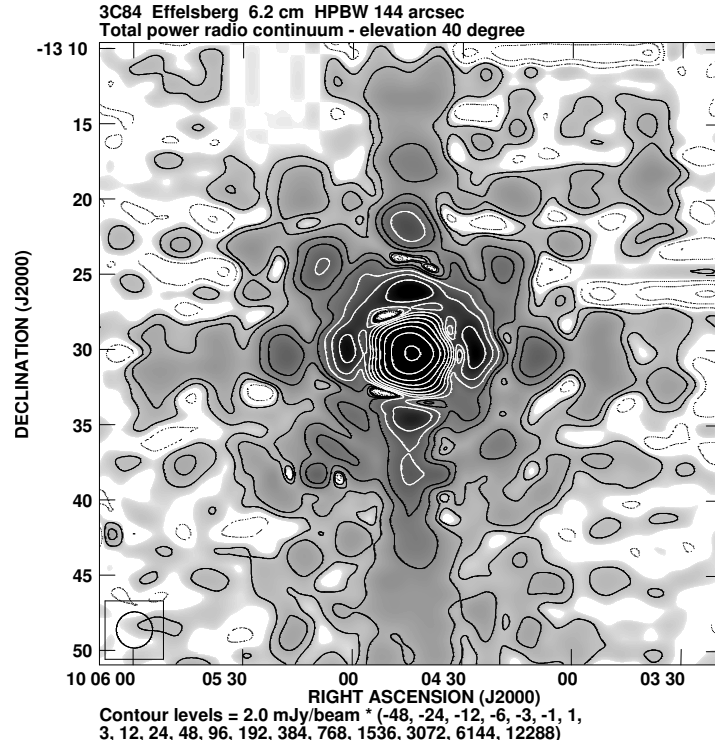


Figure A.4: 3C84 Effelsberg $\lambda 6.2$ cm total power distribution obtained at an elevation of $\eta = 40^\circ$. Contours are at -48, -24, -12, -6, -3, -1, 1, 3, 6, 12, 24, 48, 96, 192, 384, 768, 1536, 3072, 6144, and 12888×2 mJy/beam. This beam pattern is very similar to the beam pattern at $\eta = 55^\circ$ shown in Fig. A.3.

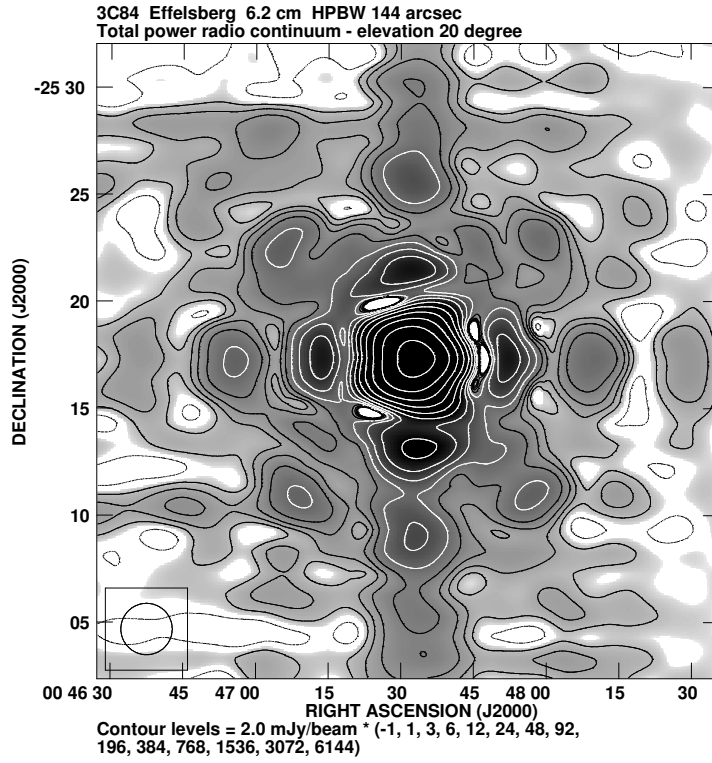


Figure A.5: 3C84 Effelsberg $\lambda 6.2$ cm total power distribution obtained at an elevation of $\eta = 20^\circ$. Contours are at -1, 1, 3, 6, 12, 24, 48, 96, 192, 384, 768, 1536, 3072, and 6144 $\times 2$ mJy/beam. The comparison with the $\lambda 3.6$ cm observations (Fig. A.8) shows the similarity of the beam patterns.

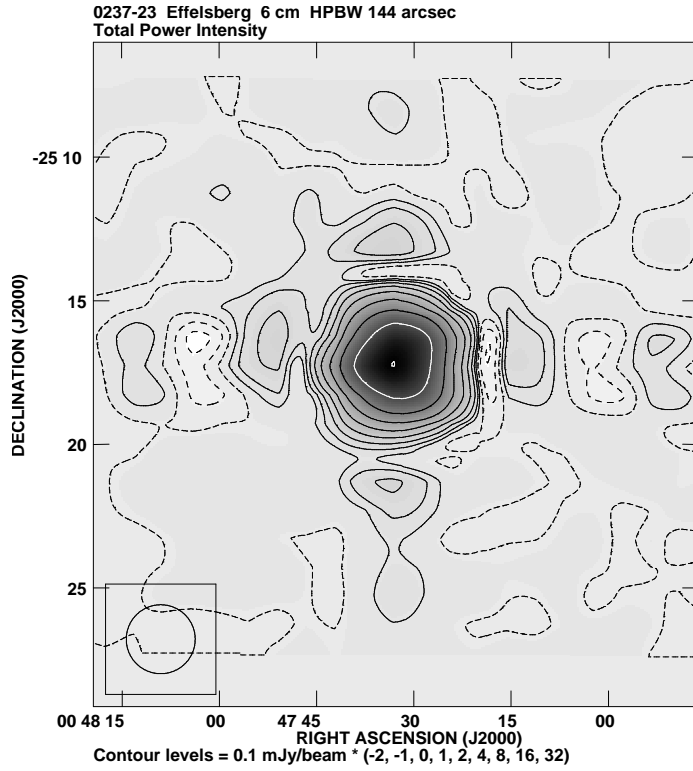


Figure A.6: 0237-23 Effelsberg $\lambda 6.2$ cm total power distribution obtained at an elevation of $\eta = 20^\circ$. Contours are at -2, -1, 0, 1, 2, 4, 8, 16, and 32 $\times 0.1$ Jy/beam. This observation was used as a calibrator source for the observation of NGC 253. To be compared with Fig. A.5.

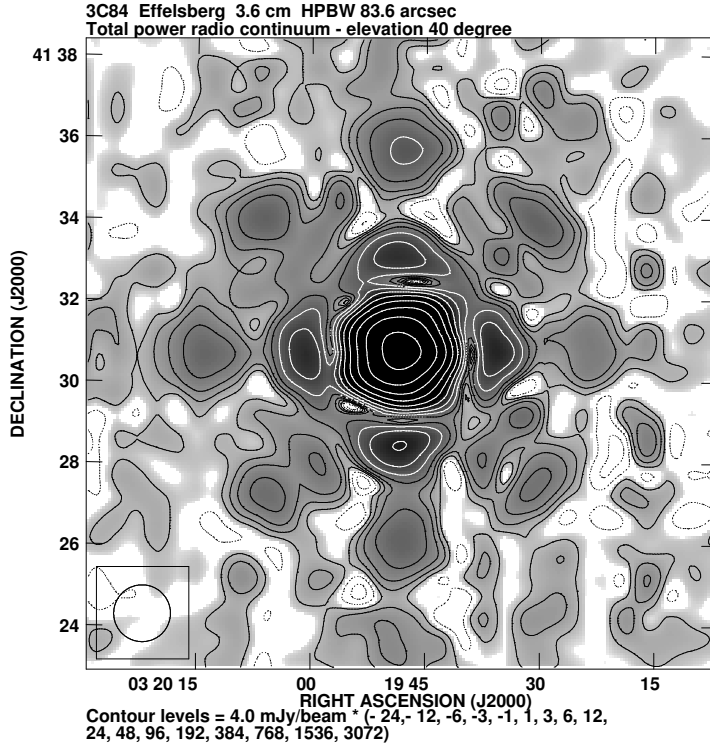


Figure A.7: 3C84 Effelsberg $\lambda 3.6$ cm total power obtained at an elevation of $\eta = 40^\circ$. Contours are at -24, -12, -6, -3, -1, 1, 3, 6, 12, 24, 48, 96, 192, 384, 768, 1536, and 3072×4 mJy/beam. Note that the northern sidelobe is significantly more prominent compared with the observation obtained at a lower elevation of $\eta = 20^\circ$ (Fig. A.8).

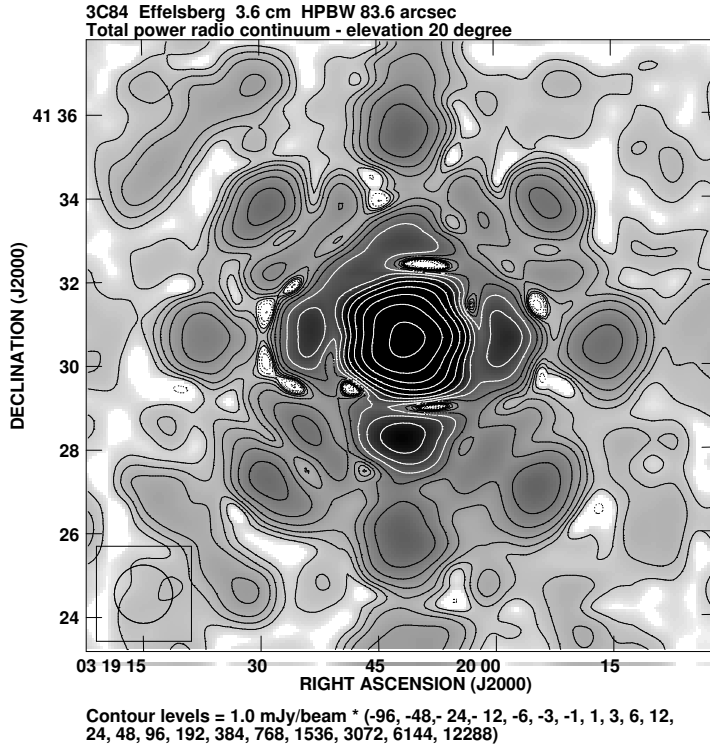


Figure A.8: 3C84 Effelsberg $\lambda 3.6$ cm total power distribution obtained at an elevation of $\eta = 20^\circ$. Contours are at -96, -48, -24, -12, -6, -3, -1, 1, 3, 6, 12, 24, 48, 96, 192, 384, 768, 1536, 3072, 6144, and 12288×1 mJy/beam. The asymmetric shape of the central beam part is notable as the contours are not exactly circular. The sidelobes also are not symmetric as the southern one is the most prominent.

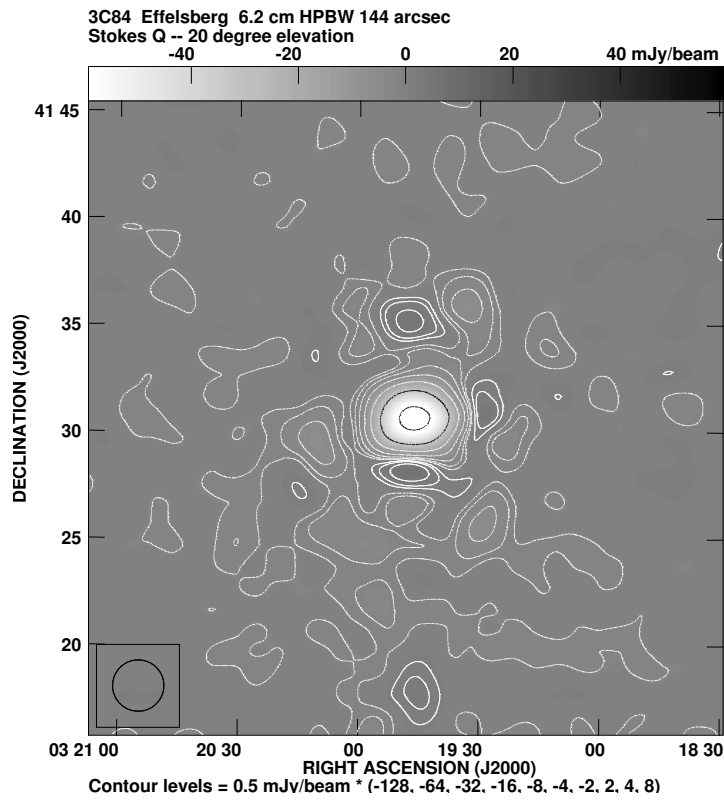


Figure A.9: *3C84 Effelsberg* $\lambda 6.2$ cm distribution of Stokes Q obtained at an elevation of $\eta = 20^\circ$. Contours are at -128, -64, -32, -16, -8, -4, -2, 2, 4, and 8×0.5 mJy/beam.

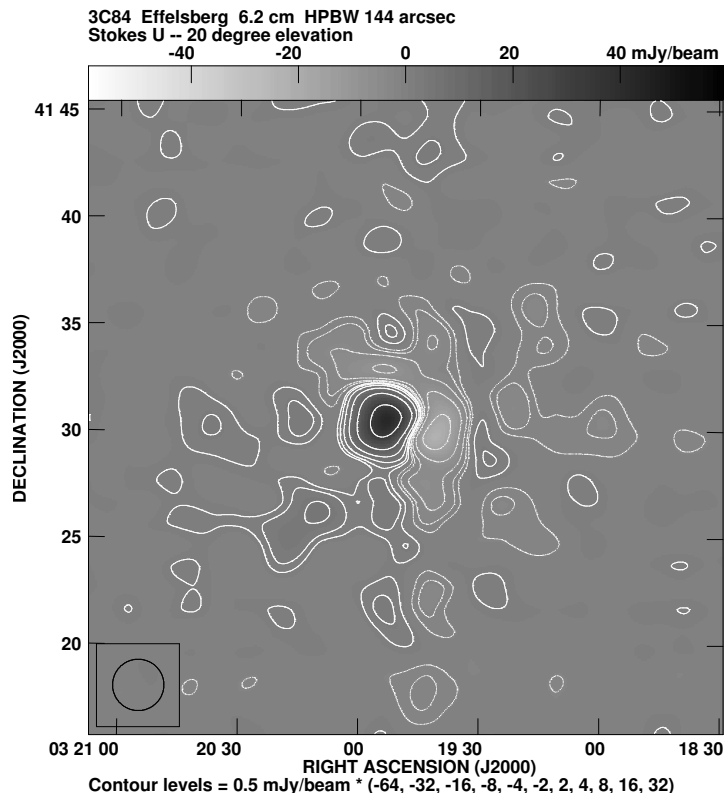


Figure A.10: *3C84 Effelsberg* $\lambda 6.2$ cm distribution of Stokes U obtained at an elevation of $\eta = 20^\circ$. Contours are at -64, -32, -16, -8, -4, -2, 2, 4, 8, 16, and 32×0.5 mJy/beam.

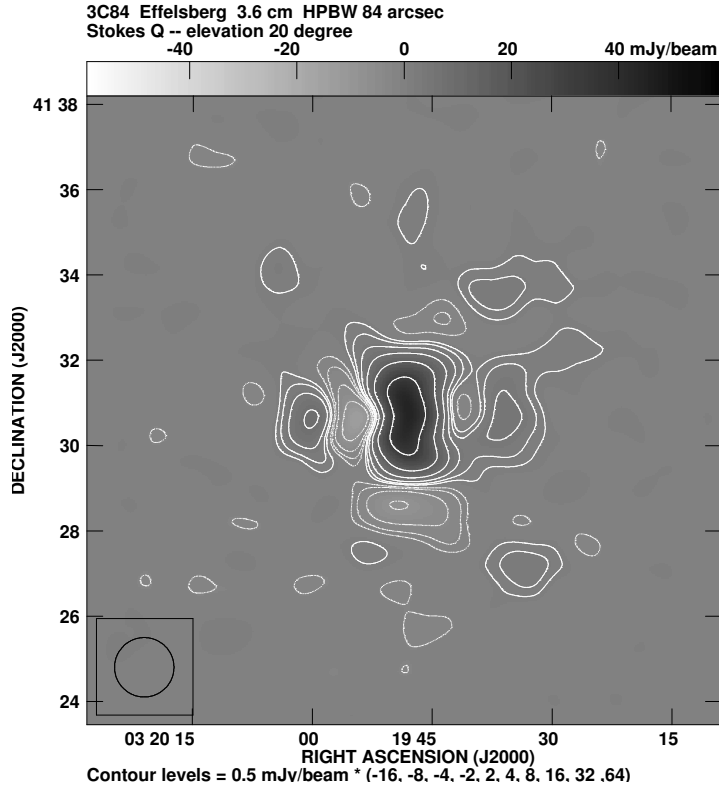


Figure A.11: *3C84 Effelsberg* $\lambda 3.6$ cm distribution of Stokes Q obtained at an elevation of $\eta = 20^\circ$. Contours are at -16, -8, -4, -2, 2, 4, 8, 16, 32, and 64×0.5 mJy/beam.

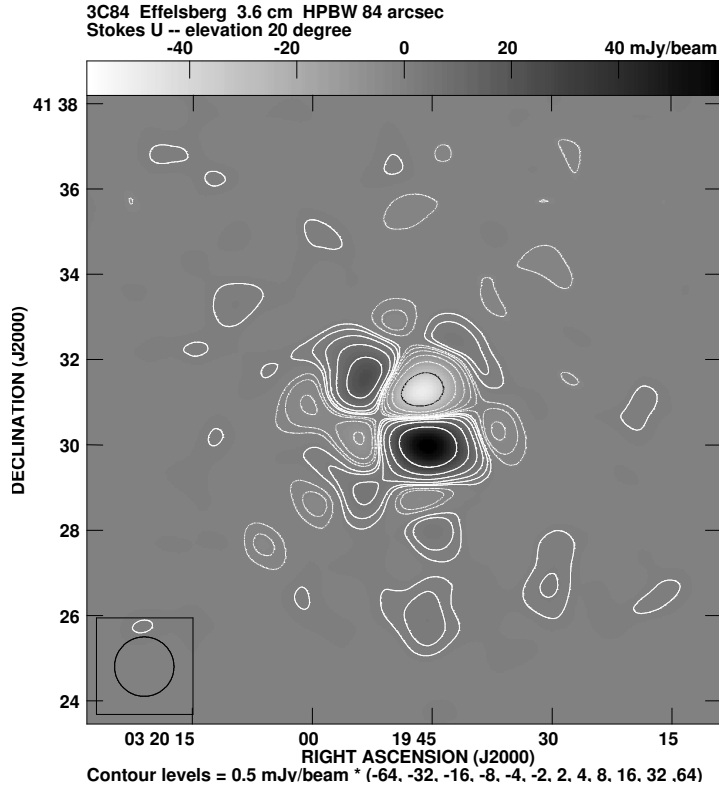


Figure A.12: *3C84 Effelsberg* $\lambda 3.6$ cm Stokes U obtained at an elevation of $\eta = 20^\circ$. Contours are at -16, -8, -4, -2, 2, 4, 8, 16, 32, and 64×0.5 mJy/beam.

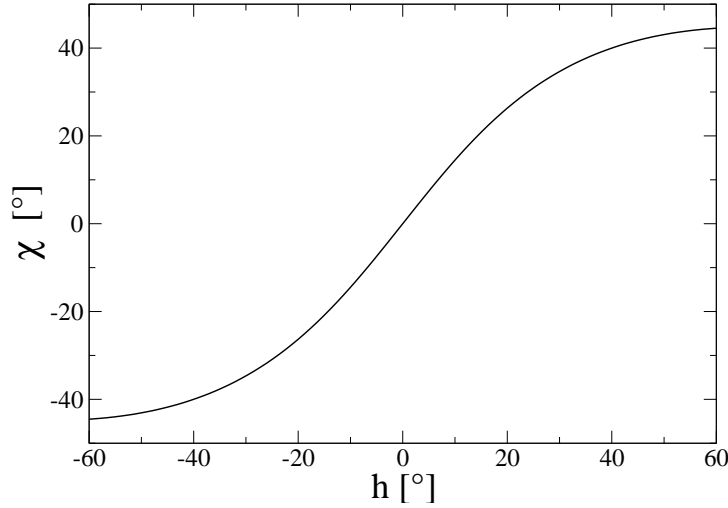


Figure A.13: *Computed parallactic angle χ of NGC 253 as function of the hour angle h as described in equation A.1.*

not constant but varies with time and has to be computed for each map separately. It can be determined from the following expression (Klein 1978):

$$\chi = \pm \arctan \left(\frac{\cos \phi \sin h}{\sin \phi \cos \delta - \cos \phi \sin \delta \cos h} \right) \begin{cases} + & \text{if } \delta \geq 0 \\ - & \text{otherwise} \end{cases} \quad (\text{A.1})$$

Here, χ is the parallactic angle, ϕ the geographic latitude of the telescope, h the hour angle, and δ the declination of the observed object. Figure A.13 shows the parallactic angle as a function of the sidereal time for NGC 253 at the geographic latitude $\phi_{\text{Eff}} = 50.525^\circ$ of the Effelsberg telescope. Moreover, the angle of each separate scan is included in the revised NOD-2 header. Each map has been cleaned with a parallactic angle according to the sidereal time of the observation. I took the mean parallactic angle during the observation of a single map. Choosing a constant parallactic angle for the cleaning is sufficient as the change of the parallactic angle is small (typically 10°) during the scanning of a single map. For large maps it is necessary to deconvolve each point of the map with its appropriate parallactic angle.

| λ [cm] | Loop-Gain | Threshold [rms] |
|----------------|-----------|-----------------|
| 6.2 | 0.1 | 90 |
| 3.6 | 0.1 | 30 |

Table A.2: *Parameters for the single-dish cleaning.*

The $\lambda 6.2$ cm maps have been cleaned after the restoration with the beam-switching method in Stokes I . The $\lambda 3.6$ cm maps have been cleaned in the Stokes channels RR and LL separately. Finally, all cleaned total power maps were combined using the “PLAIT” algorithm by Emerson & Gräve (1988). It makes use of the perpendicular directions¹ of the scanning in order to suppress irregularities in the baselevels of each scan. It has turned out that the use of “PRESSE” applied on each cleaned total power map prior to the combination is not suitable. PRESSE performs a Fourier transformation similar to PLAIT but can be applied on maps with only one scanning direction. However, the total power was increased along the major axis of NGC 253 but decreased further off the major axis (see Fig. A.14). This change is

¹The scanning direction is chosen that the direction is either parallel or perpendicular to the major axis of NGC 253.

drastically visible in the spectral index maps, which showed a very steep spectral index between $\lambda 6.2$ cm and $\lambda 3.6$ cm. The cleaned total power maps are discussed in section (A.2.2).

Finally, I would like to add a general comment on the presented procedure of cleaning single-dish observations. In his diploma thesis H. Rottmann developed the program "CLEANER", which addressed the presented shortcomings of the cleaning procedure for the single-dish (Rottmann 1996). Due to technical problems I was unfortunately not able to use the program but I successfully processed our Effelsberg maps through all the necessary steps "by hand". It would be highly desirable to get such program again, since it would be possible to clean Effelsberg maps straight forward even for non-experienced observers.

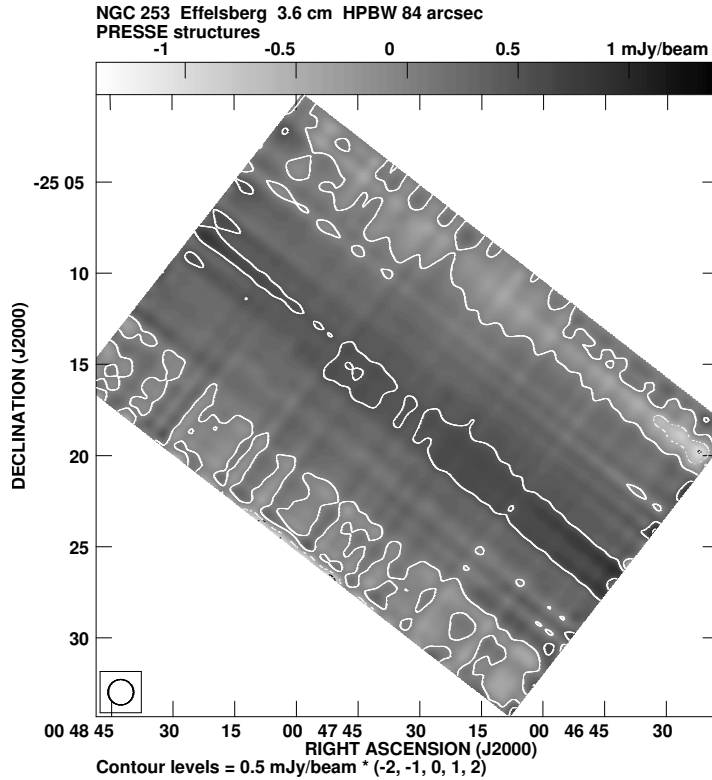


Figure A.14: *NGC 253 PRESSE structures at $\lambda 3.6$ cm, i.e. the difference between the total power map (not processed with PRESSE) and the total power map (processed with PRESSE).*

A.2.2 The cleaned total power maps

Figure A.15 shows the uncleaned total power map of NGC 253 at $\lambda 6.2$ cm. The contour lines are not clipped at the noise level in order to give an impression of the background emission, which is on average constant over the entire field. The contour lines show huge extensions at weak levels especially in the northwestern part. In the southeastern part we notice much emission which gives the impression of a huge halo. The cleaned map presented in Fig. A.16 shows much different structures: the contour lines in the northwestern are less extended than prior to the cleaning. This map was used to be combined with the VLA observations at the same wavelength in order to fill up the missing zero-spacing flux (for details see section B.1).

Figure A.17 shows the uncleaned total power map of NGC 253 at $\lambda 3.6$ cm. There seems to be a lot of halo emission, actually the southeastern part of the halo has even a box shaped halo. Figure A.18 shows the result after the cleaning procedure for NGC 253 at $\lambda 3.6$ cm. Much of the halo emission has vanished. The southeastern part of the halo has been split up into two broad extensions, one associated with the

already noted point source, the other one south of of the nucleus. Moreover, the contour lines follow better the outline of the galactic disk in the central part of the galaxy. Thus a good deal of the deviations can be attributed to the sidelobes of the strong central total power emission.

More insight in the contribution of the telescope beam is shown by the difference between the uncleaned and the cleaned total power maps (the "cleaning structures"). The cleaning structures are shown in Figs. A.19 and A.20 for $\lambda 6.2$ cm and $\lambda 3.6$ cm, respectively. The contour plots resemble well the beam pattern with the uncleaned total power emission underlying as grey-scale. It is obvious that the extension of the sidelobes is larger at $\lambda 6.2$ cm compared to $\lambda 3.6$ cm, because the beam size is larger.

A.3 Instrumental polarization

This section describes how the influence of the nuclear point source from our Effelsberg polarization maps has been removed. For this I use the beam patterns in Stokes Q and U , which have been already presented in Sect. A.1. In order to apply the correction of the instrumental polarization the beam patterns and the maps to be cleaned have to be transformed to an identical coordinate system for which I chose the Ra-Dec coordinate system. The $\lambda 6.2$ cm, observations, of NGC 253 were carried out in the Ra-Dec system thus there was no need for a transformation. The $\lambda 3.6$ cm observations, however, were made in coordinate system which is aligned with the major axis of NGC 253 in order to reduce the time expense for sweeping between the scanning lines. Moreover, the observations of 3C84 to obtain the beam patterns have been made in a coordinate system tilted by a parallactic angle of roughly 45° . Thus the Stokes Q and U quantities are defined in a coordinate system tilted by a constant angle against the Ra-Dec coordinate system: the so-called internal coordinate system. How they were transformed to the Ra-Dec coordinate system I will briefly explain in the following.

A.3.1 The transformation of Stokes Q and U

In order to make the transformation from the internal coordinate system to the Ra-Dec coordinate systems I use the definition of Stokes Q and U on the Poincaré sphere (Rohlf & Wilson 2004):

$$\begin{aligned} Q &= S_0 \cos(2\chi) \cos(2\psi) \\ U &= S_0 \cos(2\chi) \sin(2\psi). \end{aligned} \quad (\text{A.2})$$

Here S_0 is a constant quantity, which can be eliminated. Also we can set $\chi = 0$ when we make the assumption of Stokes $V = 0$ (no circular polarization). In fact the circular polarization from most astrophysical objects is negligible compared to the linear polarization. Thus this assumption is well justified. The polarization angle ψ is defined by:

$$\psi = \frac{1}{2} \arctan\left(\frac{U}{Q}\right). \quad (\text{A.3})$$

The polarization angle is measured in the coordinate system defined by Q and U . The Polarization vector \vec{P} intrinsically emitted by an astrophysical source is coordinate independent. Thus the polarization angle ψ is transformed to $\psi' = \psi + \Delta\psi$, when the rotation angle is $\Delta\psi$. In order to fulfill the equation A.3 we have to transform Stokes Q and U . From equation A.2, respectively from the sketch in Fig. A.21, we obtain Stokes Q' and U' in the rotated coordinate system:

$$\begin{aligned} Q' &= Q \cos(2\Delta\psi) - U \sin(2\Delta\psi) \\ U' &= Q \sin(2\Delta\psi) + U \cos(2\Delta\psi). \end{aligned} \quad (\text{A.4})$$

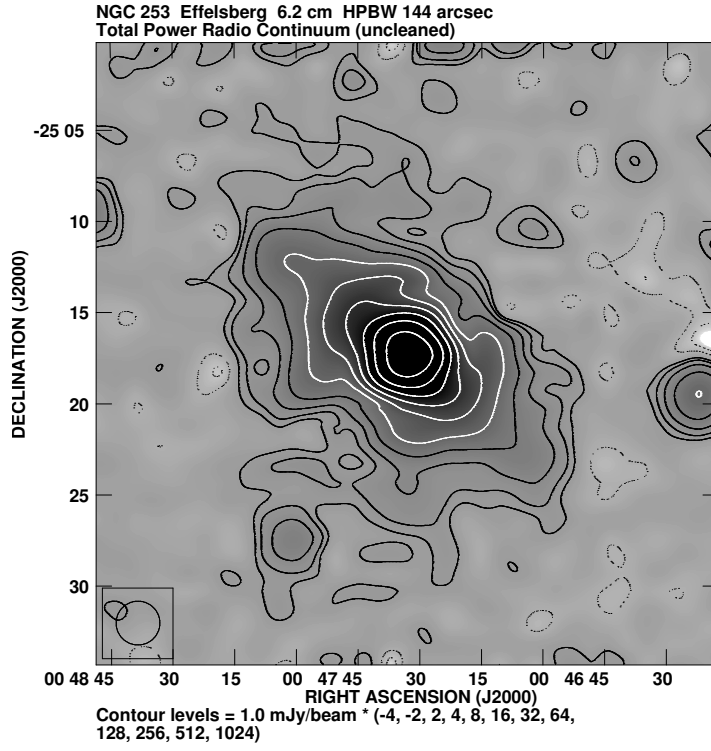


Figure A.15: NGC 253 Effelsberg $\lambda 6.2$ cm total power radio continuum (uncleaned). Contours are at -4, -2, -2, 4, 8, 16, 32, 64, 128, 256, 512, and 1024×1 mJy/beam.

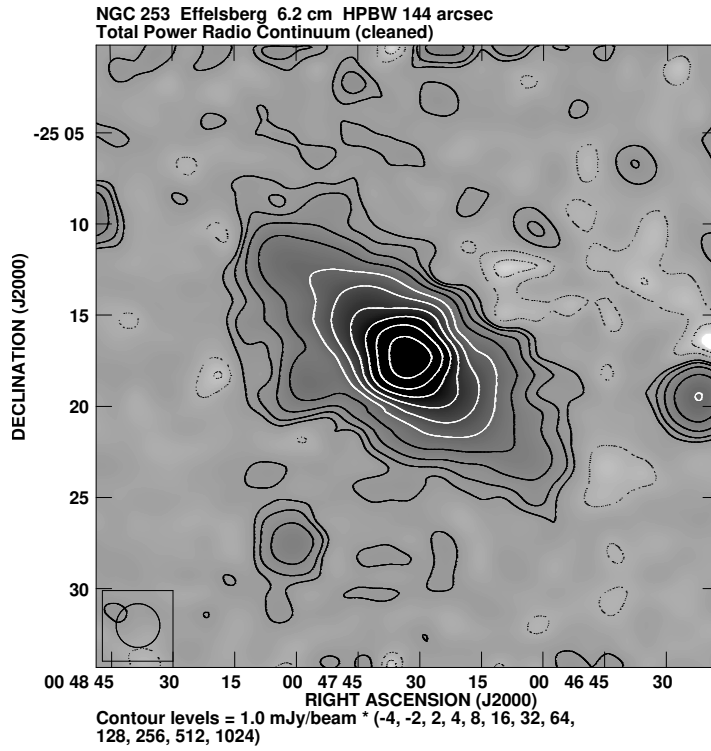


Figure A.16: NGC 253 Effelsberg $\lambda 6.2$ cm total power radio continuum (cleaned). Contours are at -4, -2, 2, 4, 8, 16, 32, 64, 128, 256, 512, and 1024×1 mJy/beam. To be compared with Fig. A.15.

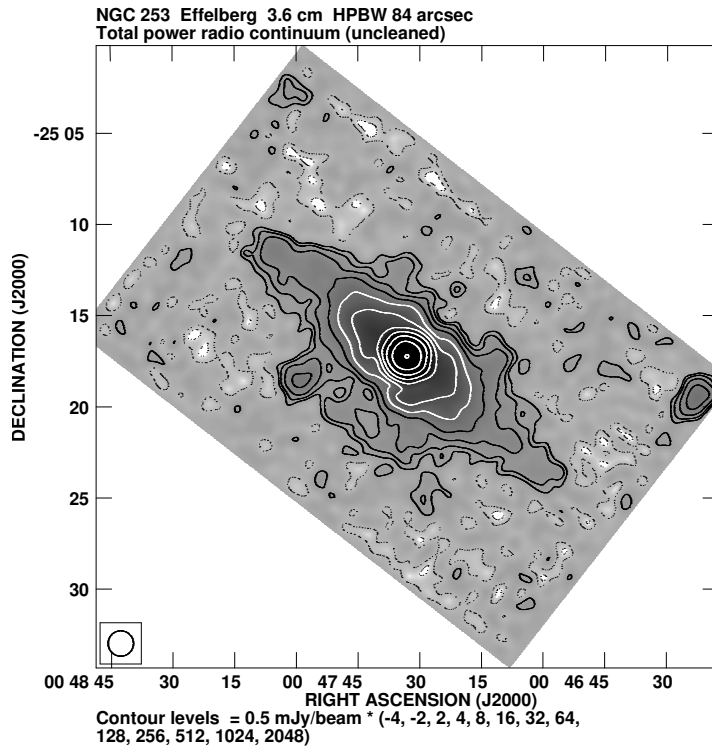


Figure A.17: *NGC 253 Effelsberg total power radio continuum $\lambda 3.6 \text{ cm}$ map (uncleaned). Contours are at $-4, -2, 2, 4, 8, 16, 32, 64, 128, 256, 512, 1024$, and $2048 \times 0.5 \text{ mJy/beam}$.*

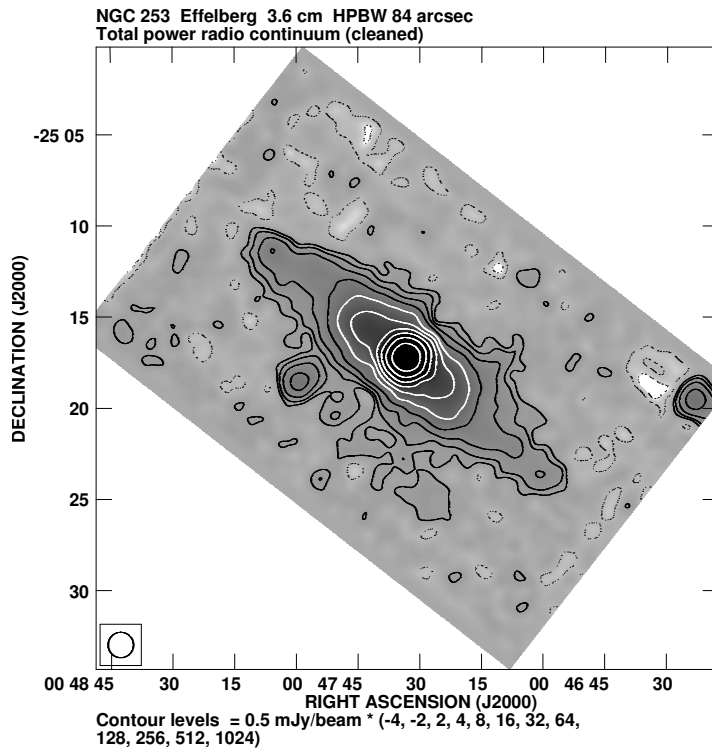


Figure A.18: *NGC 253 Effelsberg $\lambda 3.6 \text{ cm}$ total power radio continuum (cleaned). Contours are at $-4, -2, 2, 4, 8, 16, 32, 64, 128, 256, 512$, and $1024 \times 0.5 \text{ mJy/beam}$. To be compared with Fig. A.17.*

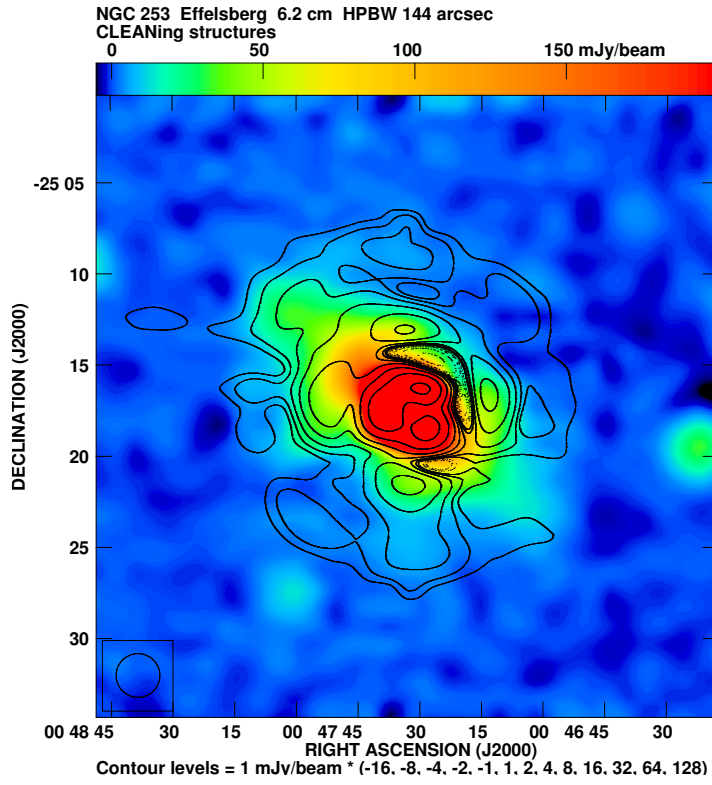


Figure A.19: *NGC 253 Effelsberg λ 6.2 cm cleaning structures on top of the uncleaned total power map. The map of the cleaning structures is defined as the difference between the uncleaned total power map and the cleaned total power map. Contours are at -16, -8, -4, -2, 2, 4, 8, 16, 32, 64, and 128×1 mJy/beam.*

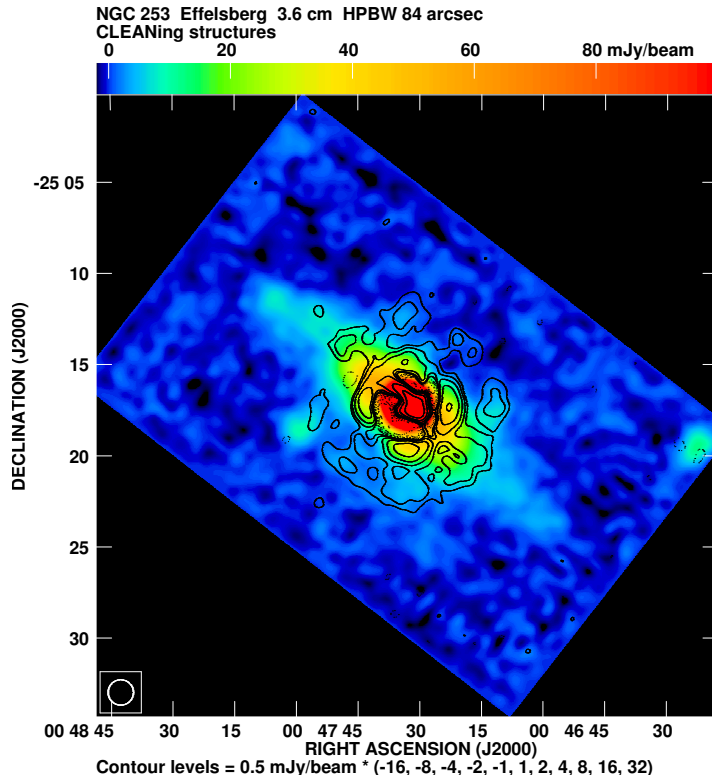


Figure A.20: *NGC 253 Effelsberg λ 3.6 cm cleaning structures on top of the uncleaned total power map. Contours are at -16, -8, -4, -2, -2, 4, 8, 16, and 32×0.5 mJy/beam.*

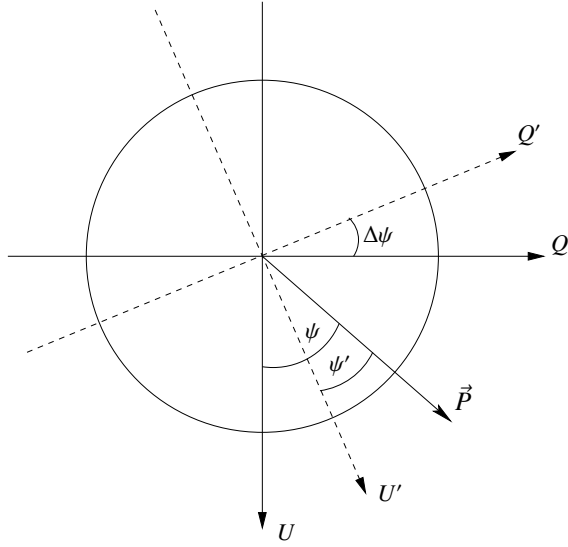


Figure A.21: The arbitrary coordinate system of the polarization measurement defines Stokes Q and U . The Polarization vector \vec{P} intrinsically emitted by an astrophysical source is coordinate independent. Thus the polarization angle ψ is transformed to $\psi' = \psi + \Delta\psi$, when the rotation angle is $\Delta\psi$. To make ψ' fulfill the relation A.3 the observed quantities Stokes Q and U are transformed to Q' and U' which define the rotated coordinate system.

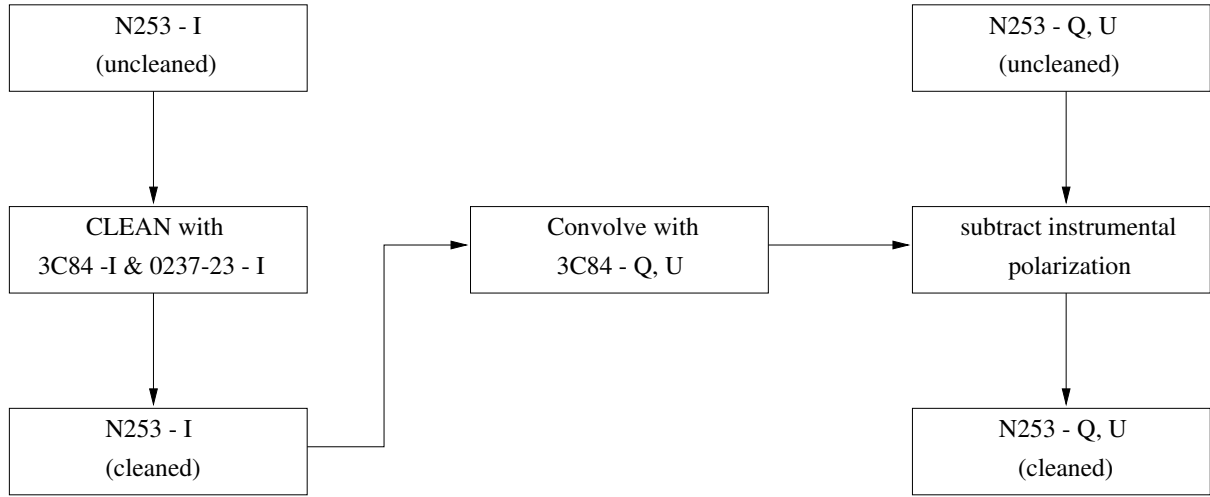


Figure A.22: Block diagram of the single-dish cleaning procedure used for NGC 253. The individual steps are described in the text.

The position angle of the major axis of NGC 253 is $PA = -38^\circ$. Performing the transformation according to equation A.4 yields the maps in the Ra-Dec coordinate system. The transformation angle is near to 45° . It can be easily derived from Fig. A.21 that in this case the Stokes Q map is transformed into the Stokes U map and the Stokes U map is transformed into the Stokes Q map with inverse sign. Hence, one has to check very carefully whether the transformation has been done correctly.

A.3.2 The Effelsberg polarization maps

For the correction of the instrumental polarization I assumed a constant parallactic angle since the change of the parallactic angle during the observation of a single map is less than 5° . The mean parallactic angle of the individual maps deviates not more than 8° from the mean of *all* maps which is $\chi = 0^\circ$. Hence

I applied the correction of the instrumental polarization on the final map of NGC 253 in the Ra-Dec coordinate system.

In order to compute the instrumental response to the total power emission, I convolved the cleaned total power map with the beam pattern in Stokes Q and U , respectively. The computed instrumental corrections for $\lambda 6.2$ cm are presented in Figs. A.23 and A.24 for Stokes Q and U , respectively. These maps were subtracted from the observed Stokes Q and U maps of NGC 253 shown in Figs. A.25 and A.26. The resulting cleaned maps are shown in Figs. A.27 and A.28 for Stokes Q and U , respectively. The influence of the instrumental polarization can be easily inferred by comparing the uncleaned and cleaned maps. In the uncleaned Stokes Q map we find map an elongated region of negative emission connecting the northern halo with the southern halo. This region is replaced with an elongated region of positive emission aligned east-west in the cleaned map. In the uncleaned Stokes U map we find a small blob of positive emission east of the nucleus which is almost completely removed by the cleaning. The impact of the instrumental polarization can be inferred from the comparison of the uncleaned (Fig. A.29) and the cleaned (Fig. A.30) polarized intensity maps, too. The maximum of the polarized intensity is significantly lowered by the cleaning. Moreover, the two depolarization regions associated with the radio spurs appear less prominent in the cleaned maps with the drop of polarized emission less prominently.

The computed instrumental corrections for $\lambda 3.6$ cm are presented in Figs. A.31 and A.32 for Stokes Q and U , respectively. These maps were subtracted from the uncleaned Stokes Q and U maps of NGC 253 shown in Figs. A.33 and A.34. The resulting cleaned maps of NGC 253 are presented in Figs. A.35 and A.36 for Stokes Q and U , respectively. For Stokes Q we find the cleaning to remove an elongated region of negative emission extending north-south by an elongated region of positive emission elongated east-west similar to the cleaning at $\lambda 6.2$ cm. For Stokes U the cleaning removes the absolute minimum of the emission west of the nucleus. The comparison of the polarized intensity maps in Figs. A.37 (uncleaned) and A.38 (cleaned) shows again that the depolarization regions are less prominent in the cleaned map. Again, as for the $\lambda 6.2$ cm observations, the maximum of polarized emission is lowered by the cleaning. This is reasonable as the contribution of the instrumental polarization to the polarized flux has been removed.

The careful cleaning and correction of the instrumental polarization was not only needed for obtaining the Effelsberg maps at $\lambda 6.2$ cm and at $\lambda 3.6$ cm. The $\lambda 6.2$ cm Stokes Q and U maps were moreover used to fill up the missing zero-spacing flux of the interferometric $\lambda 6.2$ cm VLA observations (see Appendix B). There we compare also the polarization maps observed with the VLA with the Effelsberg maps. This gives more justification of the methods applied in the data reduction.

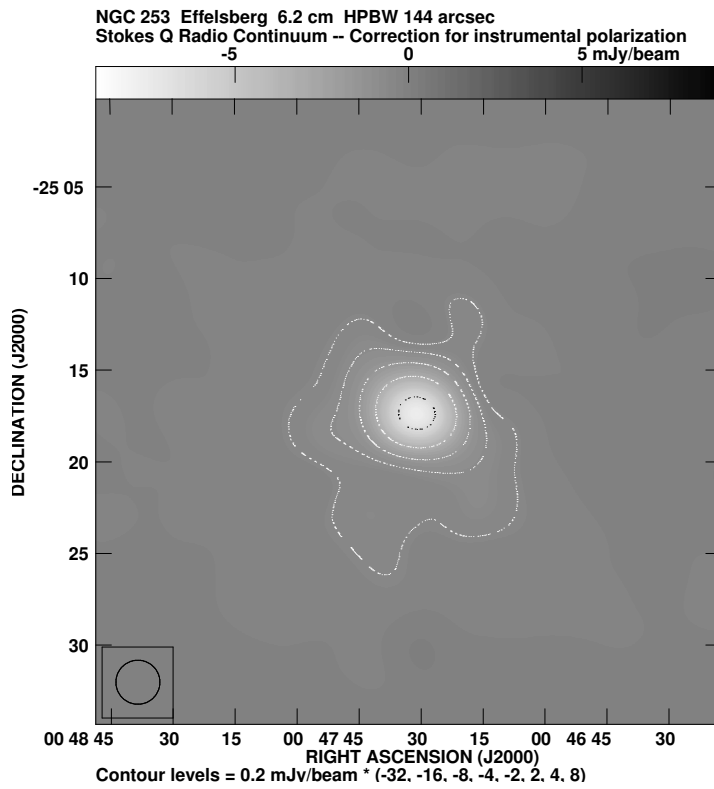


Figure A.23: NGC 253 Effelsberg $\lambda 6.2$ cm distribution of the instrumental correction in Stokes Q . Contours are at -32, -16, -8, -4, -2, 2, 4, and 8×0.2 mJy/beam.

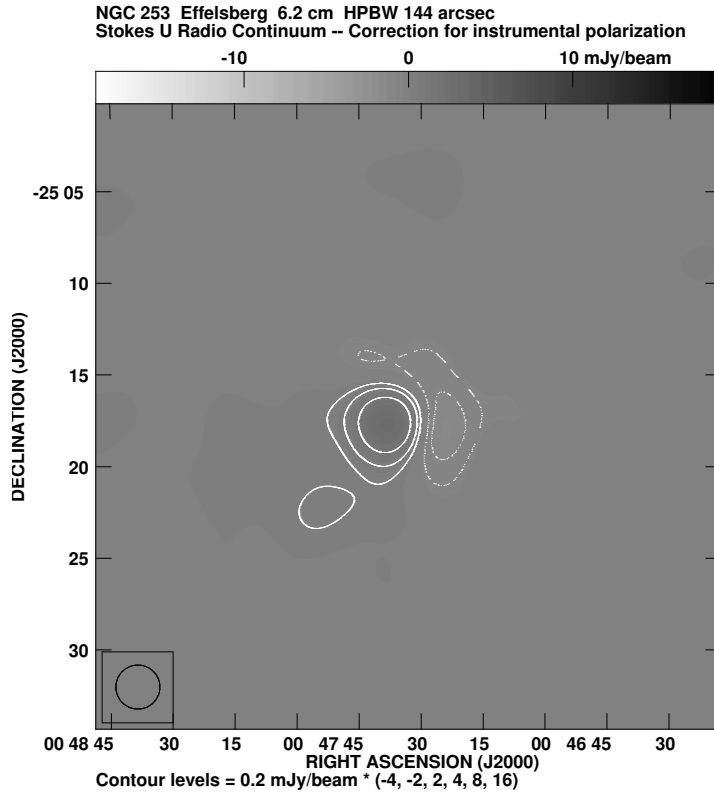


Figure A.24: NGC 253 Effelsberg $\lambda 6.2$ cm distribution of the instrumental correction in Stokes U . Contours are at -4, -2, 2, 4, 8, and 16×0.2 mJy/beam.

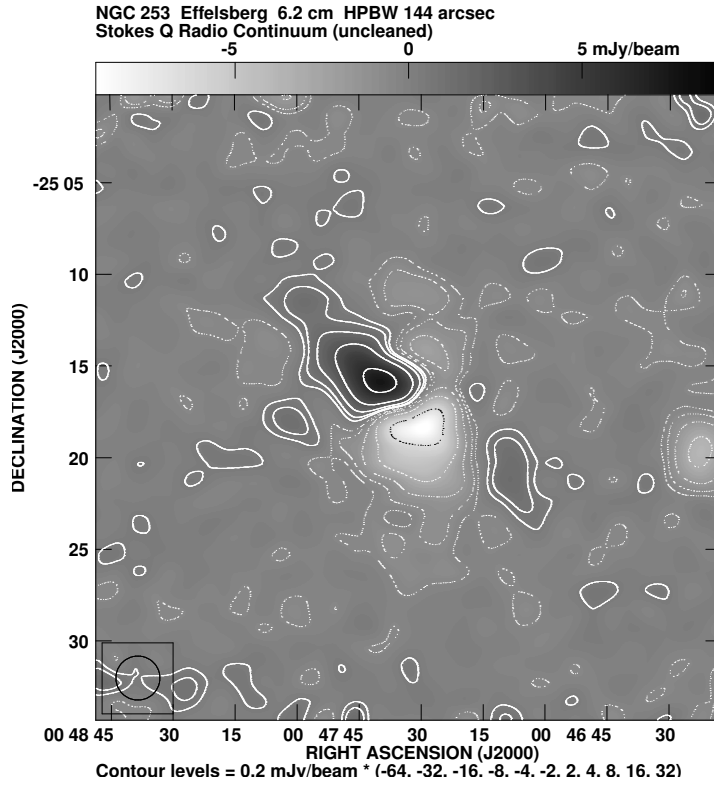


Figure A.25: NGC 253 Effelsberg $\lambda 6.2$ cm distribution of Stokes Q (uncleaned). Contours are at -64, -32, -16, -8, -4, -2, 2, 4, 8, 16, and 32×0.2 mJy/beam.

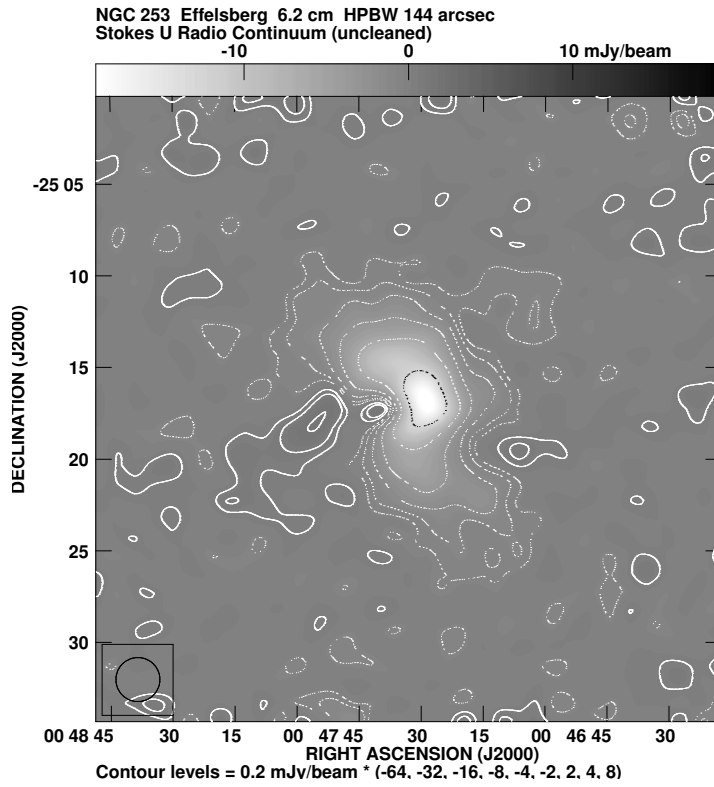


Figure A.26: NGC 253 Effelsberg $\lambda 6.2$ cm distribution of Stokes U (uncleaned). Contours are at -64, -32, -16, -8, -4, -2, 2, 4, and 8×0.2 mJy/beam.

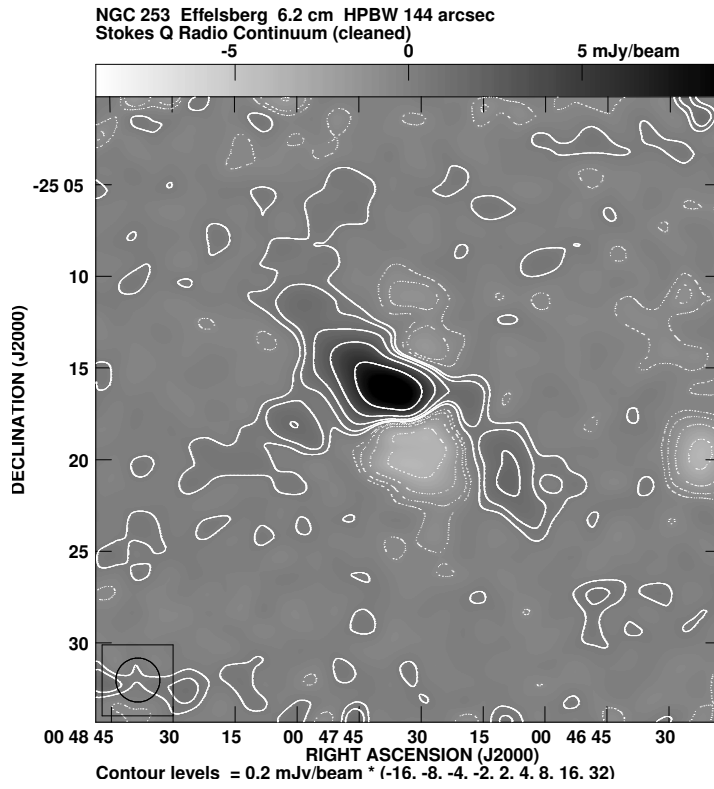


Figure A.27: NGC 253 Effelsberg $\lambda 6.2 \text{ cm}$ distribution of Stokes Q (cleaned). Contours are at $-16, -8, -4, -2, 2, 4, 8, 16, \text{ and } 32 \times 0.2 \text{ mJy/beam}$. To be compared with Fig. A.25.

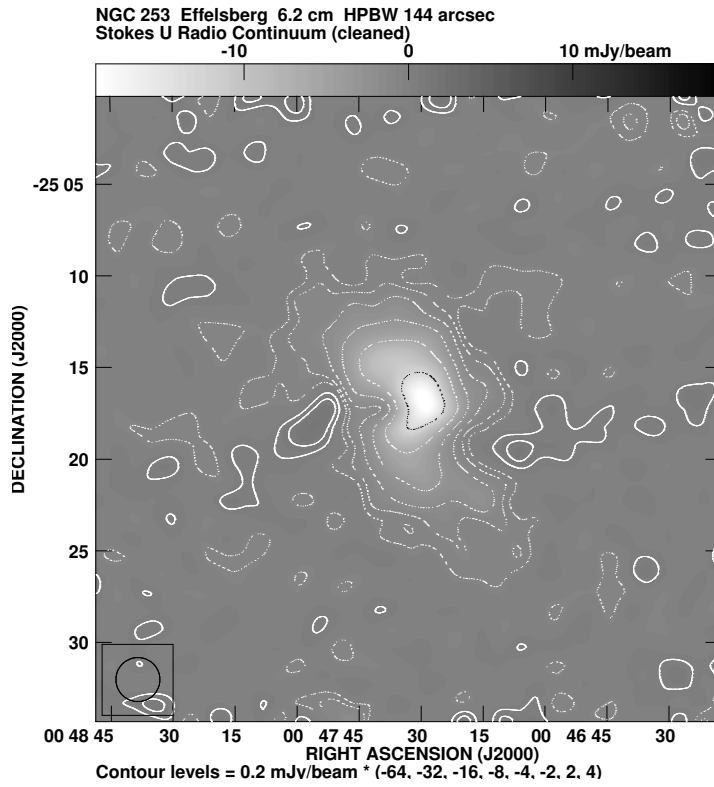


Figure A.28: NGC 253 Effelsberg $\lambda 6.2 \text{ cm}$ distribution of Stokes U (cleaned). Contours are at $-64, -32, -16, -8, -4, -2, 2, \text{ and } 4 \times 0.2 \text{ mJy/beam}$. To be compared with Fig. A.26.

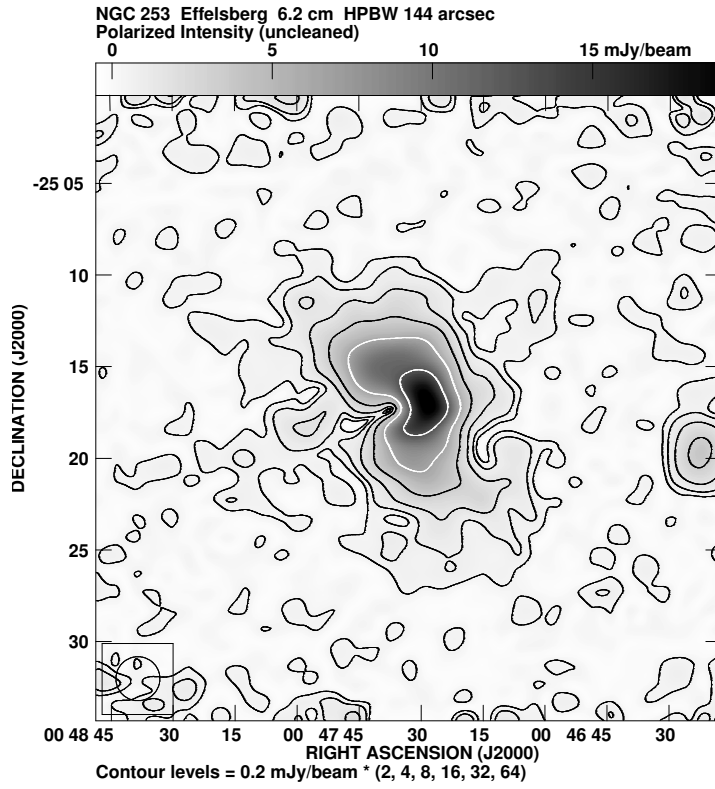


Figure A.29: NGC 253 Effelsberg $\lambda 6.2 \text{ cm}$ distribution of polarized intensity (uncleaned). Contours are at 2, 4, 8, 16, 32, and $64 \times 0.2 \text{ mJy/beam}$.

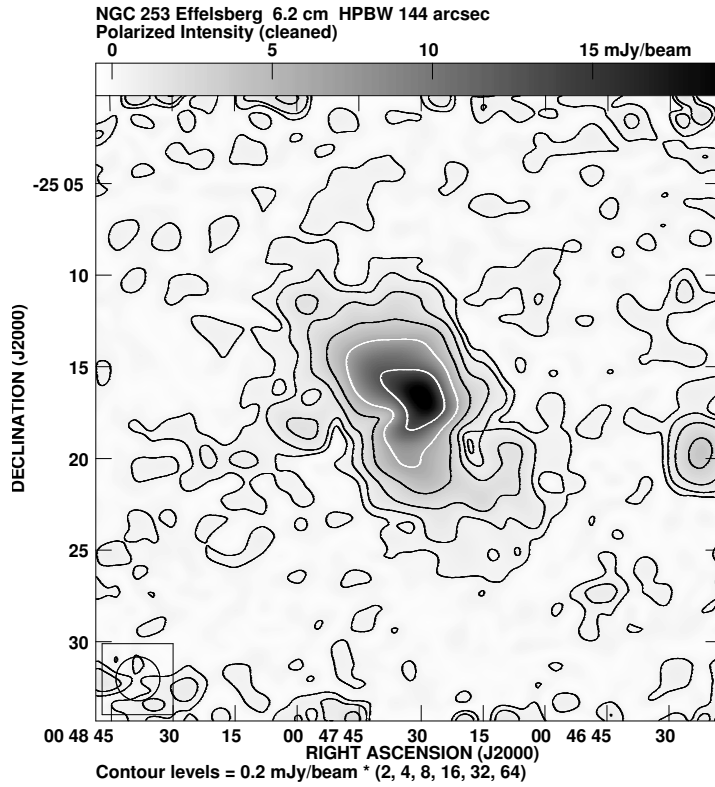


Figure A.30: NGC 253 Effelsberg $\lambda 6.2 \text{ cm}$ distribution of polarized intensity (cleaned). Contours are at 2, 4, 8, 16, 32, and $64 \times 0.2 \text{ mJy/beam}$. To be compared with Fig. A.29.

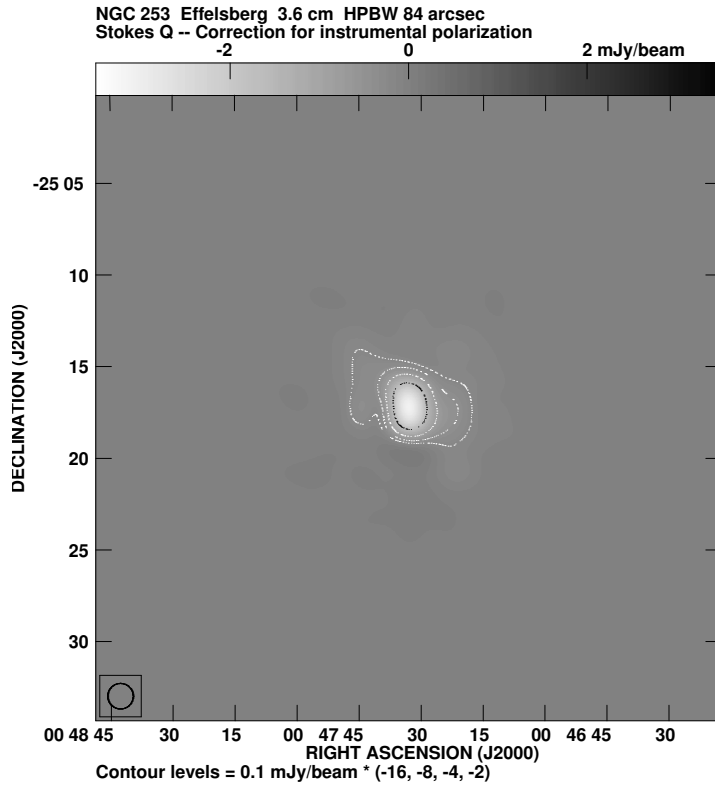


Figure A.31: *NGC 253 Effelsberg* $\lambda 3.6$ cm distribution of the instrumental correction in Stokes *Q*. Contours are at -32, -16, -8, -4, and -2×0.1 mJy/beam.

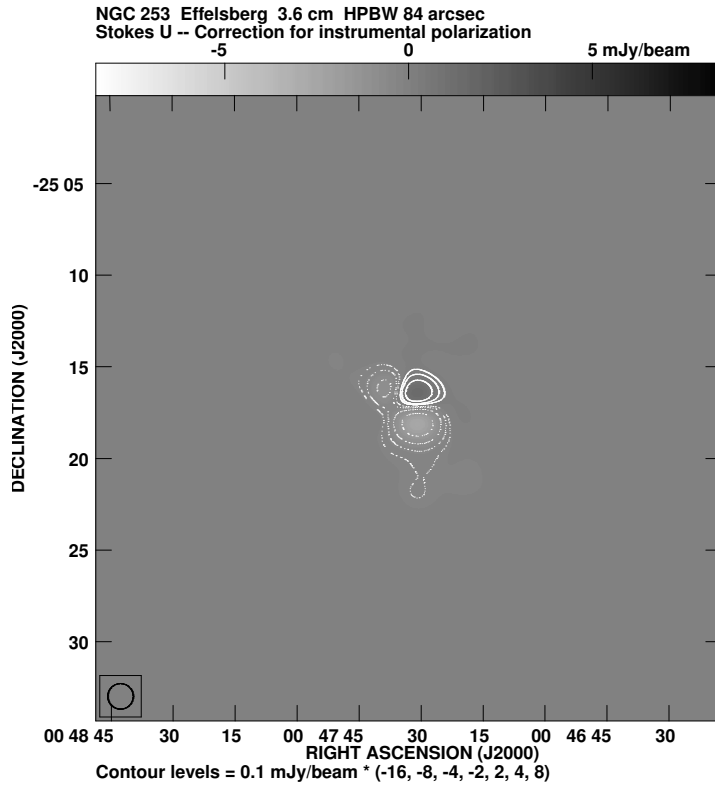


Figure A.32: *NGC 253 Effelsberg* $\lambda 3.6$ cm correction for the instrumental polarization in Stokes *U*. Contours are at -64, -32, -16, -8, -4, -2, 2, 4, and 8×0.1 mJy/beam.

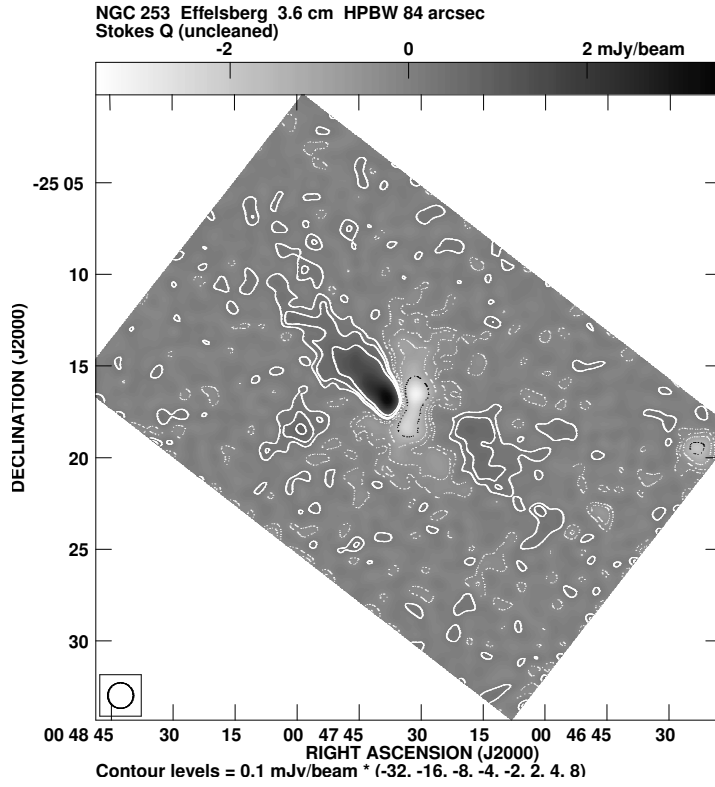


Figure A.33: NGC 253 Effelsberg $\lambda 3.6$ cm distribution of Stokes Q (uncleaned). Contours are at -32, -16, -8, -4, -2, 2, 4, 8, and 16×0.1 mJy/beam.

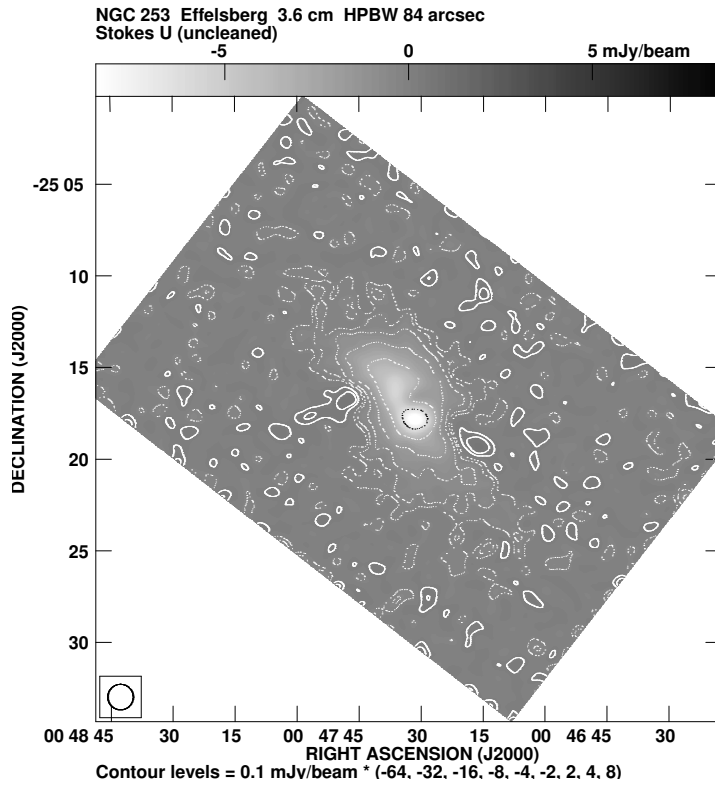


Figure A.34: NGC 253 Effelsberg $\lambda 3.6$ cm distribution of Stokes U (uncleaned). Contours are at -32, -16, -8, -4, -2, 2, 4, and 8×0.1 mJy/beam.

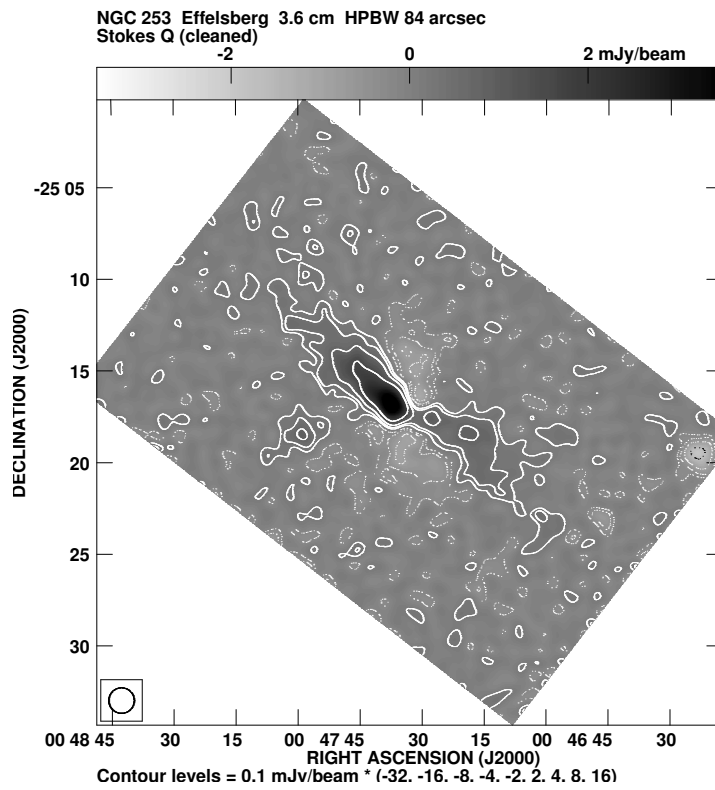


Figure A.35: NGC 253 Effelsberg $\lambda 3.6$ cm distribution of Stokes Q (cleaned). Contours are at -32, -16, -8, -4, -2, 2, 4, 8, and 16×0.1 mJy/beam. To be compared with Fig. A.33.

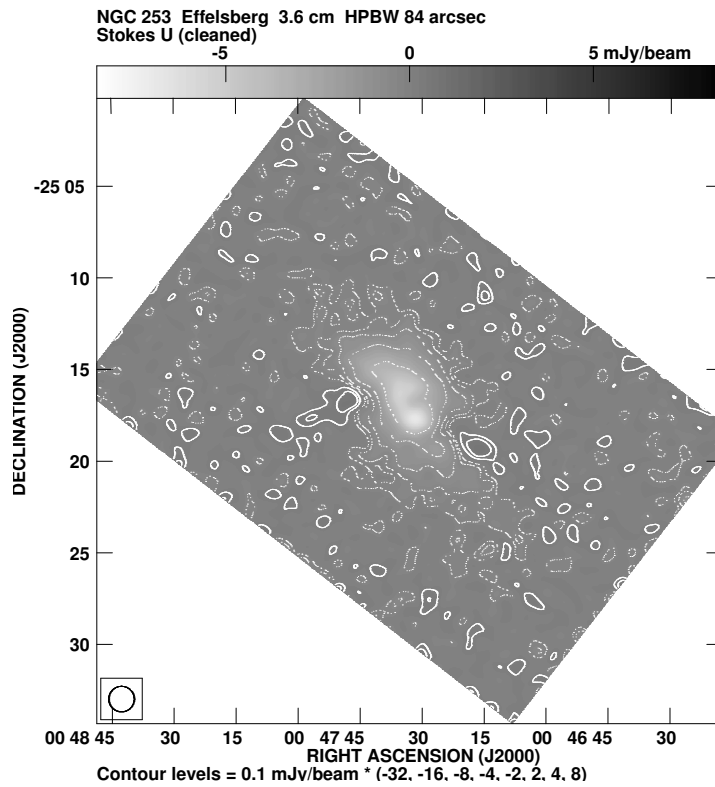


Figure A.36: NGC 253 Effelsberg $\lambda 3.6$ cm distribution of Stokes U (cleaned). Contours are at -32, -16, -8, -4, -2, 2, 4, and 8×0.1 mJy/beam. To be compared with Fig. A.34.

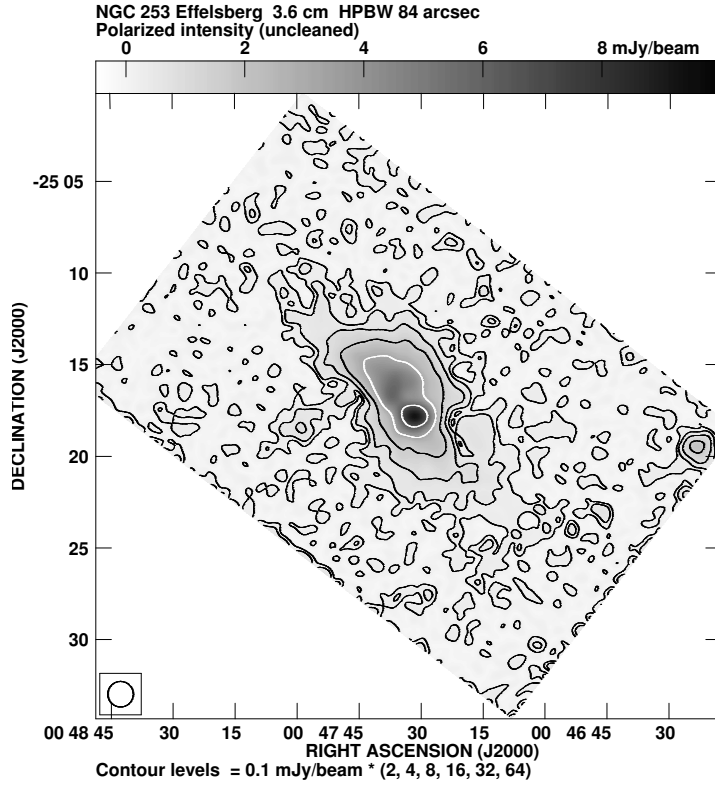


Figure A.37: NGC 253 Effelsberg $\lambda 3.6 \text{ cm}$ distribution of polarized intensity (uncleaned). Contours are at 2, 4, 8, 16, 32, and $64 \times 0.1 \text{ mJy/beam}$.

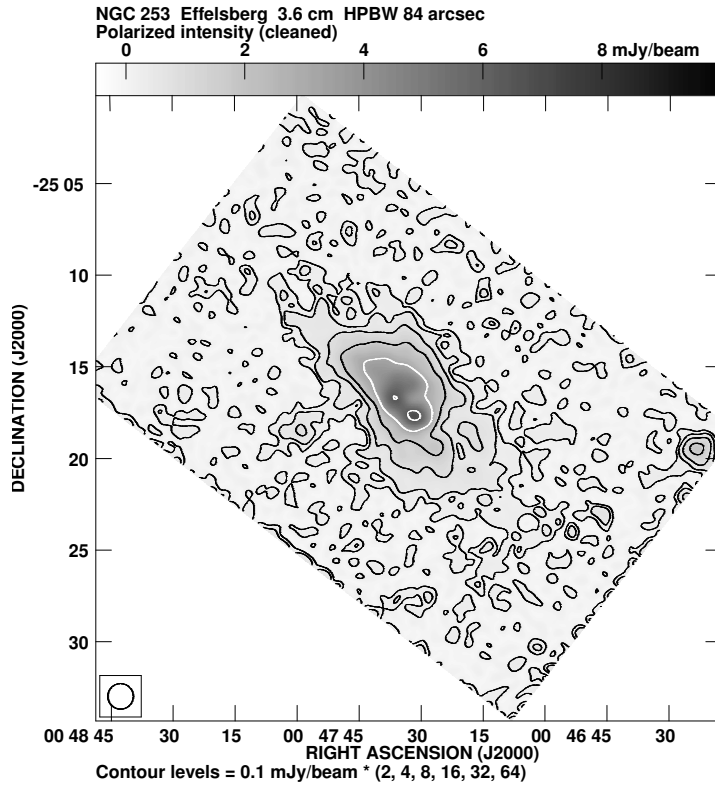


Figure A.38: NGC 253 Effelsberg $\lambda 3.6 \text{ cm}$ distribution of polarized intensity (cleaned). Contours are at 2, 4, 8, 16, 32, and $64 \times 0.1 \text{ mJy/beam}$. To be compared with Fig. A.37.

Appendix B

High dynamic range imaging with the Very Large Array (VLA)

B.1 The VLA mosaic

NGC 253 has an extension of 27.7 arcmin along the major axis. As the primary beam of the VLA antennas has only a size of 8 arcmin (HPBW) at $\lambda 6.2$ cm, we covered the galaxy by 15 pointings. The pointing centers were spaced by a distance of 5 arcmin and were placed on three rows parallel to the major axis each consisting of five pointings. This mosaic setup allows a nearly uniform sensitivity over the field of interest. I used self-calibration in 8 of the 15 pointings where the nuclear point-like source (thereafter simply called “nucleus”) is located within the primary beam. For the outer pointings the amplitude of the nucleus is not high enough to use self-calibration. The nucleus is ideally suited for the calibration phase. For this purpose I used only a few cleaning components and restricted the calibration on the outer part of the (u,v)-plane. The phase self-calibration was performed two times which showed sufficient convergence. This was followed by the calibration on phase and amplitude for which I used on the order of 1000 cleaning components. The self-calibration greatly suppresses the sidelobes caused by bright nucleus and thus ensured a sufficient high dynamic range. Our maps are essentially noise limited.

In order to recover all extended emission we used Effelsberg maps in order to fill up the missing zero-spacing flux. IMERG (part of AIPS) performs an addition of the VLA and the Effelsberg maps in the Fourier domain. The best results were obtained for a small overlap region between $0.4\text{ k}\lambda$ and $0.41\text{ k}\lambda$. The missing flux in the VLA map amounts to 10 % of the total flux and even 20 % of the flux of the extended flux measured with Effelsberg. This emphasizes the need of an independent measurement with a single-dish telescope when performing a mosaic with an interferometer.

B.2 Wide field polarization imaging

B.2.1 Standard polarization calibration with the VLA

The VLA antennas are equipped with detectors, the so-called feed horns, which measure the left-hand (Stokes L) and right-hand (Stokes R) circular polarization. The feed horns are no perfect receivers which measure exactly the circular components. There is also a correlation between the total power and the polarization. This is called the *instrumental polarization, leakage term, or D-term*. The measured polarization is the sum of the intrinsic polarization of the observed source and the instrumental polarization. The instrumental polarization can be disentangled observing that only the intrinsic polarization changes with the parallactic angle as the source moves over the sky when observing with an alt-azimuthal antenna

(as for the VLA). A good coverage of the observed parallactic angles is necessary to apply the polarization calibration with PCAL (part of AIPS) which can be accomplished by a 12 hour observation of the secondary (phase) calibrator if it is observed in regular time intervals throughout the observation. Eventually the absolute polarization angle has to be calibrated against a strong polarized source such as 3C286 with known polarization properties. This standard polarization calibration for the VLA works well but it is not suitable for wide field polarization imaging as the instrumental polarization is determined only for on-axis emission in the center of the primary beam.

The mosaic setup aims at a constant sensitivity over the field of view (FOV) which is optimized for a spacing between the pointings of one Half Power Beam Width (HPBW). Thus the nucleus of NGC 253 is located almost exactly on the edge of the primary beam for seven of out of 15 pointings, namely No. 4, 5, 6, 7, 9, 10, 11, and 12 (see Fig. B.1). This setup has severe consequences for the instrumental polarization since it amounts only to a fraction of 0.1 % for the center of VLA primary beam but it can be up to a few % at the primary beam edge. A further complication of the situation is the time variability of the instrumental polarization when the source moves around the center of the primary beam dependent on the parallactic angle. This reflects the dependency of the instrumental polarization on the location in the primary beam of the VLA. The cleaning of a time variable source can not be used in order to remove the sidelobes.

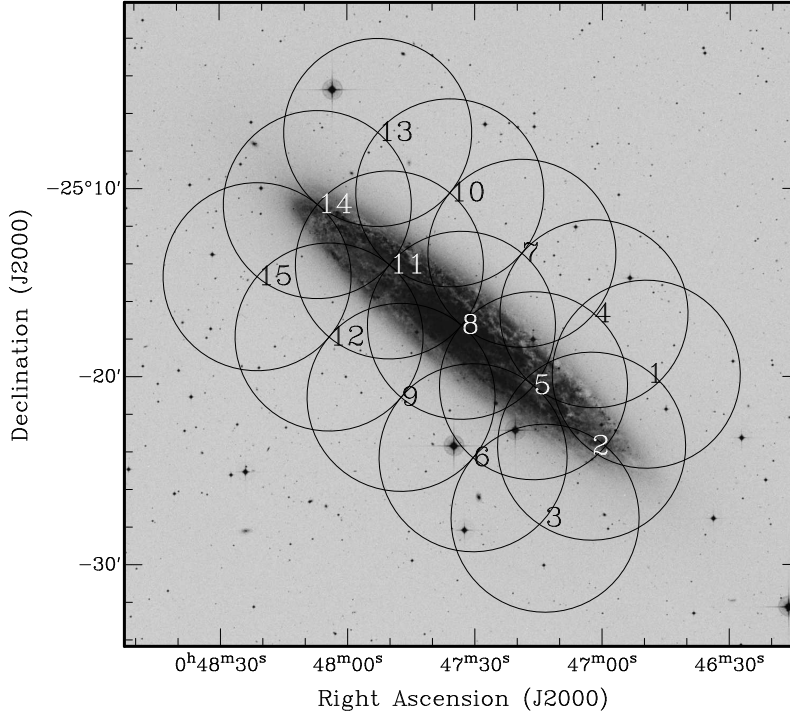


Figure B.1: *The VLA mosaic of NGC 253 at $\lambda 6.2$ cm consisting of 15 pointings. The circles indicate the HPBW of the VLA primary beam which is 8 arcmin at $\lambda 6.2$ cm. The background optical image has been obtained from the DSS.*

In Figs. B.2 and B.3 I present pointing No. 7 in Stokes Q and U , respectively, using the standard polarization calibration and successive cleaning. Clearly, the maps are heavily influenced by spurious polarization and are useless for any further consideration. In Figs. B.4 and B.5 I present the maps for the entire mosaic in Stokes Q and U , respectively.

B.2.2 Improved snapshot technique

The standard polarization technique is thus not suited to carry out the polarization mosaic of our measurements. In order to improve the quality of the polarization maps I first tried to remove the time variable

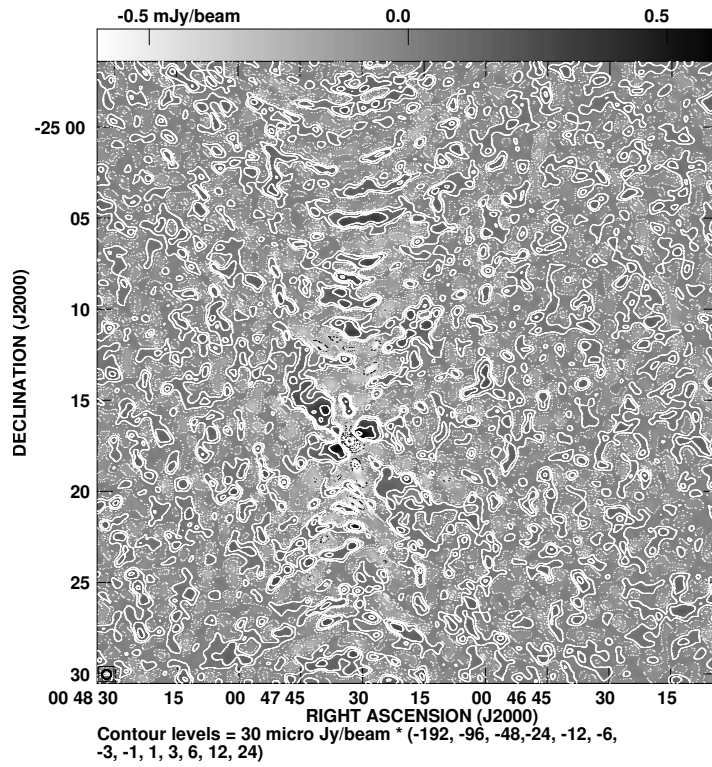


Figure B.2: *Stokes Q of Pointing No. 7. The standard polarization calibration on the secondary calibrator was used. Contours are at -192, -96, -48, -24, -12, -6, -3, -1, 1, 3, 6, 12, and $24 \times 30 \mu\text{Jy/beam}$.*

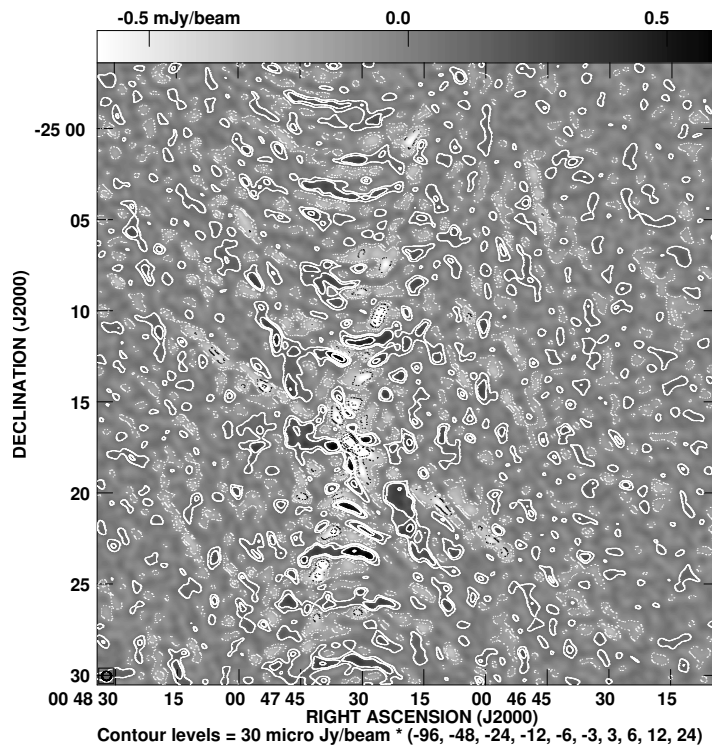


Figure B.3: *Stokes U of Pointing No. 7. The standard polarization calibration on the secondary calibrator was used. Contours are at -96, -48, -24, -12, -6, -3, 3, 6, 12, and $24 \times 30 \mu\text{Jy/beam}$.*

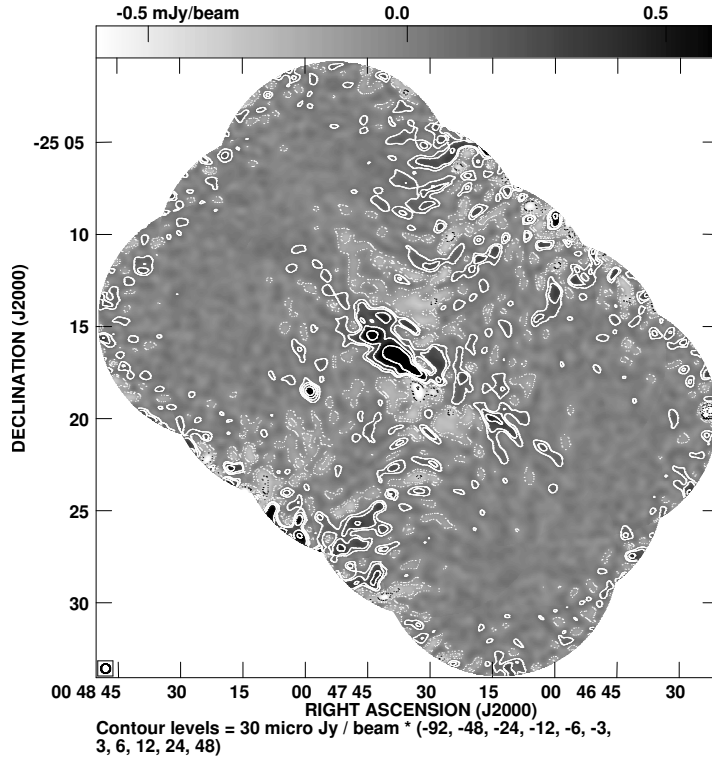


Figure B.4: NGC 253 VLA $\lambda 6.2$ cm Stokes Q . The standard polarization calibration on the secondary calibrator was used. Contours are at -92, -48, -24, -12, -6, -3, 3, 6, 12, 24, and $48 \times 30 \mu\text{Jy}/\text{beam}$.

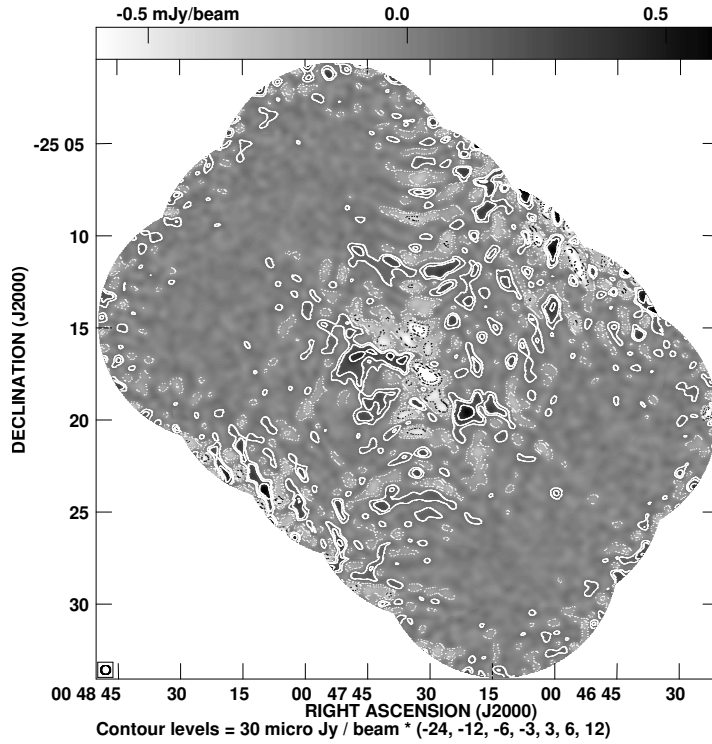


Figure B.5: NGC 253 VLA $\lambda 6.2$ cm Stokes U . The standard polarization calibration on the secondary calibrator was used. Contours are at -24, -12, -6, -3, 3, 6, and $12 \times 30 \mu\text{Jy}/\text{beam}$.

contribution of the instrumental polarization from the (u,v) -data. This can be done if we use only small time intervals – so-called “snapshots” – of the (u,v) -data. In our data set the integration time on each pointing is only 6 min which can be considered as a snapshot. In that short time span the variation of the parallactic angle is very small and hence the D-term is almost constant. The cleaning of the nucleus in each individual snapshot has the advantage of removing almost all sidelobes of the spurious polarization and replacing the nucleus with a Gaussian. In order to stack up the snapshot images they have to be convolved to an identical clean beam. The obvious disadvantage of that technique is that the snapshot with the lowest resolution, when the source rises or sets, limits the resolution of the final map. The snapshot technique has been described by Carilli & Holdaway (1992) for polarization observations at $\lambda 20$ cm with the VLA. It turned out that this technique can not be successfully applied to our observations since only point-like sources are well retained but the extended emission is almost not detected while the spurious polarization is well suppressed.

Hence, I developed an improvement to the snapshot technique observing that the crucial point for recovering all extended emission is to use the full set of the (u,v) -data for the inversion. It is worthwhile to note that the addition of (u,v) -data is not linear. It is a large difference between inverting each snapshot individually and then stacking the images together and taking all (u,v) -data and invert the (u,v) -data in one process. The conclusion is: in order to recover all extended emission it is most important to invert the (u,v) -data all together.

Hence, I removed the nucleus from the (u,v) -data in the individual snapshots before inverting all (u,v) -data. The amplitude of the nucleus in each snapshot was measured in Stokes Q and U , respectively. With a cleaning of the Stokes Q and U maps I replaced the nucleus with a Gaussian and thus determined the cleaning components of the nucleus in each snapshot. The cleaning components were subtracted using UVSUB (part of AIPS) from the (u,v) -snapshots. After that all (u,v) -snapshots were combined using DBCON (part of AIPS) before the inversion and successive cleaning with IMAGR. The use of all (u,v) -data all together with the time dependent contribution of the instrumental polarization subtracted improved the cleaning significantly and thus the sidelobes of the spurious polarization were suppressed as well. The noise-level caused by the spurious polarization was lowered roughly by a factor of three as can be seen in Figs. B.6 and B.7 for pointing No. 7 in Stokes Q and U , respectively. Figures B.8 and B.9 show the mosaic with this technique. Comparing with the maps presented above we see that the sidelobes of the spurious polarization are much better suppressed. Still, there are several arcs and rays visible centered on the nucleus. The noise level is still dominated by the spurious polarization and is higher than the theoretical expected noise level. Hence, this technique is an improvement to the standard polarization calibration but the maps are still not good enough to be useful for further consideration. The steps used for the improved snapshot technique are here briefly described:

1. The (u,v) -data of each observing run is calibrated with PCAL with the secondary (phase) calibrator.
2. The (u,v) -data is split in the snapshots of 6 minutes integration time for the seven pointings adjacent to the nuclear source.
3. The (u,v) -data is inverted and cleaned for each individual snapshot in Stokes Q and U , respectively. Thus for each snapshot the cleaning components of the nucleus in Stokes Q and U are obtained.
4. The cleaning components in Stokes Q and U of the nuclear point-like source are subtracted from the (u,v) -data in each individual snapshot using UVSUB.
5. The (u,v) -snapshots are combined using DBCON for Stokes Q and U , respectively. Hence, for each pointing we obtain a (u,v) -data set consisting of all (u,v) -snapshots for Stokes Q and U , respectively. These (u,v) -data sets are inverted and cleaned with IMAGR.

6. Thus a cleaned map with the nucleus subtracted is obtained in Stokes Q and U .

B.2.3 Off-axis polarization calibration

Even with the nucleus from the (u,v)-snapshots subtracted there is still a significant level of spurious polarization which dominates the noise level. The sidelobes are created as the polarization calibration is not known for the off-axis location of the nucleus. The cleaning replaces the nucleus with a Gaussian subtracting the dirty beam. Hence, the accuracy of the dirty beam limits the accuracy of the cleaning. The off-axis polarization calibration must thus be accurate as possible. The polarization calibration has to be performed for the off-axis location of the nucleus. For that purpose I applied PCAL on NGC 253 itself (instead on the secondary calibrator) including the nucleus. The calibration was done for each of the seven adjacent pointings and for each observing run. It turned out that I had to use the option “SOLTYPE=ORI” which applies a fit for feed ellipticity and orientation. It can be used in cases where the linear approximation breaks down (more than a few percent instrumental polarization). The spread of the polarization angle in the different baselines checked with the primary calibrator 3C48 was small enough (less than 5°). The polarization calibration on the nuclear point-like source was thus successfully applied. With the improved calibration for the off-axis location of the nucleus I was able to remove the nucleus almost completely from the (u,v)-data and any time variable contribution from the instrumental polarization was removed. I inverted all (u,v)-data together and formed the maps for the individual pointings. The pointing No. 7 is presented in Figs. B.10 and B.11 and the mosaic is presented in Figs. B.12 and B.13 in Stokes Q and U , respectively. The improvement is stunning compared with the maps presented before. The extended emission is now separated from the boundary caused by the beam attenuation. In the single pointing the extended polarized emission is well separated from the boundary. The arcs and rays centered on the nucleus have vanished. Now the maps are essentially noise limited with a noise level of $30 \mu\text{Jy}/\text{beam}$ at 30 arcsec HPBW. Here follows a brief explanation how I did perform the calibration:

1. The (u,v)-data of the individual pointing is calibrated with PCAL using “SOLTYPE=ORI”. For this I use all (u,v)-data together.
2. The (u,v)-data is split in the snapshots of 6 minutes integration time.
3. The snapshots are inverted and cleaned separately for Stokes Q and U . I clean only the nucleus because that is the only visible source in the snapshots which are well above the noise level. Also with this technique I obtain only the cleaning components of the nucleus.
4. The cleaning components are subtracted from the (u,v)-data in each snapshot using UVSUB for Stokes Q and U , respectively.
5. The (u,v)-snapshots are stacked together using DBCON for Stokes Q and U , respectively. The stacked (u,v)-data is inverted and cleaned with IMAGR again for Stokes Q and U , respectively.
6. All 15 pointings are convolved to an identical clean Gaussian beam using CONVOLV.
7. The mosaic is formed using LTESS which performs a linear superposition with a correction for the VLA primary beam attenuation using information from each pointing out to the 7 percent level of the primary beam (Braun 1988).

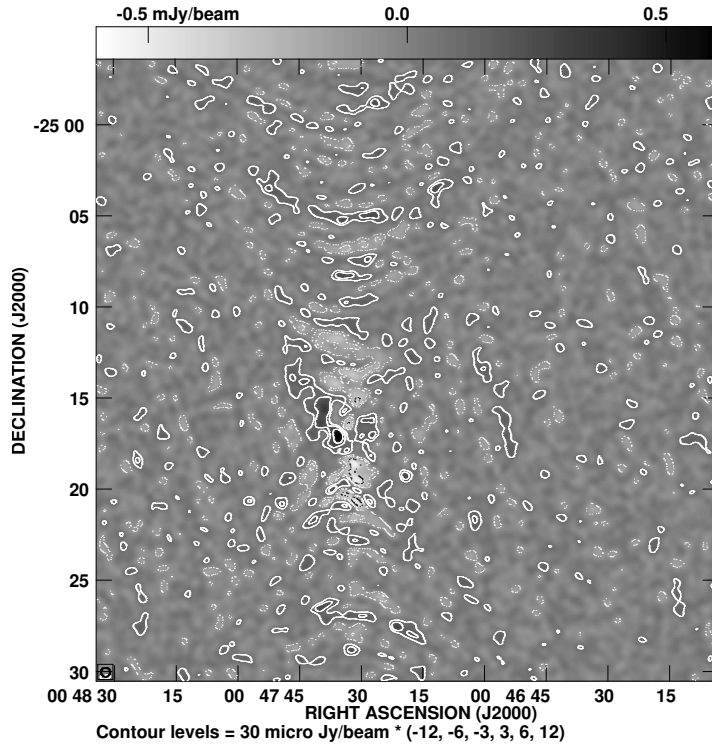


Figure B.6: *Pointing No. 7 in Stokes Q. The standard polarization calibration on the secondary calibrator was used. The nucleus has been subtracted from the (u,v)-data in each snapshot. Contours are at -12, -6, -3, 3, 6, and $12 \times 30 \mu\text{Jy/beam}$.*

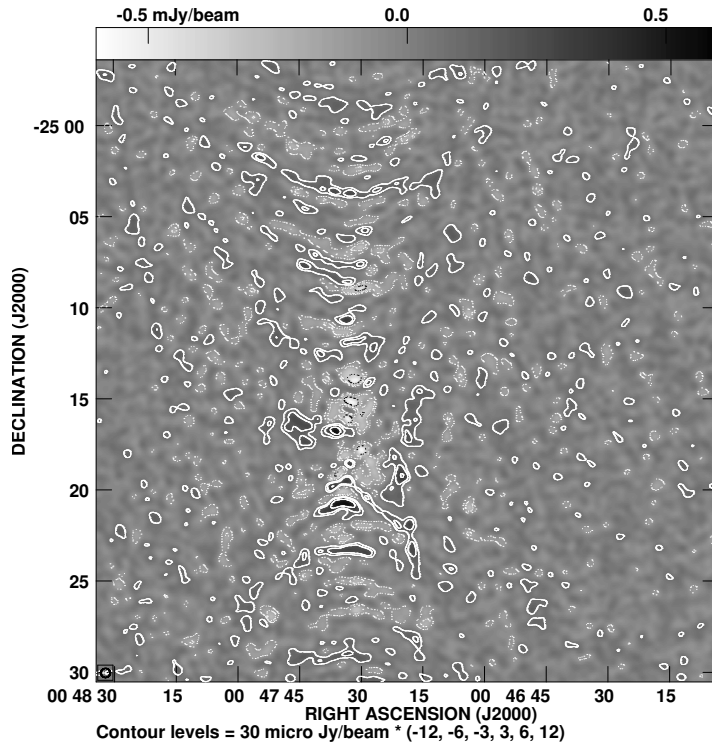


Figure B.7: *Pointing No. 7 in Stokes U. The standard polarization calibration on the secondary calibrator was used. The nucleus has been subtracted from the (u,v)-data in each snapshot. Contours are at -12, -6, -3, 3, 6, and $12 \times 30 \mu\text{Jy/beam}$.*

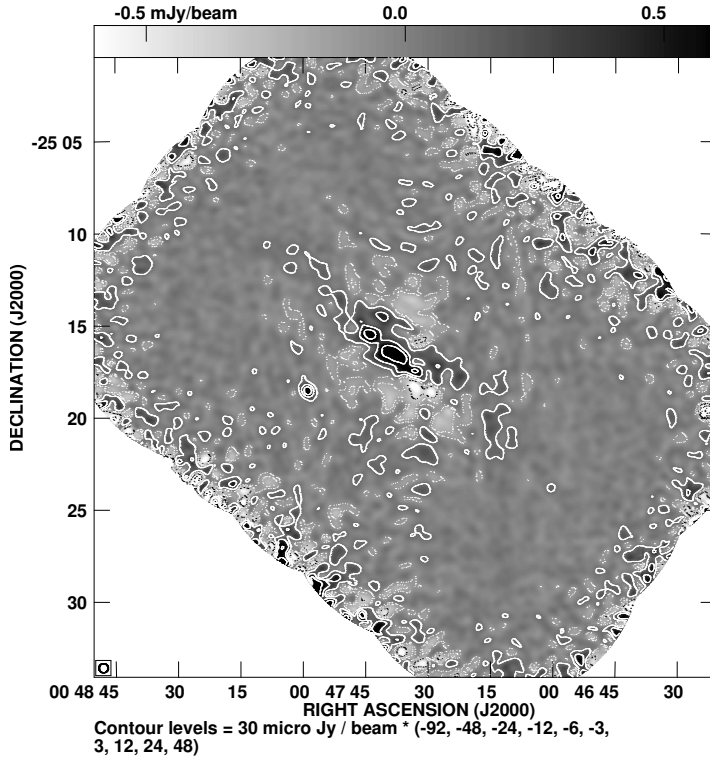


Figure B.8: NGC 253 VLA $\lambda 6.2$ cm Stokes Q. The standard polarization calibration on the secondary calibrator was used. The nucleus has been subtracted from the (u,v)-data in each snapshot. Contours are at -92, -48, -24, -12, -6, -3, 3, 6, 12, 24, and $48 \times 30 \mu\text{Jy}/\text{beam}$.

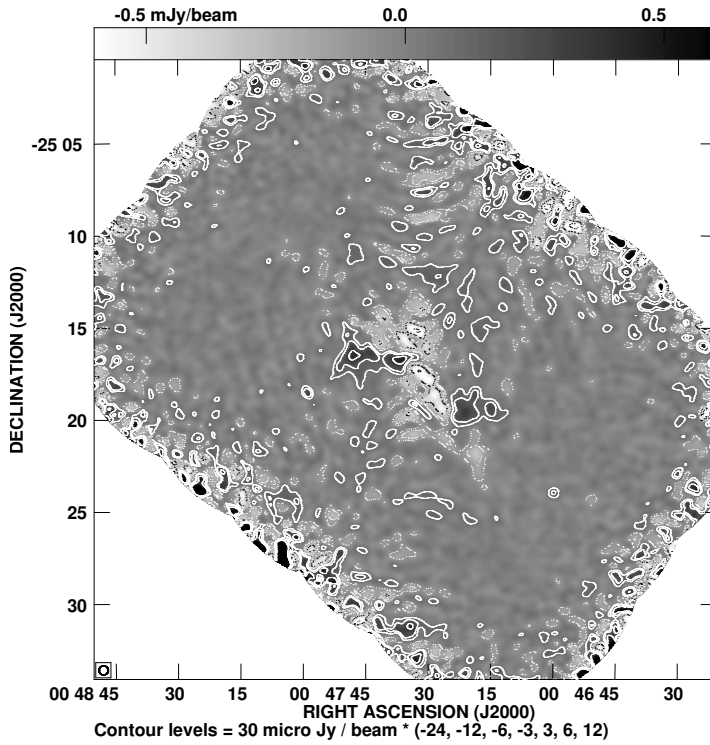


Figure B.9: NGC 253 VLA $\lambda 6.2$ cm Stokes U. The standard polarization calibration on the secondary calibrator was used. The nucleus has been subtracted from the (u,v)-data in each snapshot. Contours are at -24, -12, -6, -3, 3, 6, and $12 \times 30 \mu\text{Jy}/\text{beam}$.

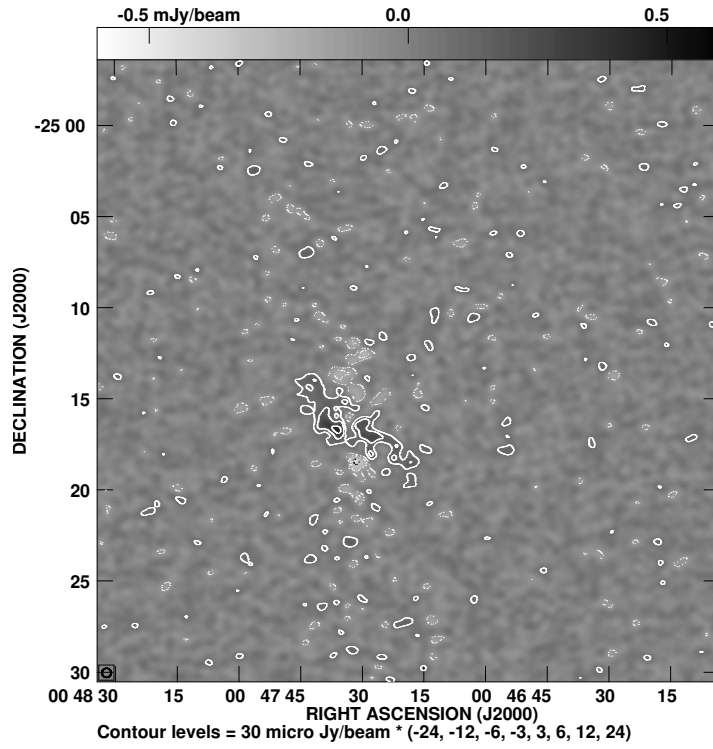


Figure B.10: *Stokes Q* of pointing No. 7. The polarization calibration on the nucleus itself was used. The nucleus has been subtracted from the (u,v) -data in each snapshot. Contours are at $-24, -12, -6, -3, 3, 6, 12$, and $24 \times 30 \mu\text{Jy/beam}$.

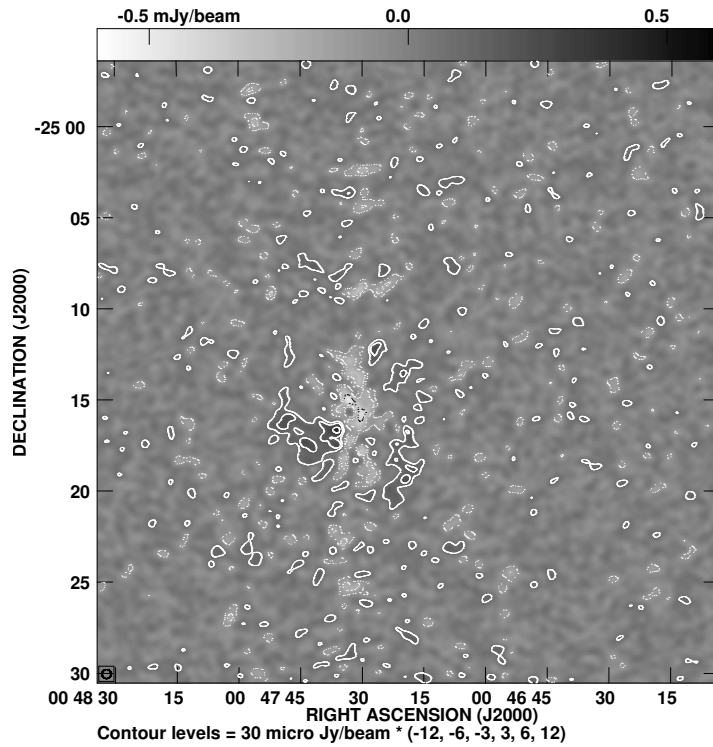


Figure B.11: *Stokes U* of pointing No. 7. The polarization calibration on the nucleus itself was used. The nucleus has been subtracted from the (u,v) -data in each snapshot. Contours are at $-12, -6, -3, 3, 6$, and $12 \times 30 \mu\text{Jy/beam}$.

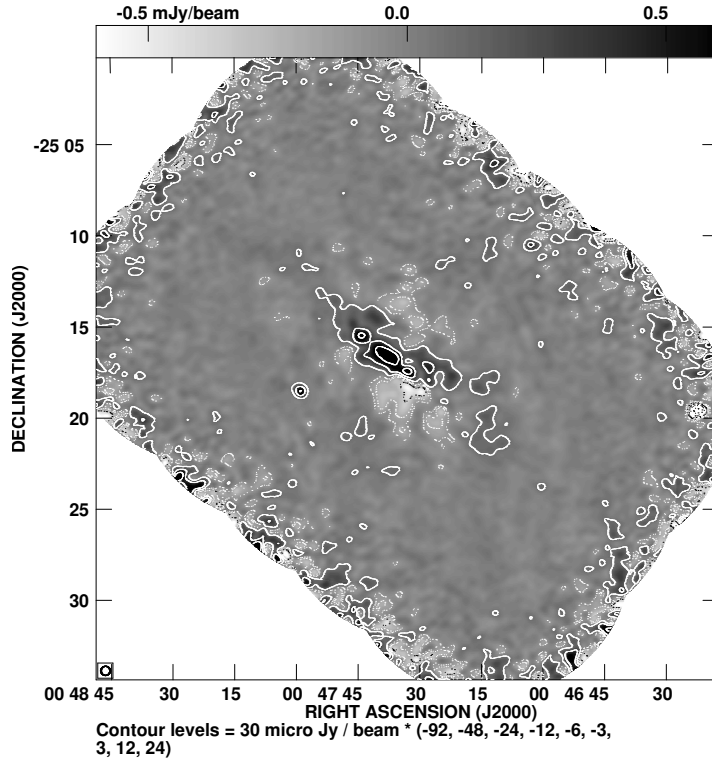


Figure B.12: *NGC 253 VLA $\lambda 6.2$ cm Stokes Q.* The polarization calibration on the nucleus itself was used. The nucleus has been subtracted from the (u,v) -data in each snapshot. Contours are at -92, -48, -24, -12, -6, -3, 3, 6, 12, and $24 \times 30 \mu\text{Jy/beam}$.

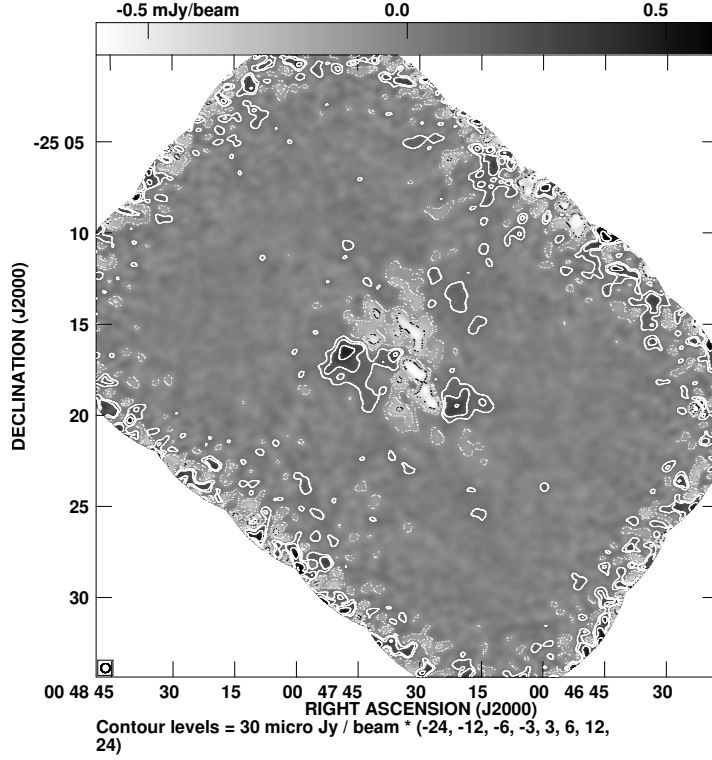


Figure B.13: *NGC 253 VLA $\lambda 6.2$ cm Stokes U.* The polarization calibration on the nucleus itself was used. The nucleus has been subtracted from the (u,v) -data in each snapshot. Contours are at -24, -12, -6, -3, 3, 6, 12, and $24 \times 30 \mu\text{Jy/beam}$.

B.2.4 Comparison with the Effelsberg polarization maps

The comparison with the Effelsberg polarization maps is important in order to check the reliability of the polarization calibration. For this purpose I convolved the VLA Stokes Q and U mosaic with the Effelsberg beam of 144 arcsec (HPBW). These maps are presented in Figs. B.14 and B.15. They have to be compared with the maps presented in Appendix A. There is a good correlation between the two completely independent measurements.

For the final maps I have combined the VLA mosaic with the Effelsberg maps as described in the section B.1. Thus, I was able to recover all extended emission which is distributed on such large angular scales that the missing zero-spacing flux of the VLA plays a significant role. The flux integration of the polarized intensity gave a total polarized flux of 0.0796 Jy for the combined VLA and Effelsberg map and 0.0635 Jy for the VLA map alone. Thus the Effelsberg adds 25 % of polarized flux to the VLA map which is significant.

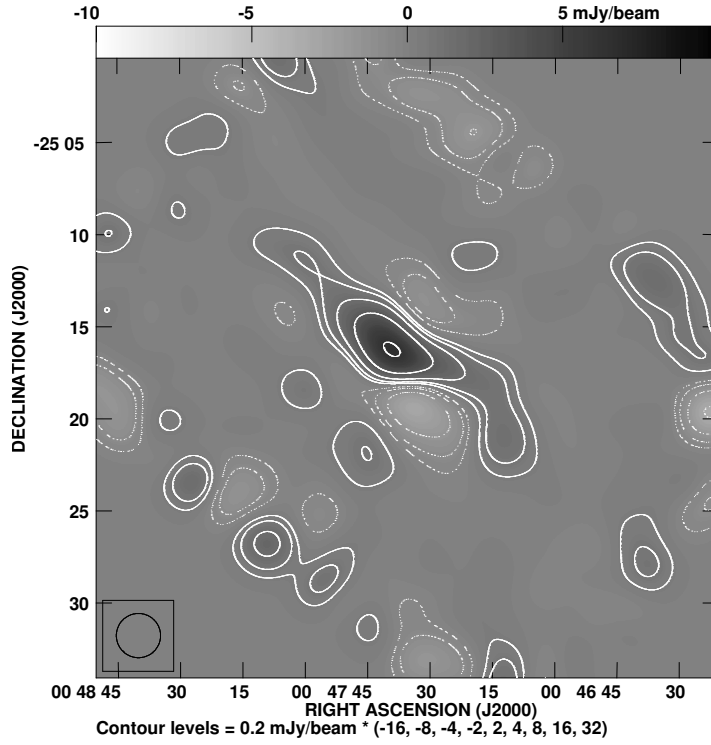


Figure B.14: NGC 253 VLA $\lambda 6.2$ cm Stokes Q convolved to 144 arcsec HPBW. Contours are at -16, -8, -4, -2, 2, 4, 8, 16, and $32 \times 200 \mu\text{Jy/beam}$. To be compared with Fig. A.27.

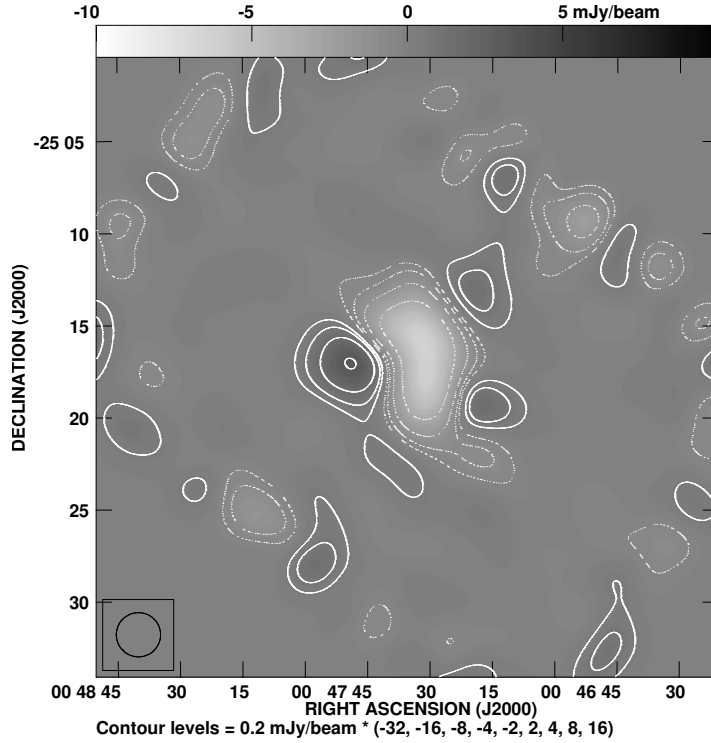


Figure B.15: NGC 253 VLA $\lambda 6.2$ cm Stokes U convolved to 144 arcsec HPBW. Contours are at -32, -16, -8, -4, -2, 2, 4, 8, and $16 \times 200 \mu\text{Jy/beam}$. To be compared with Fig. A.28.

Appendix C

Color figures

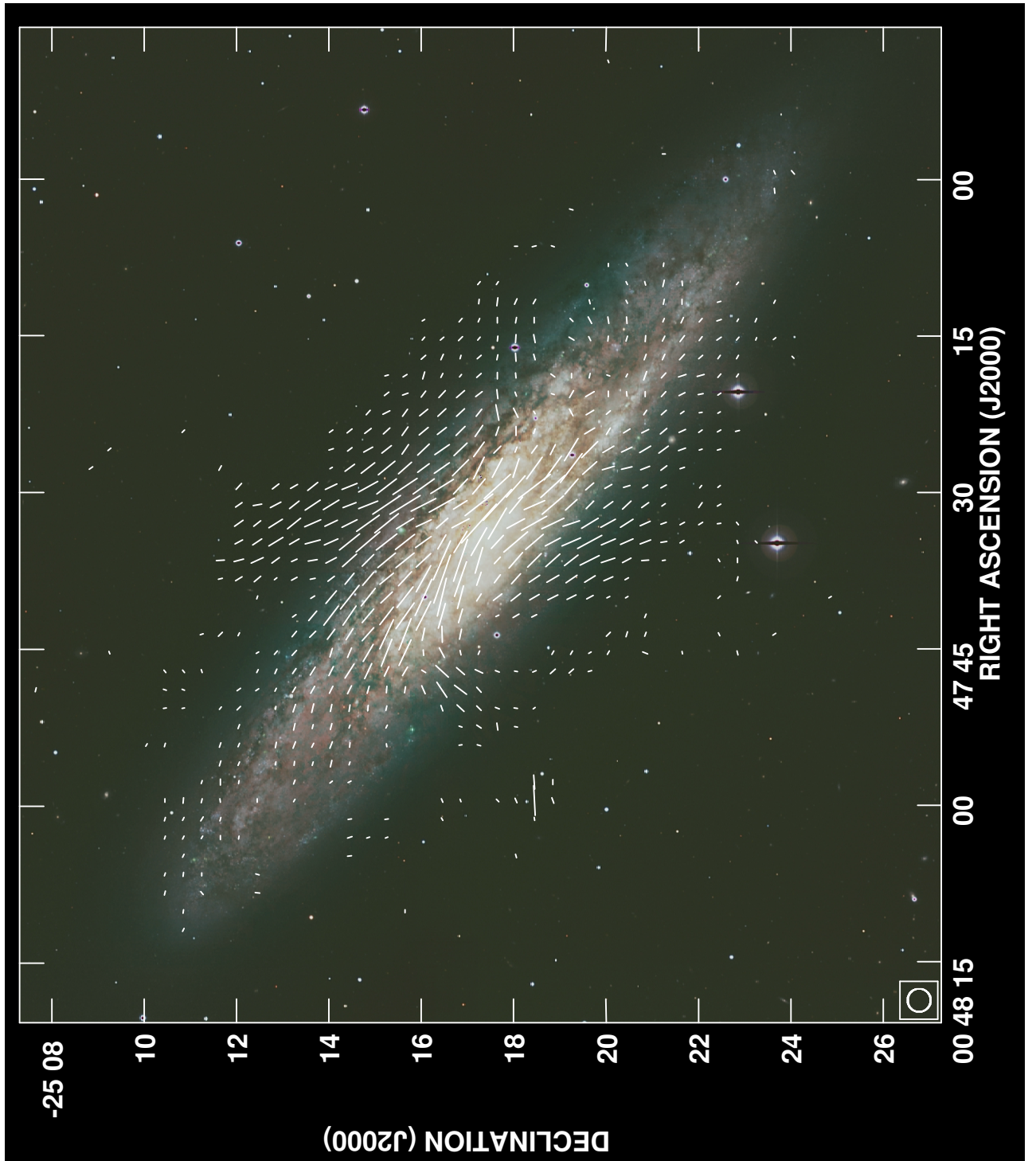


Figure C.1: NGC 253 VLA + Effelsberg $\lambda 6.2$ cm orientation of the intrinsic regular magnetic field with $30''$ resolution. The length of the vectors is defined by $1''$ to be equivalent to $16.7 \mu\text{Jy}/\text{beam}$ of polarized intensity. The optical image has been provided by Schmithüsen & Burggraf (2007).

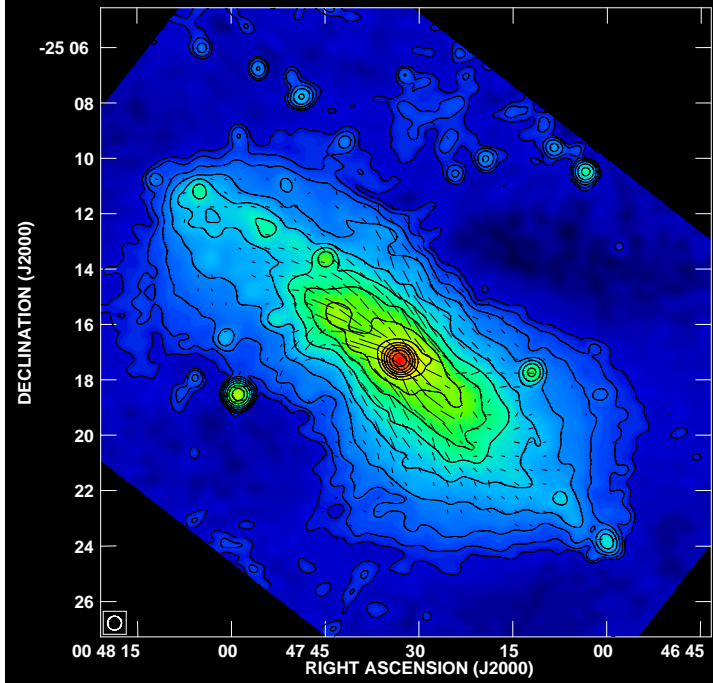


Figure C.2: *The total power radio continuum obtained from the combined VLA + Effelsberg observations at $\lambda 6.2$ cm. Contours are at 3, 6, 12, 24, 48, 96, 192, 384, 768, 1536, 3077, 6144, 12288, and $24576 \times 30 \mu\text{Jy/beam}$. The overlaid vectors indicate the orientation of the intrinsic regular magnetic field. The length of the vectors is defined by $1''$ to be equivalent to $12.5 \mu\text{Jy/beam}$ of polarized intensity.*

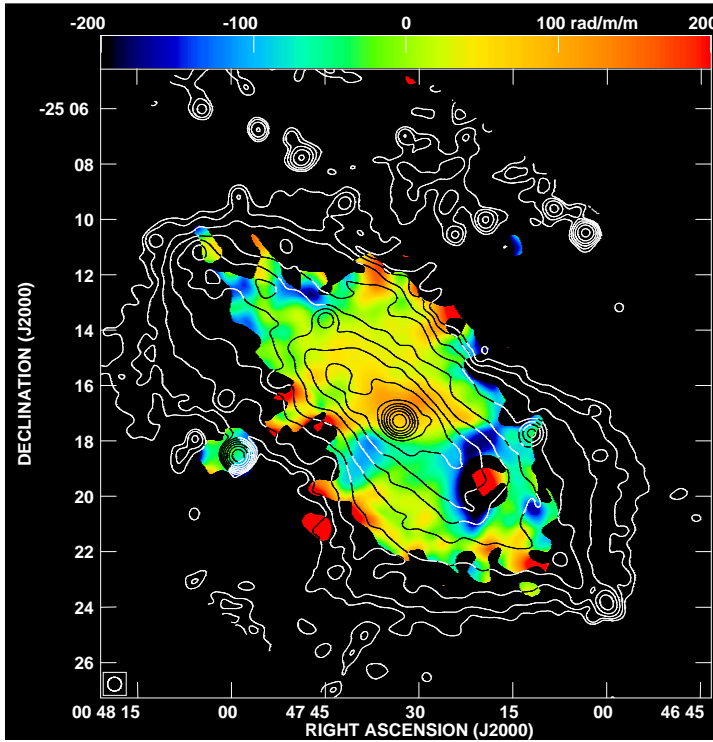


Figure C.3: *Distribution of the Rotation Measure between $\lambda 6.2$ cm (VLA + Effelsberg) and $\lambda 3.6$ cm (Effelsberg) and total power radio continuum obtained from the combined VLA + Effelsberg observations at $\lambda 6.2$ cm. The overlaid contours are identical to Fig. C.2.*

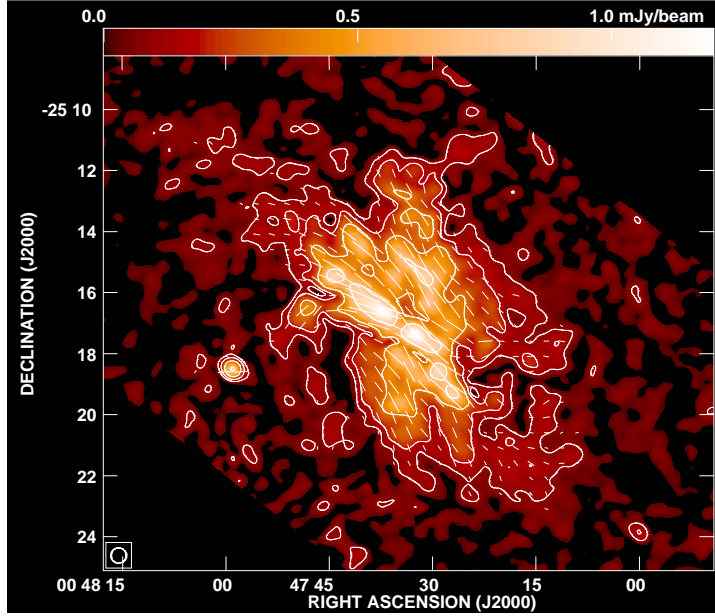


Figure C.4: *The polarized intensity obtained from the combined VLA and Effelsberg observations at $\lambda 6.2$ cm. Contours are at 3, 6, 12, and $24 \times 30 \mu\text{Jy/beam}$. The overlaid vectors indicate the orientation of the intrinsic regular magnetic field. The length of the vectors is defined by 1 arcsec to be equivalent to $12.5 \mu\text{Jy/beam}$ polarized intensity.*

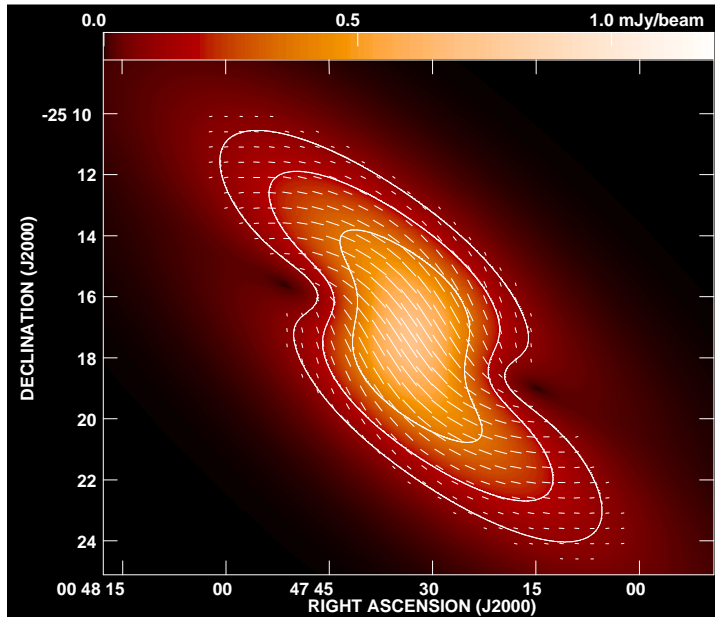


Figure C.5: *Model for the axisymmetric spiral magnetic field with a pitch angle of 25° . Contours and vectors are identical as in Fig. C.4.*

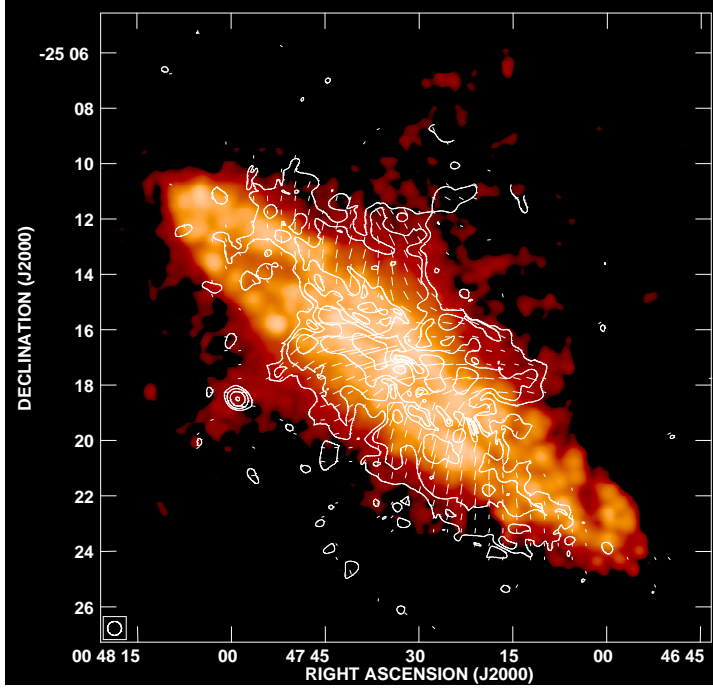


Figure C.6: *Poloidal magnetic field with $H\alpha$ emission. Contours and vectors are identical to Fig. C.5.*

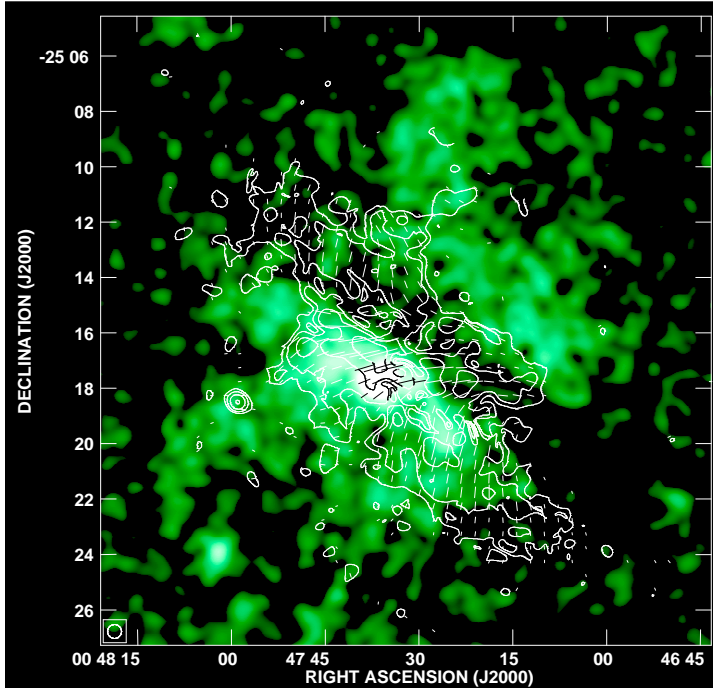


Figure C.7: *Poloidal magnetic field with soft X-ray emission. Contours and vectors are identical to Fig. C.5.*

Bibliography

- Baars, J. W. M., Genzel, R., Pauliny-Toth, I. I. K., & Witzel, A. 1977, A&A, 61, 99
- Balbus, S. A. & Hawley, J. F. 1991, ApJ, 376, 214
- Beck, R. 2000, in Royal Society of London Philosophical Transactions Series A, Vol. 358, Astronomy, physics and chemistry of H_3^+ , 777
- Beck, R., Brandenburg, A., Moss, D., Shukurov, A., & Sokoloff, D. 1996, ARA&A, 34, 155
- Beck, R. & Gaensler, B. M. 2004, New Astronomy Review, 48, 1289
- Boomsma, R., Oosterloo, T., Fraternali, F., van der Hulst J.M., & Sancisi, R. 2005, A&A, 431, 65
- Borgani, S., Finoguenov, A., Kay, S. T., et al. 2005, MNRAS, 361, 233
- Brandenburg, A., Nordlund, A., Stein, R. F., & Torkelsson, U. 1995, ApJ, 446, 741
- Braun, R. 1988, Millimeter Array Memo., 46
- Breitschwerdt, D., McKenzie, J. F., & Voelk, H. J. 1991, A&A, 245, 79
- Carilli, C. L. & Holdaway, M. A. 1992, VLA Test Memo, 163, 1
- Carilli, C. L., Holdaway, M. A., Ho, P. T. P., & de Pree, C. G. 1992, ApJ, 399, L59
- Cline, K. S., Brummell, N. H., & Cattaneo, F. 2003, ApJ, 599, 1449
- Coles, P. 2005, Nature, 433, 248
- Dahlem, M., Lazendic, J. S., Haynes, R. F., Ehle, M., & Lisenfeld, U. 2001, A&A, 374, 42
- Dahlem, M., Lisenfeld, U., & Golla, G. 1995, ApJ, 444, 119
- Dahlem, M., Lisenfeld, U., & Rossa, J. 2006, A&A, 457, 121
- de Blok, W. J. G. & Bosma, A. 2002, A&A, 385, 816
- Dettmar, R.-J. & Soida, M. 2006, AN, 327, 495
- Emerson, D. T. & Gräve, R. 1988, A&A, 190, 353
- Gaensler, B. M., Beck, R., & Feretti, L. 2004, New Astronomy Review, 48, 1003
- Harnett, J. I. & Reynolds, J. E. 1985, MNRAS, 215, 247

- Haslam, C. G. T. 1974, *A&AS*, 15, 333
- Högbom, J. A. 1974, *A&AS*, 15, 417
- Hoopes, C. G., Heckman, T. M., Strickland, D. K., & Howk, J. C. 2003, *ApJ*, 596, L175
- Hoopes, C. G., Walterbos, R. A. M., & Greenwalt, B. E. 1996, *AJ*, 112, 1429
- Ipavich, F. M. 1975, *ApJ*, 196, 107
- Klein, U. 1978, Diploma thesis, Friedrichs-Wilhelms-Universität, Bonn, Germany
- Klein, U. & Mack, K.-H. 1995, in *Astronomical Society of the Pacific Conference Series*, Vol. 75, *Multi-Feed Systems for Radio Telescopes*, ed. D. T. Emerson & J. M. Payne, 318
- Krause, M. 2004, in *The Magnetized Interstellar Medium*, ed. B. Uyaniker, W. Reich, & R. Wielebinski, 173
- Krause, M. 2007, *Memorie della Societa Astronomica Italiana*, 78, 314
- Kulsrud, R. & Pearce, W. P. 1969, *ApJ*, 156, 445
- Mack, K.-H. 2005, priv. comm.
- Mashchenko, S., Couchman, H. M. P., & Wadsley, J. 2006, *Nature*, 442, 539
- Moore, B., Ghigna, S., Governato, F., et al. 1999, *ApJ*, 524, L19
- Navarro, J. F., Frenk, C. S., & White, S. D. M. 1996, *ApJ*, 462, 563
- Parker, E. N. 1966, *ApJ*, 145, 811
- Pence, W. D. 1981, *ApJ*, 247, 473
- Pietsch, W., Vogler, A., Klein, U., & Zinnecker, H. 2000, *A&A*, 360, 24
- Ponman, T. J., Cannon, D. B., & Navarro, J. F. 1999, *Nature*, 397, 135
- Rohlfs, K. & Wilson, T. 2004, *Tools of radioastronomy* (Berlin, Germany: Springer)
- Rosen, A. & Bregman, J. N. 1995, *ApJ*, 440, 634
- Rossa, J. & Dettmar, R.-J. 2000, *A&A*, 359, 433
- Rottmann, H. 1996, PhD thesis, Friedrichs-Wilhelms-Universität, Bonn, Germany
- Schmithüsen, O. & Burggraf, B. 2007, priv. comm.
- Soida, M. 2005, in *The Magnetized Plasma in Galaxy Evolution*, ed. K. T. Chyzy, K. Otmianowska-Mazur, M. Soida, & R.-J. Dettmar, 185–190
- Spergel, D. N., Bean, R., Doré, O., et al. 2007, *ApJS*, 170, 377
- Spergel, D. N., Verde, L., Peiris, H. V., et al. 2003, *ApJS*, 148, 175
- Strickland, D. K., Heckman, T. M., Weaver, K. A., Hoopes, C. G., & Dahlem, M. 2002, *ApJ*, 568, 689

- Teerikorpi, P., Bottinelli, L., Gouguenheim, L., & Paturel, G. 1992, *A&A*, 260, 17
- Tüllmann, R., Pietsch, W., Rossa, J., Breitschwerdt, D., & Dettmar, R.-J. 2006, *A&A*, 448, 43
- Veilleux, S. & Rupke, D. S. 2004, *Publications of the Astronomical Society of Australia*, 21, 393
- Younger, J. D., Cox, T. J., Seth, A. C., & Hernquist, L. 2007, *ApJ*, 670, 269
- Zirakashvili, V. N., Breitschwerdt, D., Ptuskin, V. S., & Voelk, H. J. 1996, *A&A*, 311, 113

List of Figures

| | | |
|------|---|----|
| 1.1 | Cartoon of the halo structure of NGC 253 (I) | 4 |
| 4.1 | Cartoon of the halo structure of NGC 253 (II) | 37 |
| 4.2 | NGC 4634 VLA $\lambda 6.2$ cm total power and B-vectors | 39 |
| 4.3 | NGC 4634 VLA $\lambda 6.2$ cm polarized intensity and B-vectors | 39 |
| 4.4 | NGC 7090 ATCA $\lambda 6$ cm total power and B-vectors | 40 |
| 4.5 | NGC 7090 ATCA $\lambda 6$ cm polarized intensity and B-vectors | 40 |
| 4.6 | NGC 7462 ATCA $\lambda 6$ cm total power and B-vectors | 41 |
| 4.7 | NGC 7462 ATCA $\lambda 6$ cm polarized intensity and B-vectors | 41 |
| A.1 | Effelsberg secondary focus cabin (SFK) | 46 |
| A.2 | Scanning procedure of the Effelsberg maps | 47 |
| A.3 | 3C84 Effelsberg $\lambda 6.2$ cm total power at 55° elevation | 50 |
| A.4 | 3C84 Effelsberg $\lambda 6.2$ cm total power at 40° elevation | 50 |
| A.5 | 3C84 Effelsberg $\lambda 6.2$ cm total power at 20° elevation | 51 |
| A.6 | 0237-23 Effelsberg $\lambda 6.2$ cm total power at 20° elevation | 51 |
| A.7 | 3C84 Effelsberg $\lambda 3.6$ cm total power at 40° elevation | 52 |
| A.8 | 3C84 Effelsberg $\lambda 3.6$ cm total power at 20° elevation | 52 |
| A.9 | 3C84 Effelsberg $\lambda 6.2$ cm Stokes Q at 20° elevation | 53 |
| A.10 | 3C84 Effelsberg $\lambda 6.2$ cm Stokes U at 20° elevation | 53 |
| A.11 | 3C84 Effelsberg $\lambda 3.6$ cm Stokes Q at 20° elevation | 54 |
| A.12 | 3C84 Effelsberg $\lambda 3.6$ cm Stokes U at 20° elevation | 54 |
| A.13 | NGC 253 parallactic angle as function of the hour angle | 55 |
| A.14 | NGC 253 Effelsberg $\lambda 3.6$ cm PRESSE structures | 56 |
| A.15 | NGC 253 Effelsberg $\lambda 6.2$ cm total power (uncleaned) | 58 |
| A.16 | NGC 253 Effelsberg $\lambda 6.2$ cm total power (cleaned) | 58 |
| A.17 | NGC 253 Effelsberg $\lambda 3.6$ cm total power (uncleaned) | 59 |
| A.18 | NGC 253 Effelsberg $\lambda 3.6$ cm total power (cleaned) | 59 |
| A.19 | NGC 253 Effelsberg $\lambda 6.2$ cm cleaning structures | 60 |
| A.20 | NGC 253 Effelsberg $\lambda 3.6$ cm cleaning structures | 60 |
| A.21 | Transformation of Stokes Q and U | 61 |
| A.22 | Block diagram of the single-dish cleaning of NGC 253 | 61 |
| A.23 | NGC 253 Effelsberg $\lambda 6.2$ cm Stokes Q instrumental correction | 63 |
| A.24 | NGC 253 Effelsberg $\lambda 6.2$ cm Stokes U instrumental correction | 63 |
| A.25 | NGC 253 Effelsberg $\lambda 6.2$ cm Stokes Q (uncleaned) | 64 |
| A.26 | NGC 253 Effelsberg $\lambda 6.2$ cm Stokes U (uncleaned) | 64 |
| A.27 | NGC 253 Effelsberg $\lambda 6.2$ cm Stokes Q (cleaned) | 65 |

| | |
|---|----|
| A.28 NGC 253 Effelsberg $\lambda 6.2$ cm Stokes U (cleaned) | 65 |
| A.29 NGC 253 Effelsberg $\lambda 6.2$ cm polarized intensity (uncleaned) | 66 |
| A.30 NGC 253 Effelsberg $\lambda 6.2$ cm polarized intensity (cleaned) | 66 |
| A.31 NGC 253 Effelsberg $\lambda 3.6$ cm Stokes Q instrumental correction | 67 |
| A.32 NGC 253 Effelsberg $\lambda 3.6$ cm Stokes U instrumental correction | 67 |
| A.33 NGC 253 Effelsberg $\lambda 3.6$ cm Stokes Q (uncleaned) | 68 |
| A.34 NGC 253 Effelsberg $\lambda 3.6$ cm Stokes U (uncleaned) | 68 |
| A.35 NGC 253 Effelsberg $\lambda 3.6$ cm Stokes Q (cleaned) | 69 |
| A.36 NGC 253 Effelsberg $\lambda 3.6$ cm Stokes U (cleaned) | 69 |
| A.37 NGC 253 Effelsberg $\lambda 3.6$ cm polarized intensity (uncleaned) | 70 |
| A.38 NGC 253 Effelsberg $\lambda 3.6$ cm polarized intensity (cleaned) | 70 |
| | |
| B.1 The VLA mosaic at $\lambda 6.2$ cm of NGC 253 | 72 |
| B.2 NGC 253 VLA $\lambda 6.2$ cm pointing No. 7 Stokes Q (I) | 73 |
| B.3 NGC 253 VLA $\lambda 6.2$ cm pointing No. 7 Stokes U (I) | 73 |
| B.4 NGC 253 VLA $\lambda 6.2$ cm Stokes Q (I) | 74 |
| B.5 NGC 253 VLA $\lambda 6.2$ cm Stokes U (I) | 74 |
| B.6 NGC 253 VLA $\lambda 6.2$ cm pointing No. 7 Stokes Q (II) | 77 |
| B.7 NGC 253 VLA $\lambda 6.2$ cm pointing No. 7 Stokes U (II) | 77 |
| B.8 NGC 253 VLA $\lambda 6.2$ cm Stokes Q (II) | 78 |
| B.9 NGC 253 VLA $\lambda 6.2$ cm Stokes U (II) | 78 |
| B.10 NGC 253 VLA $\lambda 6.2$ cm pointing No. 7 Stokes Q (III) | 79 |
| B.11 NGC 253 VLA $\lambda 6.2$ cm pointing No. 7 Stokes U (III) | 79 |
| B.12 NGC 253 VLA $\lambda 6.2$ cm Stokes Q (III) | 80 |
| B.13 NGC 253 VLA $\lambda 6.2$ cm Stokes U (III) | 80 |
| B.14 NGC 253 VLA $\lambda 6.2$ cm Stokes Q ($HPBW = 144$ arcsec) | 82 |
| B.15 NGC 253 VLA $\lambda 6.2$ cm Stokes U ($HPBW = 144$ arcsec) | 82 |
| | |
| C.1 NGC 253 VLA $\lambda 6.2$ cm magnetic field orientation | 84 |
| C.2 NGC 253 VLA + Effelsberg total power radio continuum at $\lambda 6.2$ cm | 85 |
| C.3 NGC 253 VLA + Effelsberg Rotation Measure between $\lambda 6.2$ cm and 3.6 cm | 85 |
| C.4 NGC 253 VLA + Effelsberg polarized emission and B-vectors at $\lambda 6.2$ cm | 86 |
| C.5 NGC 253 axisymmetric spiral magnetic field model | 86 |
| C.6 NGC 253 poloidal magnetic field with $H\alpha$ emission | 87 |
| C.7 NGC 253 poloidal magnetic field with soft X-ray emission | 87 |

List of Tables

| | | |
|-----|---|----|
| 1.1 | Constituents of the interstellar medium. | 3 |
| 4.1 | ATCA observation details. | 38 |
| A.1 | Beam properties of the 100-m Effelsberg telescope | 48 |
| A.2 | Parameters for the single-dish cleaning | 55 |

Acknowledgments

I would like to express my gratitude to Prof. Dr. Ralf-Jürgen Dettmar. He not only gave me the opportunity to perform a PhD but also stimulated my work and encouraged me all the time. I am also very grateful for the supervision by Dr. Rainer Beck and Dr. Marita Krause during my frequent visits at the MPIfR. The technical help I obtained from both was crucial to solve the various difficulties of the calibration of the radio continuum observations. The analysis and presentation of my results benefited greatly from many lengthy discussions with them.

I thank Prof. Dr. Reinhard Schlickeiser for his helpful suggestions which significantly improved the discussion of the results. I thank Uli Klein, Lutz Habertzettl, Karl-Heinz Mack, and Helge Rottmann for their assistance to the cleaning of the Effelsberg maps. Wolfgang and Patrizia Reich helped me on many occasions using NOD2 for the reduction of the Effelsberg maps. I thank Marian Soida for his crash-course in AIPS. The reduction of the VLA data was greatly assisted by Eric Greisen, Chris Carilli, and Rick Perley. Marek Jamrozý showed me how to combine the Effelsberg and the VLA maps. I thank Michael Dahlem and Jürgen Ott for supporting observations with the ATCA and the Mopra telescope. Gyula Józsa (“Josh”), Michael Dahlem, and Jamie McCallum helped me very much with the use of MIRIAD and the calibration of data from the ATCA. I had various discussions of radio continuum observations with Marian Soida, Marek Urbanik, Katarzyna Otmianowski-Mazur, Krzysztof Chyży, and Marek Weżgowiec from the observatory in Cracow. Dieter Breitschwerdt helped me a lot to understand the theory of cosmic ray transport. With Jürgen Dreher I discussed properties of magnetic reconnection. Martin Haas showed me how to calculate the radiation density from infrared observations. I received valuable comments on the manuscript I received from Enno Middelberg, Clemens Trachternach, and Giuseppe Aronica. Giuseppe Aronica provided also much technical help to write the thesis in L^AT_EX 2_ε.

This work also benefited from many discussion with people from the AIRUB, namely Zita Banhidi, Dominik Bomans, Frederic Boone, Birgitta Burggraf, Janine van Eymeren, Marcus Jütte, Volker Knierim, Elvira Krusch, Eva Manthey, Michelle Mizuno-Wiedner, Kai Polsterer, Dominik Rosenbaum, Wolfhard Schlosser, Olaf Schmithüsen, Clemens Trachternach, Ralph Tüllmann, Marcos Voelzke, and Kerstin Weis. This work would not have been possible without the computational environment maintained by Tim Falkenbach and Ingo Tertel. Thomas Luks and Volker Knierim helped me to use SOLARIS computers for the use of NOD2. Finally, I would like to thank the organizers of the GRK 787 and the SFB 591 for providing such excellent working conditions that I have found during my stay at the Ruhr-Universität Bochum.

Curriculum Vitae

| | |
|-------------|--|
| 1977 | Born on October 10 in Moers |
| 1984 – 1988 | Elementary school "St. Konrad" in Moers |
| 1988 – 1997 | High school "Gymnasium Adolfinum" in Moers: Abitur (A-levels) |
| 1997 – 2003 | Study of general physics at the "Technische Universität München" |
| 2002 – 2003 | Diploma thesis at the "Max-Planck Institut für Astrophysik" |
| June 2003 | Diploma in Physics |
| 2004 – 2007 | PhD at the "Astronomisches Institut der Ruhr-Universität Bochum" |

Bochum, December 10, 2007

Volker Heesen

Hiemit versichere ich, dass ich die vorliegende Dissertation eigenständig und ohne andere als die angegebenen Hilfsmittel angefertigt habe.

Bochum, den 10. Dezember 2007

Volker Heesen